



**A Broad-Band Spectral and Timing Study
of the X-ray Binary System Centaurus X-3**

**A Dissertation Submitted to the Faculty of the
Graduate School of the University of Maryland
at College Park**

Michael Damian Audley



Laboratory for High Energy Astrophysics

Grant NAG5-1176

National Aeronautics and
Space Administration

Goddard Space Flight Center
Greenbelt, Maryland 20771

August 1998

Available from:

NASA Center for AeroSpace Information
7121 Standard Drive
Hanover, MD 21076-1320
Price Code: A17

National Technical Information Service
5285 Port Royal Road
Springfield, VA 22161
Price Code: A10

A BROAD-BAND SPECTRAL AND
TIMING STUDY OF THE X-RAY
BINARY SYSTEM CENTAURUS X-3

by

Michael Damian Audley

Dissertation submitted to the Faculty of the Graduate School of the
University of Maryland at College Park in partial fulfillment
of the requirements for the degree of
Doctor of Philosophy
1997

Advisory Committee:

Professor Jordan A. Goodman, Chairman
Professor Elihu A. Boldt, Academic Advisor
Professor Richard F. Ellis
Professor Douglas C. Hamilton
Dr. Richard L. Kelley, Technical Advisor
Professor Marvin Leventhal

ABSTRACT

Title of Dissertation: A BROAD-BAND SPECTRAL AND
 TIMING STUDY OF THE X-RAY
 BINARY SYSTEM CENTAURUS X-3

Michael Damian Audley , Doctor of Philosophy, 1997

Dissertation directed by: Dr. Richard L. Kelley
 Laboratory for High Energy Astrophysics,
 NASA / Goddard Space Flight Center.

This dissertation describes a multi-mission investigation of the high mass X-ray binary pulsar Centaurus X-3. Cen X-3 was observed with the Broad Band X-Ray Telescope (BBXRT) in December 1990. This was the first high-resolution solid state X-ray spectrometer to cover the iron K fluorescence region. The Fe K emission feature was resolved into two components for the first time. A broad 6.7 keV feature was found to be a blend of lines from Fe XXI-Fe XXVI with energies ranging from 6.6 to 6.9 keV due to photoionization of the companion's stellar wind. A narrow line at 6.4 keV due to fluorescence of iron in relatively low ionization states was also found. The quasi-periodic oscillations (QPO) at about 40 mHz were used to estimate the surface magnetic field of Cen X-3

as $\sim 2.6 \times 10^{12}$ G and to predict that there should be a cyclotron scattering resonance absorption feature (CSRF) near 30 keV. In order to further resolve the iron line complex and to investigate the pulse-phase dependence of the iron line intensities, Cen X-3 was observed with the Advanced Satellite for Cosmology and Astrophysics (ASCA). Using ASCA's state-of-the-art non-dispersive X-ray spectrometers the 6.4 keV fluorescent iron line was found to be pulsing while the intensities of the 6.7 and 6.9 keV recombination lines do not vary with pulse phase. This confirms that the 6.4 keV line is due to reflection by relatively neutral matter close to the neutron star while the recombination lines originate in the extended stellar wind. The continuum spectrum was found to be modified by reflection from matter close to the neutron star. Observations with the EXOSAT GSPC were used to search for a CSRF. The EXOSAT spectra were consistent with the presence of a CSRF but an unambiguous detection was not possible because of a lack of sensitivity at energies higher than the cyclotron energy. Cen X-3 was then observed with the Rossi X-Ray Timing Explorer (RXTE) and evidence for a CSRF at 25.1 ± 0.3 keV was found. This corresponds to a magnetic field of $(2.16 \pm 0.03) \times 10^{12}$ G and is consistent with the value obtained from the QPO analysis.

© Copyright by
Michael Damian Audley
1997

Preface

This dissertation consists of two parts. The first part comprises Chapters 1–4. This part is intended to provide background information for the reader and to explain the motivation for the study of Cen X-3. Chapter 1 provides an overview of the spectral and timing properties of high-mass X-ray binaries. In Chapter 2 I describe the operation of the types of non-dispersive X-ray spectrometers used in this work. The X-ray observatories that were used to perform the observations are described in Chapter 3, and in Chapter 4 I give an overview of the observational properties of Cen X-3.

In the second part of the dissertation I present the original work which I carried out for this project. This began as a purely instrumental project with the aim of developing high-resolution superconducting X-ray detectors. I have placed my work on kinetic inductance microcalorimeters in Appendix A. Although the project evolved into a mainly observational one, its unifying theme is the application of state of the art non-dispersive X-ray spectrometers to the study of Cen X-3.

Since I was working on the development of X-ray detectors which would probably not be used in a mission for several years it seemed appropriate to analyse some data from an existing state of the art X-ray telescope. Dr Richard Kelley provided the data from the BBXRT observation of Cen X-3. The analysis

of these data is described in Chapter 5. The X-ray spectroscopy results led us to propose for an observation of Cen X-3 with ASCA in order to further resolve the structure of the iron K_{α} emission line and, in particular, to test my prediction that the 6.4 keV line would be the one that pulsates. The proposal was accepted for ASCA's AO-3 observational cycle and carried out in February 1995. The results are in Chapter 7. The principal investigators were R. L. Kelley and F. Nagase. I was a co-investigator. The other main result of the BBXRT analysis was my prediction that there should be a cyclotron line in the spectrum of Cen X-3 near 30 keV. In order to search for this, we proposed to observe Cen X-3 with RXTE. I was the principal investigator. The co-investigators were R. L. Kelley and K. Ebisawa. This observation was carried out in September 1996 and the results are described in Chapter 8. Meanwhile, Dr. Saequa Vrtilek provided me with some EXOSAT GSPC observations of Cen X-3 in which I searched for a cyclotron line. This analysis is presented in Chapter 6. Finally, I summarize my results, discuss their relevance, and suggest some future work in Chapter 9.

The research for this dissertation was carried out in the X-Ray Astrophysics branch of the Laboratory for High Energy Astrophysics at NASA's Goddard Space Flight Center and was supervised by Dr. Richard L. Kelley. Much of Chapter 5 has been published in the *Astrophysical Journal* (Audley et al. 1996). Part of Appendix A has appeared in the *Journal of Low Temperature Physics* (Audley et al. 1993). The contents of Chapters 6, 7, and 8 will be submitted for publication in the *Astrophysical Journal* in the near future.

Dedication

To Anne-Marie.

Acknowledgements

I would like to thank Rich Kelley for all of the help and encouragement he has given me over the last few years. I am grateful to my academic advisor Elihu Boldt for his guidance. Without Gayle Rawley, who introduced me to cryogenic electronics and the help of John Gygax, Regis Brekosky, Scott Murphy, and Caroline Stahle the instrumental part of this project would not have been possible. I thank David Osterman for providing kinetic inductors for testing and for some fruitful discussions. I would like to thank Saequa Vrtilek for making her EXOSAT GSPC data available to me and for her many useful comments and suggestions. I would also like to thank Ken Ebisawa, Lorella Angelini, and Charles Day for answering my questions. I appreciate the suggestions of the dissertation committee. They helped make this dissertation better. I would also like to thank Randall Smith for reading the manuscript and Keith Gendreau for providing some of the figures.

This work was supported by NASA grant NAG5-1176. This research made use of data obtained through the High Energy Astrophysics Science Archive Research Center Online Service, provided by the NASA-Goddard Space Flight Center.

Table of Contents

List of Tables	xiii
List of Figures	xiv
1 Introduction	1
1.1 X-Ray Astronomy	1
1.2 X-Ray Binaries	4
1.2.1 Accretion	4
1.2.2 Orbital Properties	6
1.2.3 Mass Transfer	6
1.2.4 Classification of X-Ray Binaries	11
1.2.5 Low-Mass X-Ray Binaries	11
1.2.6 High-Mass X-Ray Binaries	13
1.3 The Evolution of High-Mass X-Ray Binaries	16
1.4 Radiation Processes in High-Mass X-Ray Binaries	19
1.4.1 Continuum Emission	19
1.4.2 Cyclotron Scattering Resonance Features	23
1.4.3 The Pulse Profile	26
1.4.4 Line Emission	29

1.4.5	Iron Line Diagnostics	30
1.5	Timing Properties of High-Mass X-Ray Binaries	34
1.5.1	Dynamical Timescales for High-Mass X-Ray Binaries	34
1.5.2	The X-Ray Light Curve	35
1.5.3	Pulse Arrival Time Analysis	35
1.5.4	Interaction of the accretion disk with the magnetosphere	40
1.5.5	Quasi-Periodic Oscillations	45
2	Non-Dispersive X-Ray Spectrometers	47
2.1	Proportional Counters	49
2.1.1	Gas Scintillation Proportional Counters	50
2.2	Solid-State Ionization Detectors	51
2.2.1	Scintillation Detectors	51
2.2.2	Si(Li) Detectors	51
2.2.3	Charge-Coupled Devices	52
2.3	Thermal X-Ray Detectors	53
2.3.1	Calorimeters with Resistive Thermometers	56
2.3.2	Thermal X-Ray Detectors with Reactive Thermometers	62
2.3.3	Kinetic Inductance Thermometry	62
3	X-Ray Observatories	65
3.1	The Broad Band X-Ray Telescope	65
3.2	The European X-Ray Observatory Satellite	68
3.2.1	The Gas Scintillation Proportional Counter	68
3.3	The Advanced Satellite for Cosmology and Astrophysics	68
3.3.1	The X-Ray Telescope	68

3.3.2	The Solid State Imaging Spectrometers	70
3.3.3	The Gas Imaging Spectrometers	71
3.4	The Rossi X-Ray Timing Explorer	72
3.4.1	The Proportional Counter Array	73
3.4.2	The High Energy X-Ray Timing Experiment	73
3.5	Summary	73
4	Centaurus X-3	77
4.1	Orbital Properties	77
4.2	Mass Transfer	78
4.3	Formation of an Accretion Disk.	79
4.4	The X-Ray Light Curve	80
4.5	The X-Ray Spectrum	83
5	Resolving the Iron Line — BBXRT	88
5.1	The Observation	88
5.1.1	Background rejection	88
5.2	Results	89
5.2.1	Timing analysis	89
5.2.2	Spectroscopy of the pulse-phase averaged data	93
5.2.3	Pulse phase resolved spectroscopy	102
5.3	Discussion	104
5.3.1	The pulse profile	104
5.3.2	The Fourier power spectrum	104
5.3.3	Comparison of results with previous observations of the iron line	108

5.3.4	The origin of the broad emission feature at 6.7 keV	110
5.4	Conclusions	112
6	The Continuum Spectrum — EXOSAT GSPC	116
6.1	Motivation	116
6.2	The Observations	117
6.3	Data Analysis and Results	119
6.3.1	Background Subtraction	119
6.3.2	Spectroscopy of the pulse-phase averaged data	119
6.3.3	Pulse phase resolved spectroscopy	130
6.4	Discussion and Conclusions	130
6.4.1	The pulse profile	130
6.4.2	The continuum spectrum	134
6.4.3	The Iron Line	135
7	Effects of Reflection — ASCA	136
7.1	Motivation	136
7.2	The Observation	136
7.3	Results	137
7.3.1	Timing analysis	137
7.3.2	The Light Curve	138
7.3.3	The pulse profile	143
7.3.4	Spectroscopy	143
7.4	Discussion	153
7.4.1	The pulse profile	153
7.4.2	The X-Ray Spectrum	156

7.4.3	Pulsar Geometry	160
7.5	Conclusions	161
8	Cyclotron Line — RXTE	162
8.1	Motivation	162
8.2	The Observation	165
8.2.1	Background subtraction	165
8.3	Results	167
8.3.1	The Pulse Profile	167
8.3.2	Spectroscopy	168
8.4	Discussion and Conclusions	171
9	Conclusions	175
9.1	List of Results	175
9.2	Future Work	176
9.2.1	The Advanced X-Ray Astrophysics Facility	177
9.2.2	X-Ray Multi-Mirror Mission	178
9.2.3	Astro-E	178
9.2.4	The Constellation Mission	179
9.2.5	Summary	179
APPENDIX: Investigation of Kinetic Inductance Thermometry for		
	X-Ray Astrophysics	181
A.1	Aluminum Proof-of-Concept Kinetic Inductors	181
A.1.1	Device Fabrication	181
A.1.2	Testing	181
A.2	Limitations of Kinetic Inductors	185

A.2.1 Critical currents	185
A.3 Conclusions	191
Glossary	192
References	197

List of Tables

1.1	Accretion-powered pulsars in high-mass supergiant and giant systems.	17
3.1	X-ray observatories and results used in this dissertation.	76
5.1	Spectral parameters of fits to phase average data.	98
5.1	— Continued	99
5.1	— Continued	100
6.1	The GSPC Data.	118
6.2	Pulse-phase average data fitted to a cut-off power law.	121
6.3	Pulse-phase average data fitted to a black body and thermal bremsstrahlung.	122
6.4	Pulse-phase average data fitted to a Comptonization model.	123
6.5	Pulse-phase average data fitted to a power law and CSRF.	124
7.1	Orbital parameters from pulse arrival time analysis.	138
7.2	Observation-average best fit parameters from SIS1 data.	146
7.3	Observation-average best fit parameters from GIS data.	151
8.1	Cyclotron features detected in X-ray pulsar spectra.	173

List of Figures

1.1	X-Ray spectra of the quiet sun and cosmic sources.	3
1.2	The HEAO-1 sky survey.	4
1.3	Roche lobes of a high-mass X-ray binary.	7
1.4	Accretion from a stellar wind.	8
1.5	Accretion by Roche lobe overflow.	9
1.6	Formation of a HMXB.	18
1.7	Calculated spectrum for an AXP with CSRF.	25
1.8	Formation of a fan beam emission pattern.	27
1.9	Formation of a pencil beam emission pattern.	28
1.10	Dependence of observed equivalent width on source geometry. . .	32
1.11	Dependence of Fe K_{α} line energy on ionization stage.	33
1.12	Eclipse half-angle.	36
1.13	Geometry of a high-mass X-ray binary system.	37
1.14	An accreting X-ray pulsar.	42
1.15	Relationship between spin-up rate and luminosity for accreting pulsars.	46
2.1	A coronal spectrum at different energy resolutions.	48
2.2	Cross-section of a MOS capacitor.	53

2.3	Charge transfer in a CCD.	54
2.4	A microcalorimeter	55
2.5	Pre-flight spectrum from an XQC pixel.	60
2.6	Cross-section of a kinetic inductor.	64
3.1	BBXRT.	66
3.2	Nested X-ray mirrors.	66
3.3	Layout of the BBXRT detectors.	67
3.4	The EXOSAT GSPC.	69
3.5	The ASCA GIS	72
3.6	Effective area curves of the X-ray telescopes used in this work. . .	75
4.1	Average V band light curve of Cen X-3	81
4.2	ASM light curve of Cen X-3	82
4.3	Typical pulse-phase averaged spectrum between 1 and 20 keV . .	85
4.4	Radial dependence of accretion disk parameters	87
5.1	The long-term behavior of the pulse period of Cen X-3.	90
5.2	BBXRT average pulse profile.	91
5.3	BBXRT energy resolved pulse profiles.	92
5.4	BBXRT Fourier power spectrum.	93
5.5	BBXRT pulse-phase averaged spectrum – one line model.	94
5.6	BBXRT pulse-phase averaged spectrum – two line model.	97
5.7	Variation of spectral parameters with pulse phase.	103
5.8	BBXRT pulse-phase averaged spectrum – five line model.	113
6.1	Fits to pulse-phase average data from dataset 1.	125

6.2	Pulse-phase average data from dataset 3.	126
6.3	Pulse-phase average data from dataset 4.	127
6.4	Simultaneous fits to GSPC and ME Ar H1 data from dataset 1. . .	129
6.5	Variation of spectral parameters with pulse phase for dataset 1. .	131
6.6	Variation of spectral parameters with pulse phase for dataset 3. .	132
6.7	Variation of spectral parameters with pulse phase for dataset 4. .	133
7.1	ASCA light curve and hardness ratio.	139
7.2	ASCA hardness <i>vs.</i> intensity	140
7.3	Possible QPO in pre-eclipse data.	141
7.4	Possible QPO in post-flare data.	142
7.5	Orbital phase resolved GIS pulse profiles and hardness ratios. . .	144
7.6	SIS spectrum of iron line region.	145
7.7	Observation-average GIS spectrum.	147
7.8	Origin of a reflected component.	148
7.9	Observation-average GIS spectrum with broad reflection feature. .	149
7.10	Variation of spectral parameters with pulse phase.	150
7.11	Orbital dependence of fluorescent iron line equivalent width. . . .	152
7.12	Orbital-phase resolved spectra	154
7.13	Orbital dependence of spectral parameters.	155
7.14	Dependence of hard and medium component intensities on pulse phase.	157
7.15	Variation of iron line intensities with pulse phase	159
8.1	RXTE Light curve	166
8.2	RXTE pulse profiles.	168

8.3	PCA spectrum with Comptonization model.	169
8.4	PCA spectrum with Comptonization model and CSRF.	170
8.5	Simultaneous fit to PCA and HEXTE data.	171
8.6	Variation of observed CSRF energy with height above the neutron star surface.	174
9.1	Comparison of effective areas of future X-ray missions.	180
A1	Kinetic inductor layout	182
A2	Tunnel diode I - V curve.	184
A3	Tunnel diode oscillator readout.	186
A4	Variation of TDO frequency with temperature.	187
A5	Superconducting transitions of molybdenum meander strip.	187
A6	Superconducting transitions of titanium meander strip.	188
A7	More superconducting transitions of titanium meander strip.	189
A8	Critical currents of gold-passivated titanium meander strips.	190

Chapter 1

Introduction

1.1 X-Ray Astronomy

Because the earth's atmosphere is opaque to X-rays, X-ray astronomy is a relatively young field. The first celestial X-ray source to be identified by early sounding rocket flights was the sun. These early observations did not seem promising for X-ray astronomy as the sun is not a very strong X-ray emitter so any detectable extrasolar source would have to be much more luminous. Luckily, this turned out to be the case. It was during a rocket flight (Giacconi et al. 1962) looking for fluorescence from the moon's surface caused by the solar wind that the first extrasolar X-ray source was detected. This was eventually identified as the X-ray binary system Sco X-1. This discovery and the first decade of X-ray astronomy are described by Giacconi (1974). As shown in Figure 1.1 the integrated flux from the X-ray background is greater than that from the quiet sun above 3 keV and Sco X-1 is brighter than the quiet sun above 4 keV (Boldt 1974).

Launched in December 1970, Uhuru was the first dedicated X-ray astronomy satellite (Kellogg 1975). It used two beryllium-window proportional counters

with mechanical collimators to map the X-ray sky between 2 and 6 keV as the satellite rotated. Uhuru had a time resolution of 0.1 s and was used to discover the Doppler shifts in the pulse period of Cen X-3 that revealed it as a binary system (Schreier et al. 1972). The Einstein observatory was launched November 1978. It was the first X-ray satellite to provide high-resolution imaging with a grazing-incidence mirror. The European X-Ray Observatory Satellite (EXOSAT) had a 90 hour orbital period which allowed continuous observations of X-ray sources lasting several days without the interference of earth occultations. EXOSAT led to the discovery of quasi-periodic oscillations in the light curves of X-ray binaries. EXOSAT's ability to perform long, uninterrupted observations enabled the nature of X-ray bursts to be determined. The third Japanese X-ray satellite Ginga had a large effective area above 10 keV which led to the discovery of cyclotron lines in the spectra of seven X-ray binaries, compared to the two cyclotron line sources that were known previously. ROSAT provided high-resolution imaging and a deep all-sky survey in soft X-rays below 2 keV. An overview of the history of X-ray astronomy is given by Charles and Seward (1995).

X-ray astronomy has changed our view of the universe and revealed it to be full of explosive, high energy phenomena. Rotation-powered pulsars can emit X-rays through synchrotron radiation. Supernova remnants emit X-rays from shocks as ejecta collide with and sweep up the interstellar medium. The hot coronae of stars emit soft X-rays. However, the accretion of matter onto compact objects is the driving force behind X-ray binaries and active galactic nuclei, which are among the most luminous sources. Thermal emission from gravitationally bound, hot intracluster gas makes galaxy clusters X-ray emitters.

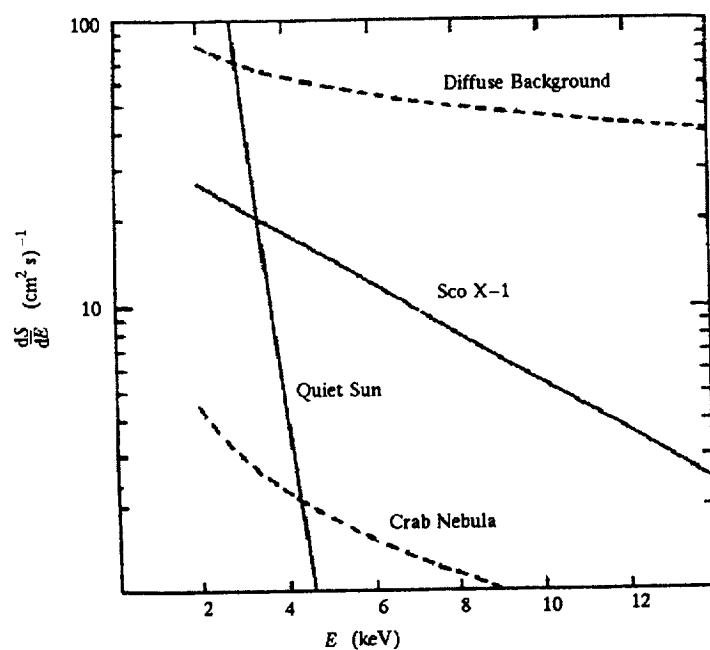


Fig. 1.1— X-ray spectrum of the quiet sun compared to the diffuse X-ray background and two Galactic sources (from Boldt 1974). The intensity of Cen X-3 in its high state is ~ 0.25 times that of the Crab.

Normal galaxies emit X-rays due to a hot interstellar medium, X-ray binaries, and supernova remnants. Figure 1.2 shows the X-ray sky as seen with the HEAO-1 A1 instrument in 1977–79 (Wood et al. 1984) and includes examples of these different emission mechanisms.

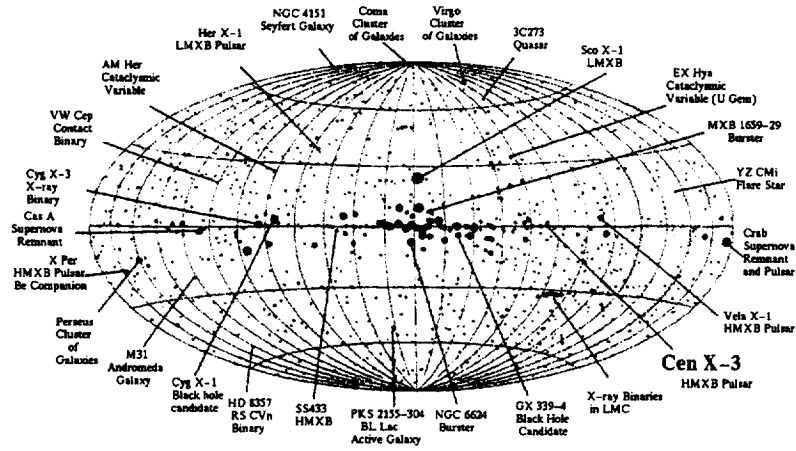


Fig. 1.2— The HEAO-1 sky survey in Galactic coordinates showing 842 X-ray sources (Wood et al. 1984). The sizes of the dots are proportional to the log of the intensity. The survey covered the 0.25–25 keV band between 1977 and 1979.

1.2 X-Ray Binaries

1.2.1 Accretion

The brightest sources in the X-ray sky are Galactic X-ray binaries. The brightest is usually Sco X-1 although its intensity is often surpassed by transient sources. In an X-ray binary, a compact star accretes matter from its companion. The gravitational potential energy of this matter is converted to kinetic energy and eventually to radiation, giving rise to the high observed luminosities. The compact star may be a white dwarf, neutron star, or black hole. In optical astronomy it is usual to refer to the heavier star in a binary system as the primary as it is usually the brighter star. In a high-mass X-ray binary the lighter, compact component is the X-ray emitter. Thus, in this dissertation I will refer to the

compact, accreting component of the X-ray binary as the primary. I will refer to the donor star as the companion.

The energy that can be extracted from accretion increases as the radius of the compact object decreases. This is because the amount of gravitational potential energy that infalling matter loses increases as the radius of the accreting object decreases. For a star of radius R_x and mass M_x which accretes matter at a rate \dot{M} , the accretion luminosity is (see Frank et al. 1985, and references therein)

$$L_{\text{acc}} = \frac{GM_x \dot{M}}{R_x} \quad (1-1)$$

assuming that all the kinetic energy of the accreted matter is converted to radiation at R_x . Neutron stars convert accreted mass to energy with an efficiency $\varepsilon = \frac{L_x}{\dot{M}c^2}$ of ~ 0.1 compared with 0.007 for thermonuclear fusion. An accreting neutron star emits radiation mostly in the energy range 1 keV–50 MeV (Frank et al. 1985). A crude estimate of the upper limit to the luminosity of these sources may be obtained by equating the outward force on electron-proton pairs with the gravitational force. The resulting luminosity

$$L_{\text{Edd}} = \frac{4\pi GMm_p c}{\sigma_T} \quad (1-2)$$

$$\approx 1.3 \times 10^{38} \left(\frac{M}{M_\odot} \right) \text{ erg s}^{-1} \quad (1-3)$$

is known as the Eddington limit. If the luminosity exceeds this value the radiation pressure from the source overcomes the gravitational force and accretion stops. This is only a rough guide as it assumes steady-state, spherical accretion.

1.2.2 Orbital Properties

The effective gravitational potential in a corotating frame is the Roche potential.

This has the form

$$\Phi_R(\mathbf{r}) = -\frac{GM_c}{|\mathbf{r} - \mathbf{r}_c|} - \frac{GM_x}{|\mathbf{r} - \mathbf{r}_x|} - \frac{1}{2}(\boldsymbol{\omega} \times \mathbf{r})^2 \quad (1-4)$$

where \mathbf{r}_c , \mathbf{r}_x , M_c , and M_x are the position vectors and masses of the companion and accreting stars, respectively (Frank et al. 1985). The orbital angular velocity of the binary is ω . This form for the potential assumes that the companion is rotating synchronously. If the companion's rotation is not synchronized with ω the effective potential will be the generalized Roche potential (Avni and Bahcall 1975, and references therein):

$$\Phi = -GM_c \left[\frac{1}{|\mathbf{r} - \mathbf{r}_c|} + \frac{q}{|\mathbf{r} - \mathbf{r}_x|} - \frac{x}{D} + \frac{1+q}{2}\Omega^2(x^2 + y^2) \right] \quad (1-5)$$

where $q = M_x/M_c$, D is the separation of the stars, and $\Omega = \omega_c/\omega$ is the ratio of the angular speed of the companion's rotation to the orbital angular speed. The x and y -axes are in the orbital plane as shown in Figure 1.3. In either case the qualitative features of the potential are the same. There is a critical surface consisting of two Roche lobes, one surrounding each star and connected by a saddle point (the first Lagrange or L_1 point). Matter may pass most easily from the companion to the primary through the L_1 point. Figure 1.3 shows the critical Roche surface of an X-ray binary similar to Cen X-3.

1.2.3 Mass Transfer

The mass transfer can take place by capture of the companion's stellar wind (see Figure 1.4) or by Roche lobe overflow as shown in Figure 1.5. These two

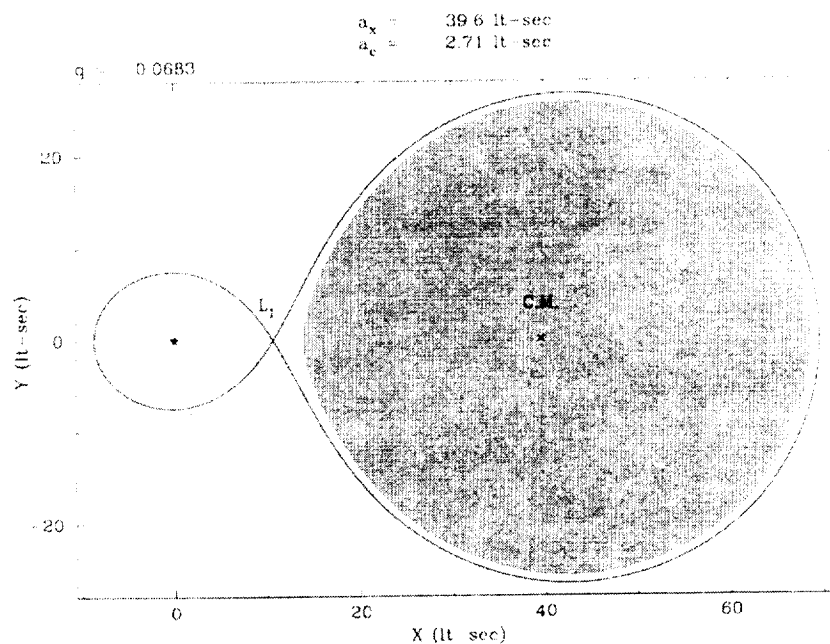


Fig. 1.3— Roche Lobe geometry of an X-ray binary. The orbital separation $D = a_x + a_c$ and the mass ratio $q \equiv M_x/M_c$ have been chosen to be similar to those of Cen X-3. The high-mass companion is close to filling its Roche lobe and is tidally distorted. The X- and Y-axes lie in the orbital plane and the accreting neutron star is at the origin.

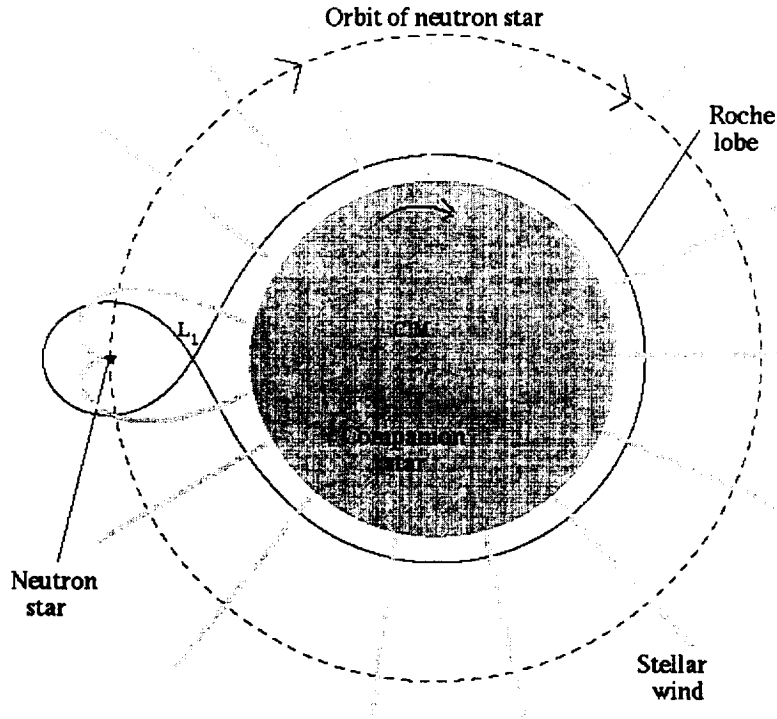


Fig. 1.4— Mass-transfer in an X-ray binary by wind accretion.

mechanisms represent the extreme cases. However the difference between these two cases is not distinct for companions that come close to filling their Roche Lobes. Because of the presence of the accreting object, the stellar wind will be enhanced along the line of centers, forming a tidal stream that flows through the first Lagrange (L_1) point (Petterson 1978; Blondin et al. 1991). Such a system may still be said to be wind-fed but most of the accreted matter flows through the L_1 point.

Whether or not an accretion disk forms depends on the mass transfer mecha-

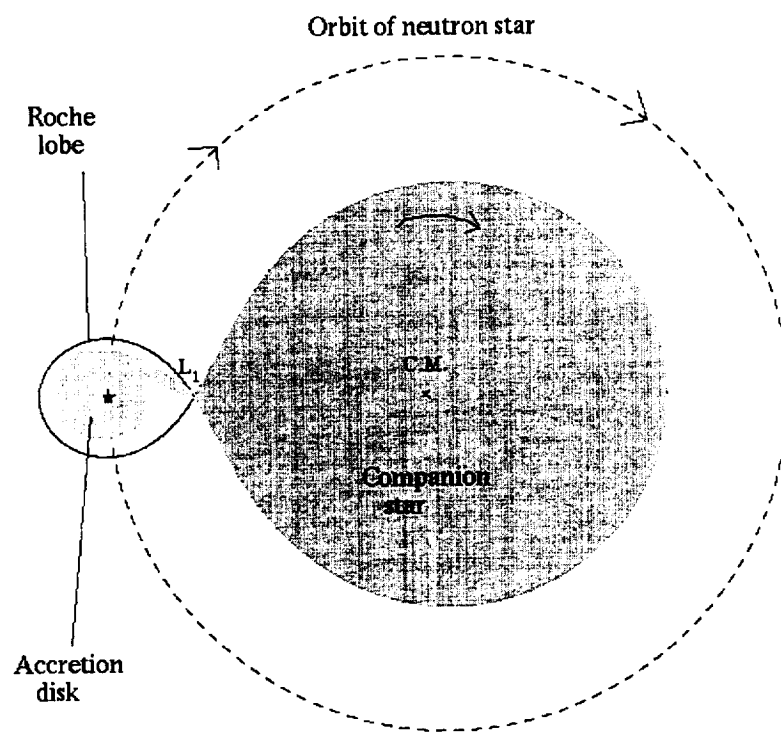


Fig. 1.5— Mass-transfer in an X-ray binary by Roche lobe overflow.

nism. For Roche lobe overflow an accretion disk is required to lower the specific angular momentum of the transferred matter before it can accrete onto the compact object. In the case of wind accretion an accretion disk may not be required depending on the orbital angular speed of the accreting star.

Following Frank et al. (1985) we can verify that an accretion disk should form in the case of Roche lobe overflow. The specific angular momentum of the material spilling through the L_1 point is essentially $b^2\omega$, where b is the distance from the accreting object to the L_1 point and ω is the orbital angular speed. In order to accrete onto the compact object this matter must shed angular momentum. The stream can lose energy through shocks but it is difficult for it to lose angular momentum. Thus the accreting matter will initially settle into the lowest energy orbit consistent with its specific angular momentum. Assuming the matter stream has lost no angular momentum since passing through the L_1 point this will be a circular orbit with radius $R_{\text{circ}} = b^2\omega/v_\phi$ where

$$v_\phi = \sqrt{\frac{GM_x M_\odot}{R_{\text{circ}}}} \quad (1-6)$$

is the tangential velocity. Viscous interactions will cause the plasma to spread out and form an accretion disk. The circularization radius R_{circ} may be expressed in terms of the orbital separation a and the ratio of the masses of the accreting star and the companion $q \equiv M_x/M_c$ as

$$\begin{aligned} R_{\text{circ}} &= a(1+q) \left(\frac{b}{a}\right)^4 \\ &\approx a(1+q)(0.500 - 0.227 \log_{10} q)^4 \\ &\approx 4(1+q)^{4/3}(0.500 - 0.227 \log_{10} q)^4 P_{\text{day}}^{2/3} R_\odot \end{aligned} \quad (1-7)$$

where P_{day} is the orbital period in days. Here the approximate formula

$$b = a [0.500 - 0.227 \log_{10} q] \quad (1-8)$$

has been used (Frank et al. 1985). If the accreting star is a white dwarf, a neutron star, or a black hole, R_{circ} will be larger than the stellar radius, allowing an accretion disk to form. R_{circ} will also be smaller than the primary's Roche lobe radius which is

$$R_L = \frac{0.49}{0.6 + q^{2/3} \ln(1 + q^{-1/3})} \quad (1-9)$$

using the approximation of Eggleton (1983).

1.2.4 Classification of X-Ray Binaries

X-Ray binaries are conventionally divided into two classes: the low-mass X-ray binaries (LMXB) and the high-mass X-ray binaries (HMXB) (Bradt and McClintock 1983). Bradt and McClintock based their classification scheme on the ratio of X-ray to optical luminosity. For a HMXB

$$\frac{L_x(2 - 10 \text{ keV})}{L_{\text{opt}}(3000 - 7000 \text{ \AA})} \lesssim 10 \quad (1-10)$$

while for a LMXB this ratio is greater than about 10. This division based on optical and X-ray luminosities coincides with a division based on the mass of the companion. This is because if the companion is an early type massive star it will dominate the optical luminosity. If the companion is a low mass star the optical luminosity will be dominated by the accretion disk.

1.2.5 Low-Mass X-Ray Binaries

The LMXB consist of a compact object accreting matter from a companion whose mass is less than $\sim 2M_{\odot}$ (e.g. Hayakawa 1985). These companions are cooler than the early-type companions of HMXB (Lang 1991) and do not have strong winds so the orbit must be compact enough for Roche lobe overflow to

take place. The optical emission of an LMXB is dominated by thermal emission from the accretion disk. Evaporating disk material may form an accretion disk corona (ADC; Kallman 1993). Other characteristics of the source will depend on the magnetic dipole moment of the compact component.

LMXB in which the accreting star is a white dwarf are known as cataclysmic variables. The available gravitational binding energy for radiation production is a factor of 10^3 less due to their larger radii (10^9 cm compared with 10^6 cm for neutron stars) and they are relatively dim in X-rays unless thermonuclear detonation of accreted material occurs, creating a nova. The type I bursts which occur in some neutron star LMXB are also due to runaway thermonuclear burning. This phenomenon is suppressed in pulsars due to the higher surface magnetic fields (e.g. Lewin et al. 1995). This may happen because the magnetic field reduces the radiative and conductive opacities and inhibits convective mixing of the helium-burning layer (Joss and Li 1980). Another effect may be the funneling of accreting matter onto the polar caps which increases the rate of mass accretion per unit area (Joss 1978). Type II bursts are another phenomenon that occur in accreting neutron star systems (e.g. Lewin et al. 1995). They are believed to be due to impulsive accretion of matter caused by instabilities in the inner accretion disk. In AM Her systems a magnetic white dwarf co-rotates with its companion and no accretion disk forms. This can occur with surface magnetic fields as low as 10^9 G because the magnetic dipole moment increases with stellar radius.

1.2.6 High-Mass X-Ray Binaries

In HMXB the donor star is more massive than $\sim 2M_{\odot}$ (Hayakawa 1985). The orbital separation is generally wider than in a typical LMXB because the companion is larger. The companion is generally highly evolved and dominates the optical emission. Tidal distortion of the companion can cause ellipsoidal variations in the optical light curve. These occur partly because the observer will see different parts of the distorted companion at different angles as it rotates. The optical light curve may also be affected by X-ray heating and light from an accretion disk. By modeling the ellipsoidal variations it is possible to determine how close the companion comes to filling its Roche Lobe (e.g. van Paradijs and McClintock 1995, and references therein). The companion which is of spectral type O or B has a strong stellar wind. If the wind is not highly ionized it may be driven by the absorption of UV photons from the companion. This is called a line-driven wind. If the wind material is highly ionized it will be transparent to UV radiation and another driving mechanism such as X-ray heating may be involved. Accretion can also take place by Roche lobe overflow which is favored by the low density of the donor. The dominant ionization mechanism is photoionization due to the X-ray luminosity which may be as high as $\sim 10^{38} \text{ erg s}^{-1}$. Because the HMXB have heavier companions they tend to be younger than LMXB. The HMXB are population I objects and are concentrated in the Galactic plane. LMXB, in contrast, tend to be population II objects and their spatial distribution shows no preference for the Galactic plane, although they tend to be concentrated towards the Galactic center. The HMXB also tend to have stronger magnetic fields than the LMXB. It is possible that this is due to accretion-induced decay of the neutron star's magnetic field. However the issue

of magnetic field decay is not settled (Bhattacharya and Srinivasan 1995). For example, the LMXB pulsar Her X-1 has a field of 3×10^{12} G (Voges et al. 1982) and is believed to be $> 10^8$ years old while X2259+586 which is a young pulsar in a supernova remnant seems to have a field of 5×10^{11} G (Koyama et al. 1986). Comparison of nine X-ray pulsars whose fields are known from cyclotron line observations (Makishima et al. 1992) indicates that the magnetic field does not decay on the timescale of the lifetime of massive X-ray binaries ($\sim 10^7$ years). A consequence of the lower average magnetic fields of LMXB is that the accretion disk extends closer to the accreting star where the radiation flux is high. This can photoionize and heat the inner accretion disk creating an ADC which can modify the spectrum (e.g. Kallman 1993).

The properties of the known accreting X-ray pulsars (AXP) are summarized by Bildsten et al. (1997). Table 1.1 shows the properties of the known HMXB with supergiant companions that are also pulsars (Bildsten et al. 1997). The compact component in these systems is a neutron star with a high magnetic field ($\sim 10^{12}$ G). The pulsed emission comes from the channeling of ionized accreting matter onto the polar caps of the rotating neutron star. These systems are distinct from the rotation-powered pulsars. They have much longer spin periods (on the order of $1\text{--}10^2$ s). At these periods the dipole radiation from an isolated pulsar would be undetectable. Such long periods cannot be attained by the spin-down power of a rotation-powered pulsar. The AXP must have been spun down by some other mechanism. The most likely mechanism is accretion. Davidson and Ostriker (1973) showed that a fast-spinning neutron star would not be able to accrete matter because of the centrifugal barrier in the effective potential. This is known as the propeller effect (Illarionov and Sunyaev 1975). The rotating

magnetosphere would eject any infalling matter from the system, resulting in a braking torque on the pulsar. For a pulsar with spin period P_0 the efficiency of this braking exceeds that of dipole-radiation braking by a factor $(r_c/r_m)^3$ where $r_c = P_0 c / 2\pi$ is the light-cylinder radius and r_m is the magnetosphere radius (see Section 1.5.4).

Some HMXB have detectable radio emission which is mostly due to synchrotron radiation in lobes of matter ejected from the system. However, in contrast to the rotation-powered pulsars none of the pulsar systems in Table 1.1 is a radio source. In fact, none of the LMXB that are known to be accreting pulsars has detectable radio emission (Hjellming and Han 1995). This is not surprising because if the early-type companion's wind is significantly ionized it will obscure radio emission from the source's inner regions. The refractive index of the medium for radio waves of frequency ν is

$$n = \sqrt{1 - \left(\frac{\nu_p}{\nu}\right)^2} \quad (1-11)$$

where

$$\nu_p = \sqrt{\frac{4\pi N_e e^2}{m_e}} \quad (1-12)$$

is the plasma frequency. Close to the source where N_e is high, n will be imaginary and the radio emission will be attenuated. Thus any detectable radio emission will come from regions far enough from the source so that $\nu_p < \nu$. The minimum distance for which this condition is met is between 10^{12} and 10^{15} cm (Hjellming 1978). If matter is ejected from the system it may have detectable synchrotron emission in radio. An example of this is the non-pulsating HMXB SS433 which has radio jets (e.g. Hjellming and Han 1995). X-ray binaries that have radio jets are known as microquasars. These are believed to be binary systems where the

primary is a neutron star or black hole which is accreting at super-Eddington rates, causing the formation of jets. The name microquasar comes from the similarity of these jets to those ejected by the accreting black holes at the centers of active galactic nuclei.

1.3 The Evolution of High-Mass X-Ray Binaries

The evolution of binary systems is determined by three timescales. The time for the system to come to hydrostatic equilibrium is short compared to the other two. The thermal or Kelvin-Helmholtz timescale is

$$t_{\text{th}} = 3 \times 10^7 \left(\frac{M_{\odot}}{M_c} \right)^2 \text{ years.} \quad (1-13)$$

The nuclear timescale is

$$t_{\text{nuc}} \approx 10^{10} \left(\frac{M_{\odot}}{M_c} \right)^{\frac{5}{2}} \text{ years.} \quad (1-14)$$

This is the timescale for hydrogen core burning to take place in the star at $\sim 10^7$ K, leading to the formation of a helium core. Figure 1.6 shows a possible scenario for the formation of a HMXB (van den Heuvel and Heise 1972).

Conservative mass transfer will cause the orbital separation and period to decrease, causing the companion's Roche lobe to shrink (e.g. Frank et al. 1985). In a close HMXB such as Cen X-3 tidal forces can be important. These will cause the neutron star's orbit to be circularized a few million years after the supernova that created it. Once the orbit is circularized, a tidal instability can set in if the ratio of orbital to spin angular momentum is less than 3. In this

Table 1.1. Accretion-powered pulsars in high-mass supergiant and giant systems.

Name	l_{II}	b_{II}	P_{spin} (s)	P_{orb} (d)	Companion
Cen X-3	292.1	+0.3	4.82	2.09	V779 Cen (06–8f)
SMC X-1	300.4	−43.6	0.717	3.89	Sk16O (BO I)
RX J0648.1–4419	253.7	−19.1	13.18	1.54	HD 49798 (06p)
LMC X-4	276.3	−32.5	13.5	1.408	Sk-Ph (07 III–V)
OA0 1657–415	344.4	+0.3	37.7	10.4	(B0–6Iab)
Vela X-1	263.1	+3.9	283	8.96	HD77581 (BO.5Ib)
1E 1145–614	295.5	−0.0	297	5.648	V830 Cen (B2Iae)
4U 1907+09	43.7	+0.5	438	8.38	(B I)
4U 1538–52	327.4	+2.1	530	3.73	QV Nor (BO1ab)
GX 301–2	300.1	−0.0	681	41.5	Wray 977 (B1.5Ia)

Note. — From Bildsten et al. (1997)

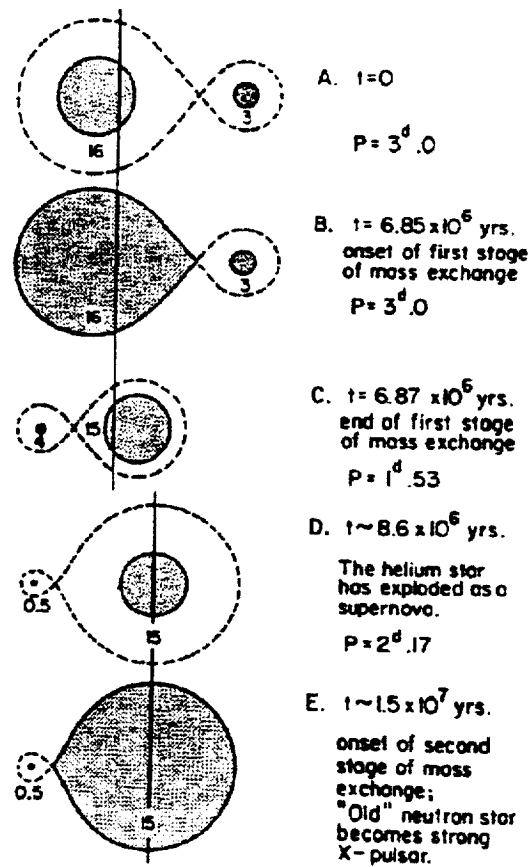


Fig. 1.6— Possible scenario for the formation of a HMXB (van den Heuvel and Heise 1972). The center of mass of the system is represented by the vertical lines.

case the orbit will decay on a timescale of $\sim 5 \times 10^5$ years and the neutron star will spiral into the companion's atmosphere. When the companion leaves the main sequence, it will overfill its Roche lobe and mass transfer will occur on the thermal timescale t_{th} . The primary will quickly spiral in, resulting in a LMXB comprising the primary neutron star and the He core of the companion. The companion may later undergo a supernova explosion, either disrupting the system or forming a binary pulsar system.

1.4 Radiation Processes in High-Mass X-Ray Binaries

1.4.1 Continuum Emission

The X-ray spectra of HMXB between 1 and 20 keV may be described by a cut-off power law (White et al. 1983). A spectrum of this form may be produced by Comptonization of soft X-rays in an optically thick medium (e.g. Hayakawa 1985).

The infalling matter will be heated up as its gravitational potential energy is converted to thermal energy. How this energy emerges as radiation depends on the geometry of the accretion column and the magnetic field dependent opacity of the infalling matter. If the matter is continuously decelerated by Coulomb interactions it will thermalize on the surface and the radiation will be a soft black body with temperature $\sim 10^7\text{K}$. However it is not clear how this can happen as the Coulomb stopping length is greater than the neutron star radius. If the infalling matter is stopped at a shock and then settles subsonically to the surface

the resulting spectrum will be similar to that of thin thermal bremsstrahlung and a black body. If the electron density is high enough this spectrum will be Comptonized. This collisionless shock might be produced by radiation pressure.

Reasonable plasma parameters for the accretion column may be roughly estimated (e.g. Mészáros 1992). We can estimate the temperature by assuming the polar cap radiates as a black body:

$$\begin{aligned} T_{\text{bb}} &\approx \left(\frac{L_x}{\sigma A} \right)^{\frac{1}{4}} \\ &= 2 \times 10^5 L_{37}^{\frac{1}{4}} A_{10}^{-\frac{1}{4}} \text{ K} \end{aligned} \quad (1-15)$$

where L_{37} is the luminosity in units of $10^{37} \text{ erg s}^{-1}$ and A_{10} is the polar cap area in units of 10^{10} cm^2 . If there is a shock above the surface the temperature will be higher (Frank et al. 1985):

$$\begin{aligned} T &\approx \frac{3}{8} \frac{GM_x m_p}{k R_x} \\ &= 6 \times 10^{11} \left(\frac{M_x}{M_\odot} \right) R_6^{-1} \text{ K} \end{aligned} \quad (1-16)$$

where m_p is the proton mass and R_6 is the neutron star radius in units of 10^6 cm . For an optically thin plasma with $T > 10^8 \text{ K}$ cooling is dominated by bremsstrahlung. Thus if the post-shock material is optically thin a thermal bremsstrahlung spectrum (Rybicki and Lightman 1979) will be emitted. For an ion of atomic number Z the emission rate is

$$\epsilon_\nu^{\text{ff}} = 6.8 \times 10^{-38} Z^2 n_e n_i T^{-\frac{1}{2}} e^{-\frac{h\nu}{kT}} \bar{g}_{\text{ff}} \text{ erg s}^{-1} \text{ cm}^{-3} \text{ Hz}^{-1} \quad (1-17)$$

so that

$$\epsilon_\nu^{\text{ff}} \approx 6.8 \times 10^{-38} n_e n_H \left(1 + 4 \frac{n_{\text{He}}}{n_H} \right) T^{-\frac{1}{2}} e^{-\frac{h\nu}{kT}} \bar{g}_{\text{ff}} \text{ erg s}^{-1} \text{ cm}^{-3} \text{ Hz}^{-1} \quad (1-18)$$

for an astrophysical plasma where $\bar{g}_{\text{ff}} \sim 1$ is the velocity-averaged Gaunt factor and n_{H} and n_{He} are the number densities of H and He. The total power emitted per unit volume will be

$$\epsilon^{\text{ff}} = 1.1 \times 10^{-21} n_e n_{\text{H}} \left(1 + 4 \frac{n_{\text{He}}}{n_{\text{H}}}\right) \left(\frac{M_{\text{x}}}{M_{\odot}}\right)^{\frac{1}{2}} R_6^{-\frac{1}{2}} \bar{g}_B \text{ erg s}^{-1} \text{ cm}^{-3} \quad (1-19)$$

where $\bar{g}_B(T) \sim 1.2$ is the frequency average of \bar{g}_{ff} . The density of the accretion column should be greater than the spherical free-fall density

$$\rho = \frac{\dot{M}}{v_{\text{ff}} 2A} \sim 10^{-3} L_{37} \text{ g cm}^{-3}. \quad (1-20)$$

The optical depth will be somewhere between the Thomson depth of free-falling material across an accretion column width of ~ 1 km and the stopping length for infalling protons on atmospheric protons:

$$0.6 L_{37} \lesssim \tau_{\text{T}} \lesssim 22. \quad (1-21)$$

Soft photons from the settling accretion mound will be Comptonized to produce a power-law for $E \lesssim kT$ and a turnover above $E \sim kT$.

Diffusive Comptonization is described by the Kompaneets equation (Kompaneets 1957)

$$\frac{\partial D}{\partial y} = \frac{1}{x^2} \frac{\partial}{\partial x} \left[x^4 \left(D + D^2 + \frac{\partial D}{\partial x} \right) \right] \quad (1-22)$$

where $D(\nu)$ is the photon phase space density which is related to the total flux $I(\nu)$ by

$$D(\nu) = \frac{c^2 I(\nu)}{8\pi h \nu^3}. \quad (1-23)$$

Here

$$x = \frac{h\nu}{kT} \quad (1-24)$$

is the photon energy in units of kT and

$$y = \sigma_T n c t \left(\frac{kT}{mc^2} \right). \quad (1-25)$$

For an infinite medium the Kompaneets equation may be solved to obtain a spectrum. At low frequencies where $D \gg 1$, $D = \frac{1}{x}$ which is the Rayleigh-Jeans spectrum. At high frequencies where $D \ll 1$, $D = \exp(-x)$ which is the Wien spectrum.

For a finite non-relativistic thermal distribution of electrons the Compton y parameter is

$$y_{NR} = \frac{4kT}{mc^2} \max(\tau_{es}, \tau_{es}^2) \quad (1-26)$$

where τ_{es} is the optical depth for electron scattering. The Compton y parameter is essentially the average fractional energy change per scattering times the mean number of scattering. It provides a measure of how much the input spectrum will be affected by Compton scattering. For $y_{NR} \gg 1$ we have saturated Comptonization, resulting in a Wien spectrum. For $y_{NR} \ll 1$ the resulting spectrum is a modified black body. The regime where $y_{NR} \gtrsim 1$ is known as unsaturated Comptonization. In this case the Kompaneets equation has to be solved.

Sunyaev and Titarchuk (1980) solved the Kompaneets equation for the up-scattering of low-energy photons by a spherical distribution of hot electrons. For an initial photon energy x_0 the emergent spectrum is $F(x, x_0) = x^3 D$. For $x \leq x_0$

$$F(x, x_0) = \frac{\alpha(\alpha + 3)}{2\alpha + 3} \left(\frac{x}{x_0} \right)^{\alpha+3} \quad (1-27)$$

and for $x \geq x_0$

$$F(x, x_0) = \frac{\alpha(\alpha + 3)x_0^\alpha}{\gamma(2\alpha + 1)} x^3 e^{-x} \int_0^\infty t^{\alpha-1} e^{-t} \left(1 + \frac{t}{x} \right)^{\alpha+3} dt \quad (1-28)$$

where

$$\alpha = \left[\frac{4}{y_{\text{NR}}} + \frac{9}{4} \right]^{\frac{1}{2}} - \frac{3}{2}. \quad (1-29)$$

For $y_{\text{NR}} \gtrsim 1$ the form of the spectrum is a power-law with an exponential cut-off for photon energies above $\sim 4kT$.

1.4.2 Cyclotron Scattering Resonance Features

An electron moving in a uniform magnetic field will be acted upon by the Lorentz force

$$\mathbf{F} = e \frac{\mathbf{v} \times \mathbf{B}}{c} \quad (1-30)$$

and will describe a helix about the field lines with radius

$$R = \frac{v_{\perp} m_e}{eB} \quad (1-31)$$

where v_{\perp} is the component of the electron's velocity normal to the magnetic field. A quantum treatment is required if the de Broglie wavelength of the electrons is comparable to R . In this case the transverse energy of the electrons is quantized into Landau levels. An electron in a Landau level is in a bound state so it does not emit synchrotron radiation. Because the lifetimes of the excited Landau levels are short compared to the time for collisional de-excitation, radiation is scattered out of the beam rather than being absorbed. The transition energy is

$$E_{\text{Cy}} = \frac{e\hbar}{m_e} B = 11.6 B_{12} \text{ keV} \quad (1-32)$$

where B_{12} is the magnetic field in units of 10^{12} G. In the accretion column of an accreting X-ray pulsar we expect that the magnetic field is strong enough that $E_{\text{Cy}} > kT$. In this case almost all of the electrons will be in the ground Landau level.

The scattering cross-sections of the magnetized plasma depend on the polarizations of the incident and scattered photons. The polarization of an electromagnetic wave in a magnetized plasma can be represented as a linear combination of two circularly polarized normal modes. The right-hand circularly polarized mode is known as the extraordinary wave. Its E -field vector rotates in the same sense as the electron gyration. Thus the cross-section for scattering the extraordinary wave will have a resonance as $\omega \rightarrow \omega_{Cy}$ (Mészáros 1992). The left-hand circularly polarized mode is the ordinary wave. In a cold, magnetized plasma its cross-section is not resonant. Vacuum polarization effects will modify the cross-sections. Virtual pairs of electrons and positrons will participate in the radiation scattering. The result is that both the ordinary and extraordinary modes will be resonant (Ventura et al. 1979). Ventura et al. (1979) also found that scattering with conversion between the ordinary and extraordinary modes is important. This process enhances the depth of the cyclotron resonance feature in the emergent spectrum. The cross-section for cyclotron scattering of an extraordinary-mode photon to an extraordinary-mode photon is

$$A_{Cy} = \frac{\tau_{Cy} \left(\frac{W_{Cy}}{E_{Cy}} E \right)^2}{(E - E_{Cy})^2 + W_{Cy}^2}. \quad (1-33)$$

Natural broadening due to the short lifetime of the excited Landau levels will make W_{Cy} at least 100 eV. If the plasma is hot, Doppler broadening will make

$$W = E_{Cy} \sqrt{\frac{kT}{m_e c^2}}. \quad (1-34)$$

Other factors that will broaden the resonance are a non-uniform magnetic field or contributions from scattering regions at different heights above the neutron star's surface. If the width of the resonance was due to Doppler broadening

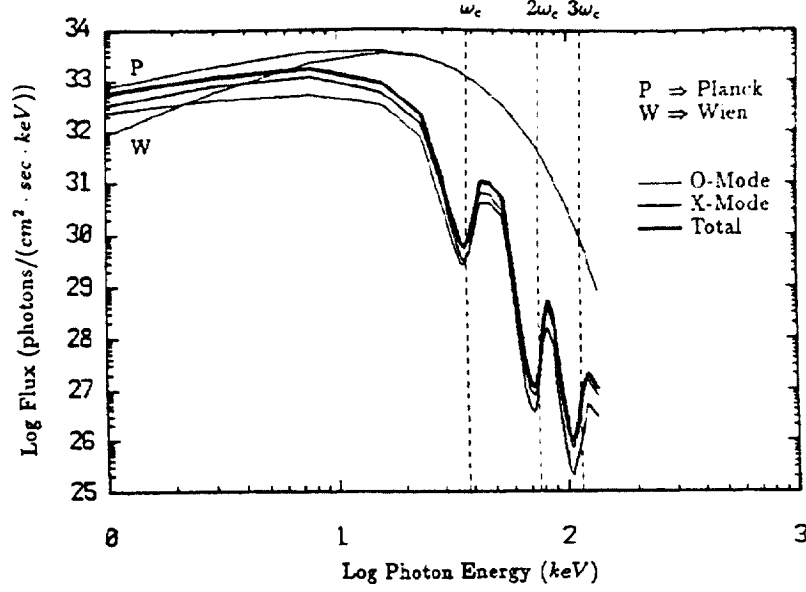


Fig. 1.7— Calculated spectrum of an AXP with a CSRF (Alexander and Mészáros 1991).

alone, the electron temperature of the plasma would be

$$kT = 511 \left(\frac{W_{Cy}}{E_{Cy}} \right)^2 \text{ keV}. \quad (1-35)$$

This is strictly an upper limit because of the other broadening mechanisms. Figure 1.7 shows a calculated spectrum for an AXP from Alexander and Mészáros (1991). The fundamental resonance is at ω_c and the harmonics at $2\omega_c$ and $3\omega_c$ are due to transitions into higher Landau levels. The calculation includes the effects of vacuum polarization, two-photon processes, and stimulated emission.

1.4.3 The Pulse Profile

The shape of the pulse profile depends on the anisotropic emission of radiation from the polar caps. It may be modified by Compton scattering or gravitational light bending. For photons whose energy is greater than the cyclotron energy, the scattering cross-section is isotropic so pulse profiles are largely determined by geometry. For photon energies below the cyclotron energy the scattering cross-section in the magnetized accretion column is highly anisotropic. The energy dependence of the pulse profile implies that the spectrum depends on pulse phase. The plasma in the accretion column is so highly magnetized that the cyclotron energy is a significant fraction of the electron rest mass. This makes a quantum treatment of the opacities necessary. The opacity of the accretion column is highly energy and direction dependent. This means that the X-ray spectrum will depend on viewing angle and thus change with pulse phase.

The radiation pressure is important as Cen X-3 radiates at near-Eddington luminosities. This may cause a radiative shock above the surface. The accretion geometry will then be a column and the radiation pattern will be a fan beam as shown in Figure 1.8. If the accreting material is stopped close to the surface the accretion column will be short like a pillbox¹ and the radiation will emerge in a pencil beam as shown in Figure 1.9. Thus luminous X-ray pulsars would be expected to emit a fan beam. However, it is possible that the effects of gravitational light bending will make this appear as a pencil beam (Mészáros and Riffert 1988).

¹A short cylindrical container used for explaining Gauss' law.

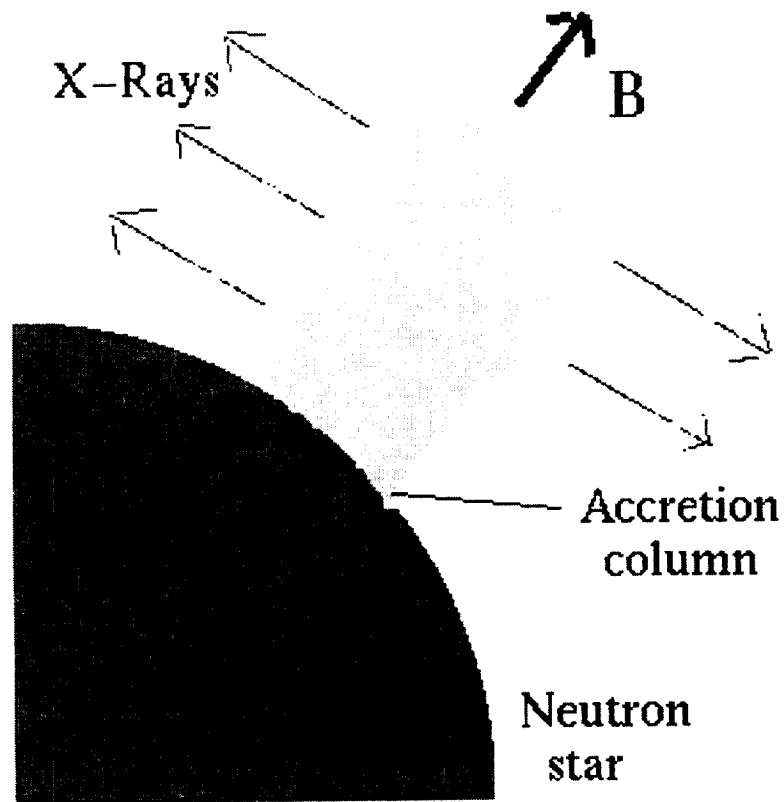


Fig. 1.8— Formation of a fan beam emission pattern. The infalling material loses its kinetic energy at a shock above the neutron star's surface and forms a tall accretion column. Most of the X-rays are emitted from the sides of the column, causing the observed intensity to be greatest when the line of sight is perpendicular to the magnetic field \mathbf{B} . The depth of any CSRF is also expected to be greatest when the intensity is greatest as the scattering cross-section is largest for photons travelling along the magnetic field.

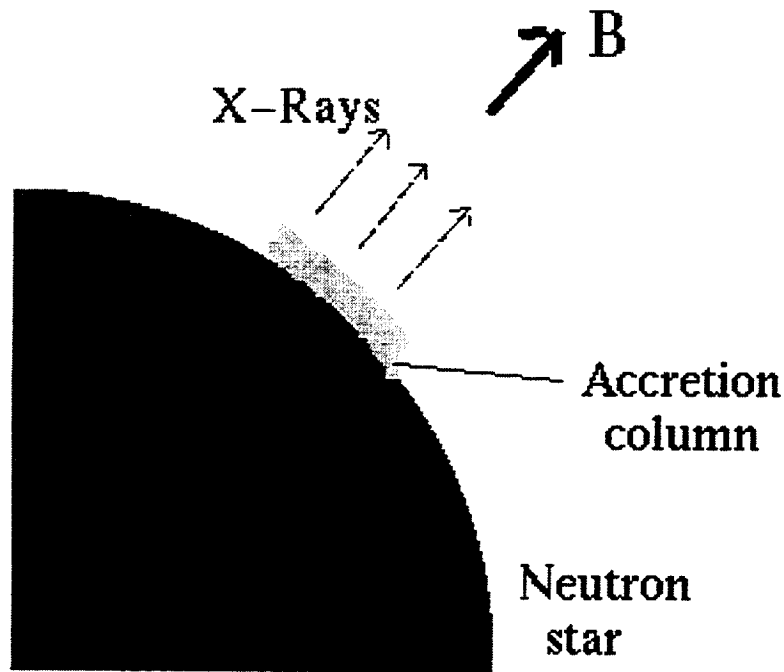


Fig. 1.9— Formation of a pencil beam emission pattern. The infalling material loses its kinetic energy near the neutron star's surface and forms a short accretion column. Most of the X-rays are emitted from the face of the column, causing the observed intensity to be greatest when the line of sight is along the magnetic field **B**. The depth of any CSRF is also expected to be least when the intensity is greatest as the scattering cross-section is smallest for photons travelling perpendicular to the magnetic field. If enough photons are scattered into a direction perpendicular to the magnetic field the CSRF may appear as an emission line when the line of sight is perpendicular to the magnetic field.

1.4.4 Line Emission

When an ion is excited to a state involving in inner-shell vacancy it may decay either by autoionization or by discrete radiative transitions. The first process is called the Auger effect. An electron from an excited ion becomes unbound leaving an ion in the next higher ionization stage. The second process is fluorescence. The probability that an excited ion will decay by fluorescence is the fluorescence yield ω .

The Doppler width of a spectral line of frequency ν_0 is given by

$$\Delta\nu = \frac{\nu_0}{c} \sqrt{\frac{2kT}{m_i}} \quad (1-36)$$

where T is the ion temperature and m_i is the ion mass. For the 6.4 keV iron K_α line this means that

$$\Delta E = (3.7 \text{ eV}) T_8^{\frac{1}{2}} \quad (1-37)$$

where T_8 is the ion temperature in units of 10^8 K. There is also collisional or pressure broadening which results in a Lorentz profile with width $\Gamma = 2\nu_{\text{col}}$ where ν_{col} is the collision frequency. If the line comes from the inner accretion disk or magnetosphere it will be broadened by orbital motion. For the purposes of spectral fitting in this work line profiles are assumed to be Gaussian. This is appropriate if thermal Doppler broadening dominates. However at high densities collisional broadening becomes important and the resulting line profile is characterized by the Voigt function

$$H(a, u) \equiv \frac{a}{\pi} \int_{-\infty}^{\infty} \frac{e^{-y^2} dy}{a^2 + (u - y)^2} \quad (1-38)$$

where

$$a \equiv \frac{\Gamma}{4\pi\Delta\nu_D} \quad (1-39)$$

and

$$u \equiv \frac{\nu - \nu_0}{\Delta\nu_D}. \quad (1-40)$$

The parameter a is a measure of the relative importance of collisional and thermal broadening. For $a \ll 1$, thermal broadening dominates and the line profile is Gaussian. For $a \gg 1$, collisional broadening dominates and the line profile is Lorentzian.

The highest resolution spectrometer used in this work is the ASCA SIS (see section 3.3.2) which has a spectral resolution of about 130 eV FWHM at the Fe K_α line energy. Thus it is safe to fit emission lines with Gaussians.

1.4.5 Iron Line Diagnostics

Iron is the end point of thermonuclear fusion. Heavier elements have to be made in supernova explosions. This makes it the most abundant of the heavy metals with a solar abundance of $N_{\text{Fe}} = 3 \times 10^{-5} N_{\text{H}}$ (Zombeck 1990). Also, the K fluorescence yield increases with Z (Kortright 1986) and is 0.34 for neutral iron (Makishima 1986). This accounts for the prominence of 6.4 keV fluorescent lines in many sources.

Spectroscopy of the iron L emission has been used to probe the properties of X-ray binaries (Kallman 1993). However, in the case of Cen X-3 the iron L emission region (0.8–1 keV; e.g. Kallman 1991) is seriously attenuated by interstellar absorption. Combined with the lower fluorescence yields (Kallman 1991) this makes iron L spectroscopy impractical in the present work.

The equivalent width of an emission or absorption feature is defined by

$$W \equiv \int_{\text{Line}} \frac{|I(E) - I(E_c)|}{I(E_c)} dE \quad (1-41)$$

where I is the observed intensity and E_c is the line centroid energy (Léna 1988). The equivalent width is a particularly useful quantity in astrophysics because it is independent of detector resolution (Thorne 1988). Makishima (1986) used Monte Carlo calculations to estimate the expected equivalent width of the fluorescent iron line for various configurations of source and scattering material. Thus, the equivalent width can be used to distinguish between different distributions of fluorescing material relative to the source. We can determine the effects of geometry on the equivalent width by separating the X-ray emission into three observed components (Inoue 1985). These are: the direct emission from the accreting object, the Thomson-scattered continuum, and the fluorescent iron line. The equivalent width of the fluorescent line depends on the relative magnitudes of these components. These are in turn determined by the geometry of the system. Figure 1.10 shows the observed and calculated equivalent width of the K_α line of neutral iron for four different configurations of source and scatterer.

The energy of the iron line may be used to determine the degree of ionization of the iron in the plasma. This can be used as a diagnostic of the ionization parameter for a photoionized plasma or the temperature of a collisional plasma. Figure 1.11 shows how the Fe K_α line energy varies with ionization stage. Electric and magnetic dipole spectra were calculated (Cowan 1981) with an intrinsic line width of 25 eV. The K_α lines were fitted with Gaussian profiles to obtain the centroid energies. The iron line energy is close to 6.4 keV for ionization stages below Fe XVIII. Thus when I refer to un-ionized iron in this dissertation I include Fe I–Fe XVIII.

Radiation from a luminous HMXB will ionize the stellar wind of its early-type companion. Recombination of Fe XXVII to Fe XXVI and Fe XXVI and Fe XXV

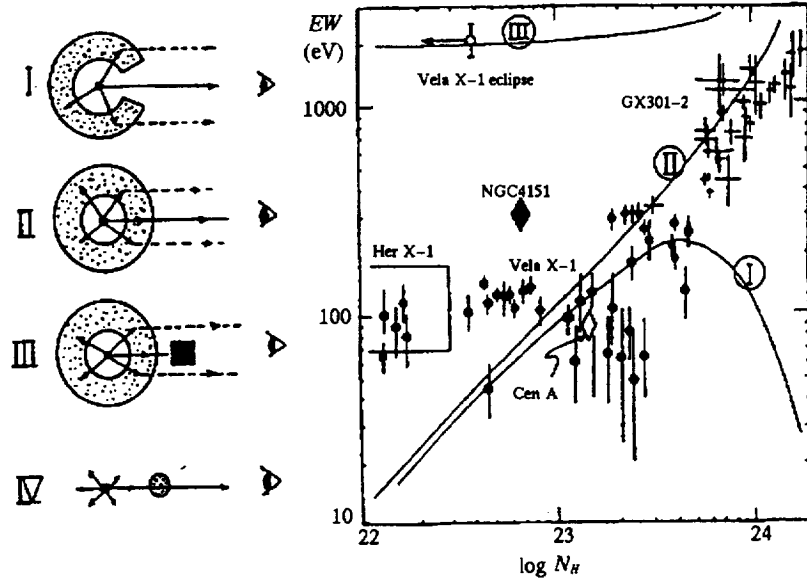


Fig. 1.10— Dependence of observed equivalent width on source geometry (from Makishima 1986). The spectrum of the central source is assumed to be a power law with photon index $\alpha = 0.8$.

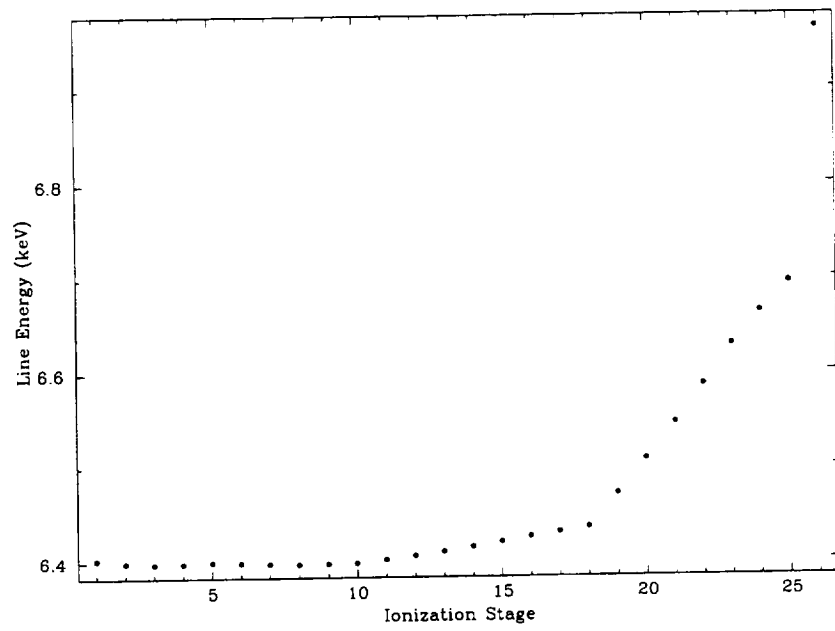


Fig. 1.11— Dependence of Fe K α line energy on ionization stage.

will produce emission lines at 6.7 and 6.9 keV. The recombination mechanisms are radiative recombination and dielectronic recombination followed by cascading. Radiative recombination is the opposite process to photoionization and dielectronic recombination is the opposite process to autoionization. Photoionization and recombination will balance each other. The state of a photoionized, optically thin plasma may be characterized by the ionization parameter $\xi = L/(n_e r^2)$ (e.g. Kallman and McCray 1982) where n_e is the electron density, L is the X-ray luminosity, and r is the distance to the source.

The photoionized plasma surrounding a system similar to Cen X-3 has $\log_{10} \xi > 10^4$ so it will be transparent to X-rays provided the electron density is not too high. The optical depth for Thomson scattering will be

$$\tau = N_H \sigma_T \approx 6.7 \times 10^{-3} N_{22} \quad (1-42)$$

where N_{22} is the electron column density in units of 10^{22} cm^{-2} .

1.5 Timing Properties of High-Mass X-Ray Binaries

1.5.1 Dynamical Timescales for High-Mass X-Ray Binaries

The temporal behavior depends on several characteristic times. The most obvious is the rotation period of the neutron star which gives rise to the observed coherent pulsations. The orbital period is another. Some X-ray binaries such as the LMXB pulsar Her X-1 exhibit third periods due to a precessing accretion

disk (e.g. White et al. 1995, and references therein). The Keplerian rotation period of the inner accretion disk is another observationally important timescale. The beat period between this and the pulsar rotation period may be manifested as quasi-periodic modulations of the light curve (see Section 1.5.5). The dynamical timescales in the accretion column close to the neutron star are ~ 0.1 ms (van der Klis 1997).

1.5.2 The X-Ray Light Curve

The X-ray emission is influenced by the source's physical characteristics. The luminosity gives a direct measure of the instantaneous mass accretion rate \dot{M} . The X-ray light curve provides information on fluctuations in \dot{M} .

In the case of an eclipsing binary the eclipse duration can be used to obtain the eclipse half-angle θ_e as shown in Figure 1.12. This may then be used to constrain the inclination angle i (see Figure 1.13). If the tidally distorted companion is characterized by a sphere of the same volume, its radius R_c is given by (Joss and Rappaport 1984)

$$R_c \approx a \sqrt{\cos^2 i + \sin^2 i \sin^2 \theta_e}. \quad (1-43)$$

If R_c is taken to be β times the Roche lobe radius R_L , i is given by

$$\sin i \approx \frac{\sqrt{1 - \beta^2 \left(\frac{R_L}{a}\right)^2}}{\cos \theta_e} \quad (1-44)$$

where R_L may be computed from Equation 1-9.

1.5.3 Pulse Arrival Time Analysis

The regular pulsations of X-ray binary pulsars provide us with accurate clocks that can be used to probe the dynamics of the system. The time at which the

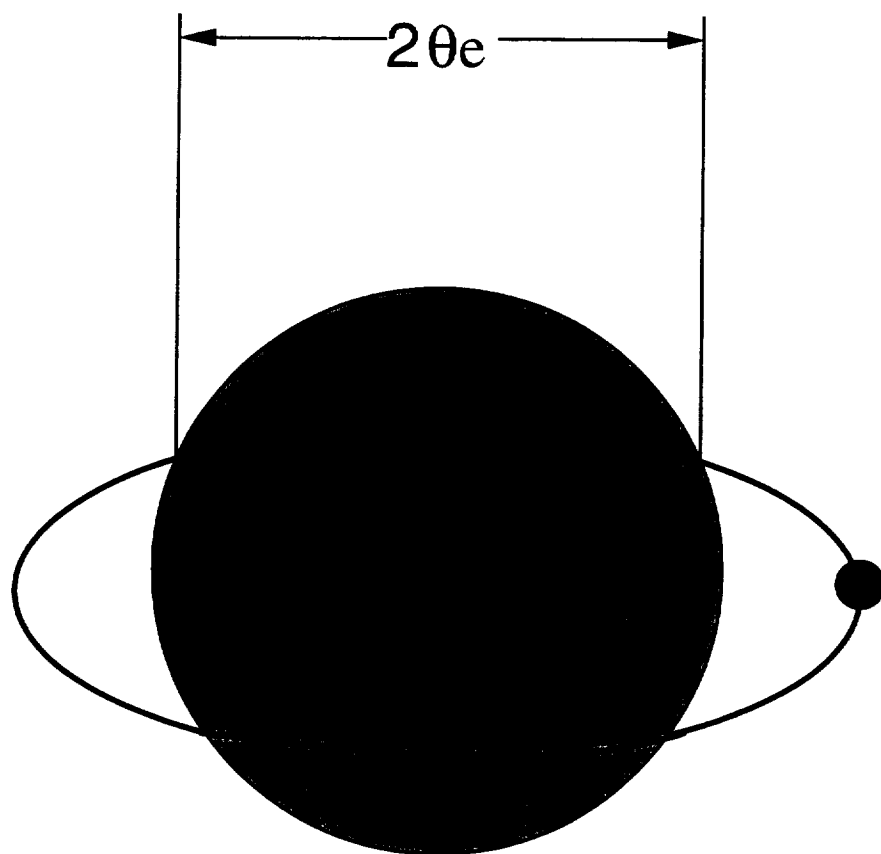


Fig. 1.12— A high-mass X-ray binary system as seen from Earth showing the definition of the eclipse half-angle θ_e .

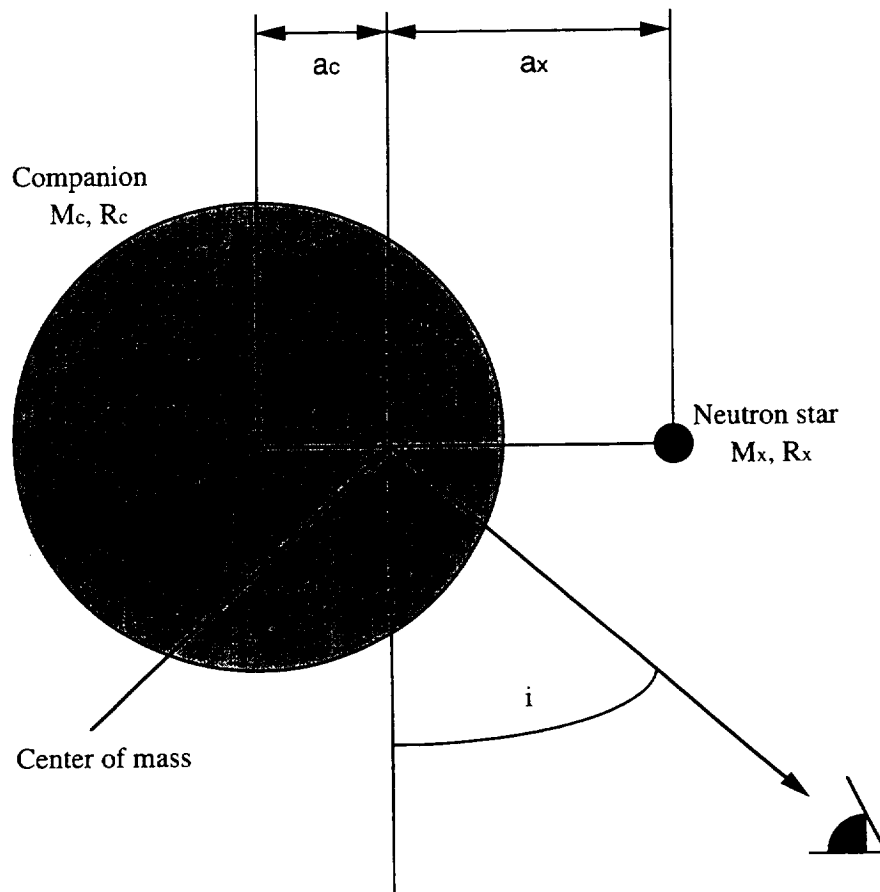


Fig. 1.13— A high-mass X-ray binary system showing the definitions of the various geometrical parameters.

n^{th} pulse is emitted is

$$t'_n = t_0 + P(n) \quad (1-45)$$

where

$$P(n) = P_0 n + \frac{1}{2} \dot{P} P_0 n^2 + \dots \quad (1-46)$$

takes into account variations in the intrinsic pulse period.

As the pulsar moves in its orbit pulse arrival times will be delayed or hastened by up to the light travel time across the projected semi-major axis of the orbit $a_x \sin i$. This is ~ 40 s for Cen X-3. The arrival time t_n of the n^{th} pulse is

$$t_n = t_0 + P(n) + \frac{a_x \sin i}{c} F(e, \omega, \tau, \nu) \quad (1-47)$$

where the function $F(e, \omega, \tau, \nu)$ describes the orbit of the neutron star about the center of mass. The orbit is elliptical with eccentricity e . The longitude of periastron ω is the angle between the line of sight and the major axis. The time of periastron passage is τ . The position of the neutron star in its orbit is described by the mean anomaly $\theta = 2\pi(t - \tau)/P_{\text{orb}}$. The function F has the form

$$F(e, \omega, \tau, \nu) = (1 - e^2) \frac{\sin(\nu + \omega)}{1 + e \cos \nu} \quad (1-48)$$

where the true anomaly ν may be found from the relations

$$\begin{aligned} \tan \frac{\nu}{2} &= \sqrt{\frac{1+e}{1-e}} \tan \frac{E}{2} \\ E - e \sin E &= \theta. \end{aligned} \quad (1-49)$$

For a circular orbit the arrival time t_n of the n^{th} pulse is

$$t_n = t_0 + P(n) + \frac{a_x \sin i}{c} \cos \left(\frac{2\pi(t'_n - T_{\text{ecl}})}{P_{\text{orb}}} \right) \quad (1-50)$$

where T_{ecl} is the time of mid-eclipse, and P_{orb} is the orbital period. If the eccentricity of the orbit is small this circular ephemeris may be used to obtain

an initial estimate of the orbital parameters. Then if terms of order e^2 and higher are ignored the residuals from the fit to the arrival times *versus* pulse number are (Sterne 1941; Deeter et al. 1981)

$$\begin{aligned}
\delta t_n = & \delta t_0 + n\delta P_0 + \frac{1}{2}n^2 P_0 \dot{P}_0 \\
& + \delta \left(\frac{a_x \sin i}{c} \right) \sin l_n - \frac{2\pi}{P_{\text{orb}}} \frac{a_x \sin i}{c} \cos l_n \\
& + \frac{2\pi}{P_{\text{orb}}^2} \frac{a_x \sin i}{c} \delta P_{\text{orb}} (t'_n - E_0) \cos l_n \\
& - \frac{3}{2} \frac{a_x \sin i}{c} e \sin \omega + \frac{1}{2} e \cos \omega \sin 2l_n \\
& - \frac{1}{2} \frac{a_x \sin i}{c} e \sin \omega \cos 2l_n.
\end{aligned} \tag{1-51}$$

Here $l_n = 2\pi(t'_n - E_0)/P_{\text{orb}} + \frac{\pi}{2}$ is the mean orbital longitude at time t'_n and $E_0 \approx T_{\text{ec1}}$ is a time when the mean orbital longitude is 90° . With the substitutions $g = e \sin \omega$ and $h = e \cos \omega$ the expression becomes linear in the parameters omitted from the circular ephemeris (\dot{P}_0 , g , and h) and in the differential corrections to the orbital parameters (δt_0 , δP_0 , $\delta \left(\frac{a_x \sin i}{c} \right)$, $\delta \tau$, and δP_{orb}). The arrival time residuals may be fitted to Equation 1-51 to obtain a better estimate of the orbital parameters. This may be compared with the arrival times to obtain a new set of residuals. The process can be iterated until convergence is obtained.

The arrival times provide information about the orbit and changes in the orbital period. Intrinsic variations in the spin period trace the angular momentum accretion rate \dot{J} .

By fitting the arrival times, the mass function of the primary

$$f(M_x) = \frac{4\pi^2 (a_x \sin i)^3}{GP_{\text{orb}}^2} \tag{1-52}$$

can be found. If there are optical measurements of Doppler shifts in lines from the companion the companion's mass function can be found. Then the mass

ratio is

$$q \equiv \frac{M_x}{M_c} = \frac{K_c P_{\text{orb}} \sqrt{1 - e^2}}{2\pi a_x \sin i} \quad (1-53)$$

where K_c is the amplitude of the Doppler velocity curve measured from optical lines. The main uncertainties are usually in K_c and θ_e . θ_e can be difficult to measure if the stellar wind has a significant optical depth. If θ_e is overestimated it will result in a value for M_x that is too low. K_c can be difficult to measure because of the extended nature of the companion and its wind.

1.5.4 Interaction of the accretion disk with the magnetosphere

One property which HMXB do not share with the rotation-powered pulsars is the presence of accreting matter that can spin the star up or down. How this occurs depends on how the magnetic field of the neutron star is coupled to the accretion flow.

In the case of a HMXB with a large ($\gtrsim 10^{11}\text{G}$) magnetic field the accretion disk cannot extend all the way down to the neutron star's surface. This is because movement of the plasma perpendicular to field lines is inhibited due to its electrical conductivity. The region surrounding the neutron star in which the flow of matter is dominated by the magnetic field is the magnetosphere. Figure 1.14 shows how the motion of the infalling matter is controlled by the magnetic field. We can make a very crude estimate of its size by equating the magnetic pressure with the ram pressure of the infalling material for spherical accretion. The radius at which these two pressures balance is the Alfvén radius

r_A .

$$r_A = 3.2 \times 10^8 \dot{M}_{17}^{-\frac{2}{7}} \mu_{30}^{\frac{4}{7}} \left(\frac{M}{M_\odot} \right)^{-\frac{1}{7}} \text{ cm.} \quad (1-54)$$

Here μ_{30} is the magnetic dipole moment of the neutron star in units of 10^{30} G cm^3 and \dot{M}_{17} is the mass accretion rate in units of 10^{17} g s^{-1} . In terms of the luminosity $\dot{M} = L/c^2 \varepsilon$ where ε is the energy conversion efficiency for 2-10 keV X-rays. This means that $\dot{M}_{17} = 1.1 L_{37}/\varepsilon_{0.1}$ where $\varepsilon_{0.1} = \varepsilon/10 \sim 1$. Thus

$$r_A = 3.1 \times 10^8 L_{37}^{-\frac{2}{7}} \varepsilon_{0.1}^{2/7} \mu_{30}^{\frac{4}{7}} \left(\frac{M}{M_\odot} \right)^{-\frac{1}{7}} \text{ cm.} \quad (1-55)$$

The magnetosphere co-rotates with the neutron star. If we make the simplistic assumption that the inner edge of the accretion disk is at the magnetospheric radius r_m , there are three possible cases for spin-period change depending on the angular velocity of the inner accretion disk. We define the co-rotation radius R_{co} as the radius at which the Keplerian orbital angular velocity $\Omega_K = \sqrt{\frac{GM_s}{r^3}}$ equals the neutron star's spin angular velocity Ω_0 . If $r_m < r_{co}$, the inner disk will be rotating faster than the magnetosphere and it will exert a positive torque which will spin up the pulsar. If $r_m > r_{co}$, the inner disk will be rotating more slowly than the magnetosphere and it will exert a negative torque which will cause the pulsar to spin down. In this simple picture, for $r_m = r_{co}$ there will be no net torque. These results hold for a prograde disk. Clearly, for a retrograde disk, the net torque on the neutron star will always be negative. The Alfvén radius r_A depends on the mass accretion rate so it is possible for the neutron star to have episodes of spinning up and spinning down.

The disk-torque model predicts that the rate of change of the spin period will depend on luminosity. Cen X-3 and Her X-1 were found to have spin-up rates an order of magnitude smaller than those predicted. Treating the neutron

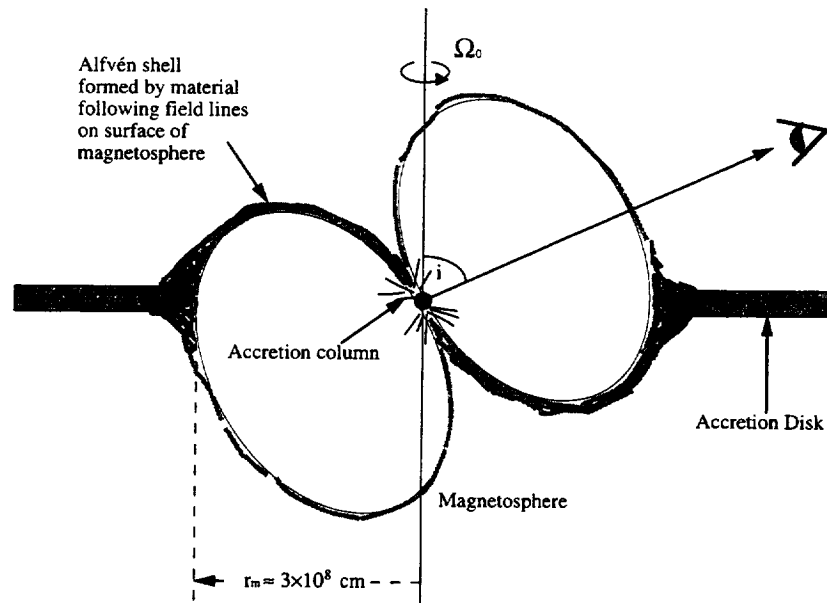


Fig. 1.14— An accreting X-ray pulsar. Inside the magnetosphere the the infalling matter flows along the magnetic field lines. The dimensions of this system have been chosen to be similar to those of Cen X-3. The radius of the neutron star ($\sim 10 \text{ km}$) has been exaggerated by a factor of 10 for clarity.

star and magnetosphere as a unit, Lamb et al. (1973) considered the transport of angular momentum across a surface just outside r_0 and found

$$\frac{\dot{P}}{P} = \frac{\dot{M}}{M_x} \left(\frac{M_x}{I_x} \frac{dI_x}{dM_x} - \frac{l(r_0)}{l_x} \right) + \frac{N'}{I_x \Omega} \quad (1-56)$$

where I_x is the moment of inertia of the neutron star, $l(r_0)$ is the component parallel to Ω of the specific angular momentum of matter just outside the surface, $l_x = I_x \Omega / M_x$ is the specific angular momentum of the neutron star, and N' is the sum of the external magnetic and viscous torques acting just outside the surface. For a Keplerian disk $l(r_0) = \sqrt{GM_x r_0}$ and for typical neutron star equations of state (Shapiro and Teukolsky 1983)

$$\frac{M_x}{I_x} \frac{dI_x}{dM_x} \approx 1. \quad (1-57)$$

Then, assuming $N' = 0$ (Shapiro and Teukolsky 1983),

$$-\dot{P} \approx 5 \times 10^{-5} \left(\mu_{30}^{\frac{2}{7}} R_6^{\frac{6}{7}} \left(\frac{M_x}{M_\odot} \right)^{-\frac{3}{7}} I_{45}^{-1} \right) \left(P L_{37}^{\frac{3}{7}} \right)^2 \text{ s yr}^{-1} \quad (1-58)$$

where I_{45} is the neutron star's moment of inertia in units of 10^{45} g cm^2 .

Ghosh et al. (1977) and Ghosh and Lamb (1979a,b) assumed that the neutron star's magnetic field threaded a thin disk. In a broad outer zone the disk is Keplerian and exerts a negative torque on the neutron star through the magnetic field. The disk makes the transition from Keplerian rotation to co-rotation with the magnetosphere in a narrow inner zone. The torque exerted by this region of the disk on the neutron star depends on whether the magnetosphere radius r_m is larger or smaller than the corotation radius r_{co} . The radius at which the disk deviates from Keplerian rotation is $r_0 \gtrless r_m$. Then if $r_{co} < r_0$ the disk in the inner transition region is rotating more slowly than the magnetosphere and will exert a negative torque on it. If $r_{co} > r_0$ the disk in this region rotates faster than

the magnetosphere and will exert a positive torque. Ghosh and Lamb (1979a) found that $\delta \approx 0.03r_0$ and

$$r_0 = \xi r_A \approx 0.52 r_A. \quad (1-59)$$

The fastness parameter ω_s is defined by (Elsner and Lamb 1977)

$$\omega_s \equiv \frac{\Omega_s}{\Omega_K(r_0)} = \left(\frac{r_m}{r_{co}} \right)^{\frac{3}{2}}. \quad (1-60)$$

Ghosh and Lamb (1979b) parameterized the total torque N in terms of a dimensionless torque $n(\omega_s)$ and the material torque $N_0 \equiv \dot{M} \sqrt{GM_x r_m}$ (Pringle and Rees 1972) exerted by a Keplerian accretion disk so that

$$N_s \approx n(\omega_s) N_0 \quad (1-61)$$

They found that $n(\omega_s)$ could be fitted by the approximate expression

$$n(\omega_s) \approx 1.4 \left(\frac{1 - \frac{\omega_s}{\omega_c}}{1 - \omega_s} \right). \quad (1-62)$$

There is a critical value of the fastness parameter, $\omega_c \approx 0.8-0.9$ above which the neutron star will spin down and below which the neutron star will spin up. For $\Omega_s \gg \omega_c$, accretion to the neutron star will cease because of the propeller effect (Davidson and Ostriker 1973). Because $n(\omega_c) = 0$ there will be an equilibrium pulsar spin period P_{eq} for which $\dot{P} \approx 0$ on average. Fluctuations in \dot{M} can still cause episodes of spin-up and spin-down. With the external magnetic torques in N' absorbed into N , Equation 1-58 becomes (Ghosh and Lamb 1979b)

$$-\dot{P} \approx 5 \times 10^{-5} \left(\mu_{30}^{\frac{2}{7}} n(\omega_s) R_6^{\frac{6}{7}} \left(\frac{M_x}{M_\odot} \right)^{-\frac{3}{7}} I_{45}^{-1} \right) \left(PL_{37}^{\frac{3}{7}} \right)^2 \text{ s yr}^{-1} \quad (1-63)$$

The relationship between average spin-up rate and luminosity for several different accreting pulsars is shown in Figure 1.15. All of the systems plotted agree

with the theoretical prediction except for Vela X-1. This confirms the presence of an accretion disk in these systems. Vela X-1 is believed to be a wind accretor, although Anzer and Börner (1995) have suggested that a Keplerian disk may form just outside the magnetosphere and that this may account for the magnitude of the random variations in the system’s pulse period.

Wang (1987) assumed a different threading parameter for the magnetic field in the inner accretion disk. Wang found that $\xi \approx 1$ and thus the magnetospheric radius is $r_m = \xi r_A \approx r_A$.

1.5.5 Quasi-Periodic Oscillations

Quasi-periodic oscillations (QPOs) provide information about the inner accretion disk and its interaction with the magnetosphere. The beat frequency mass accretion model assumes that the QPO is the beat frequency between the magnetospheric rotation and clumps in the inner accretion disk. The mass accretion rate is enhanced when these clumps connect to open field lines, yielding a quasi-periodic modulation of the X-ray luminosity. A test of this theory is the prediction that the QPO frequency should be luminosity-dependent.

A new class of fast QPOs, called “kilohertz QPOs”, has recently been discovered with NASA’s RXTE satellite (e.g. van der Klis 1997). These QPOs are probably associated with the rotation periods of neutron stars in LMXB. Photon bubble oscillations (Klein et al. 1996) are another possible mechanism that could generate kilohertz QPOs in AXP. These might be produced by the formation of radiation-pressure dominated bubbles in a locally super-Eddington accretion column.

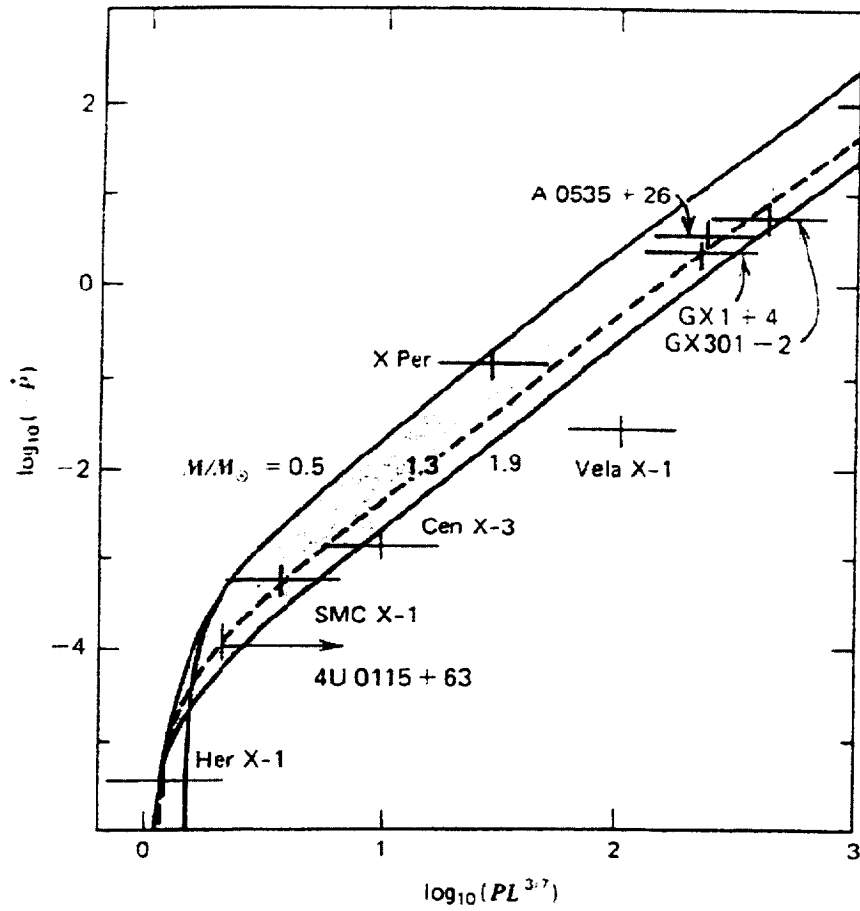


Fig. 1.15— Relationship between spin-up rate and luminosity for accreting pulsars (Shapiro and Teukolsky 1983, after Ghosh and Lamb (1979b)). The shaded region represents a range of neutron star masses between 0.5 and $1.9M_{\odot}$. The magnetic moment is assumed to be $\mu_{30} = 0.48$ for all of the systems shown.

Chapter 2

Non-Dispersive X-Ray Spectrometers

In this chapter I give a brief overview of the types of detectors that have been used to acquire the data used in this dissertation. These are all non-dispersive detectors. Their main advantage over dispersive detectors such as diffraction gratings and Bragg crystal spectrometers is their much greater quantum efficiency over a large energy band. I also describe novel cryogenic detectors which will be used in future missions. The driving force behind the development of these detectors is the need for better spectral resolution. To illustrate the importance of spectral resolution, Figure 2.1 shows the iron K region of a coronal spectrum as it might appear when observed with spectrometers with resolutions of 1, 10, and 100 eV. A resolution of 100 eV is slightly better than that of present-day X-ray observatories. With a resolution of 1 eV it is possible to resolve the K_{α} lines of intermediate ionization stages of iron.

X-rays are efficient ionizers and this is how they may be most easily detected. Early detectors were proportional counters. Positional information came from mechanical collimators, coded apertures, and shadow masks. The development of grazing-incidence X-ray mirrors such as those flown on the Einstein satellite allowed high resolution X-ray images of celestial objects to be made.

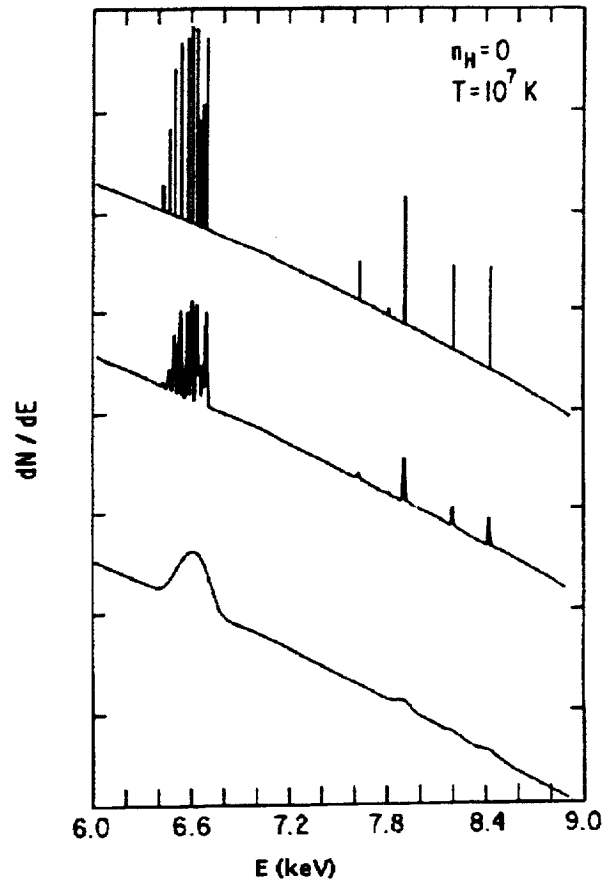


Fig. 2.1— The iron line spectrum of a coronal plasma as it might appear when observed with detectors with energy resolutions of (top to bottom) 1, 10, and 100 eV.

X-ray telescopes use Wolter-type geometry (VanSpeybroeck and Chase 1972), or an approximation, in which incident paraxial X-rays are reflected first by a paraboloid and then by a hyperboloid to form an image (see Figure 3.2).

2.1 Proportional Counters

In a proportional counter a potential difference of typically 2 keV is maintained across a gas-filled chamber. When an atom of the gas absorbs an X-ray a photoelectron is ejected along with Auger electrons. These electrons ionize more atoms resulting in an electron cloud whose size is proportional to the X-ray energy. The electron cloud drifts towards the anode. When it reaches the high-field region near the anode the electrons gain enough kinetic energy to collisionally excite an avalanche of electrons. This results in an amplification of the signal by a factor known as the gas gain G which is typically 10^3 – 10^5 . In order to maximize the photoelectric cross-section for X-rays a high- Z gas like Ar or Xe is used. The energy resolution of a proportional counter is limited by $\Delta E^2 = FN$ where $F \sim 0.1$ is the Fano factor and N is the number of electron-ion pairs produced. It also depends on G . N depends on the mean energy required to produce an electron which is 26.2 eV for Ar. The Fano factor takes into account the fact that, for a given X-ray photon, the creation of each ion pair is not statistically independent.

There are special problems associated with operating proportional counters in space. The window must have a low X-ray absorption cross-section and must also be able to withstand the pressure difference between the enclosed gas and a vacuum. The window materials that are usually used are beryllium or alu-

minized mylar. The particle background rate is proportional to the volume. For background rejection a guard detector, usually another gas cell surrounded by a shield opaque to X-rays, is used to identify cosmic ray events. Another way to identify charged-particle events is by rise-time discrimination. The absorption of an X-ray photon produces a localized electron cloud and thus a pulse with a fast rise-time. A charged particle will leave an ionization trail in the detector which results in a broader pulse with a slower rise-time. Events with slow risetimes can be tagged by the detector electronics for rejection. CH_4 or another hydrocarbon is added to the gas mixture to quench the discharge quickly. However for high counting rates the detector will have a significant dead time. The detector's response to monochromatic X-rays will have an escape peak at a lower energy due to the finite probability that the absorbing atom will emit a K_α X-ray photon that escapes the gas cell instead of an Auger electron. Position sensitivity may be obtained by using multiple anodes and measuring electron drift times.

2.1.1 Gas Scintillation Proportional Counters

In a gas scintillation proportional counter (GSPC) the electron cloud is accelerated through a further chamber where it collisionally excites the atoms of the gas. These recombine with the emission of UV scintillation photons which are detected by a photomultiplier tube. If this is position sensitive an image of the source may be obtained. The GSPC has better resolution than the proportional counter because there is no avalanche so the noise is not amplified by the gas gain G . Also the energy required to produce a scintillation photon is small, giving better counting statistics.

2.2 Solid-State Ionization Detectors

2.2.1 Scintillation Detectors

For energies higher than a few tens of keV, the X-ray cross-section of gas-filled detectors becomes too small. Detectors that use scintillating crystals as the absorbing volume have better efficiency. Background rejection is obtained by surrounding the detector with a guard scintillator. Photomultiplier tubes detect the scintillations from both crystals. X-rays from the source being observed enter the detector through a mechanical collimator and do not pass through the guard volume. Events resulting in scintillations from both volumes can be recognised by their pulse shape and can thus be rejected. Such an arrangement is known as a phosphor sandwich or phoswich detector.

2.2.2 Si(Li) Detectors

This type of detector is essentially a reverse-biased silicon diode. X-rays are absorbed in the depletion layer and cause the formation of electron-hole pairs. The charge collected at the anode is converted to a voltage by a JFET or a similar amplifier. This results in a voltage pulse that is proportional to the number of pairs created and thus to the incident X-ray energy. The resolution is determined by the energy required to create an electron-hole pair (3.8 eV) and also by the Fano factor which is ~ 0.1 for silicon.

In order to maximize the X-ray absorption cross-section the volume of the depletion region must be made as large as possible. This is done by creating an insulating layer between the anode and cathode. Such a detector is also known as a p-i-n (p-type-insulator-n-type) diode. However Si is an intrinsic p-type semi-

conductor so it has a slight excess of holes. This means that thermally excited charge carriers cause leakage currents across the depletion layer which make detection of the pulses produced by X-rays difficult. Doping can compensate for excess electron acceptors but it is difficult to dope such large volume uniformly. Lithium diffuses easily into silicon and can provide the required compensation. The insulating Li-drifted layer is the X-ray-sensitive region. One disadvantage of Si(Li) detectors is that they have to be stored in liquid nitrogen or the lithium will diffuse out of the depletion layer.

2.2.3 Charge-Coupled Devices

A charge-coupled device (CCD) is an array of metal-oxide-semiconductor (MOS) capacitors which can accumulate and store charge due to their capacitance. A cross-section of a single MOS capacitor is shown in Figure 2.2 (Gendreau 1995). When the device is properly biased electrons see a potential well in which they can be trapped. The active region of this device is the depletion region. Free charge resulting from X-ray absorption here is accumulated in the potential well of the MOS capacitor.

The array is read out by transferring the charge from one MOS capacitor to its neighbor on one side. This is done by clocking the gate voltages. In a three-phase CCD array each pixel has three gate electrodes. In each row of pixels, the corresponding electrodes on each pixel are connected. Figure 2.3 shows how charge is transferred. To avoid smearing of the X-ray image the readout time is a small fraction of the integration time. The charge from the imaging CCD is transferred to another CCD array called the frame storage array. While the imaging array is integrating an image again the charge in the frame store array

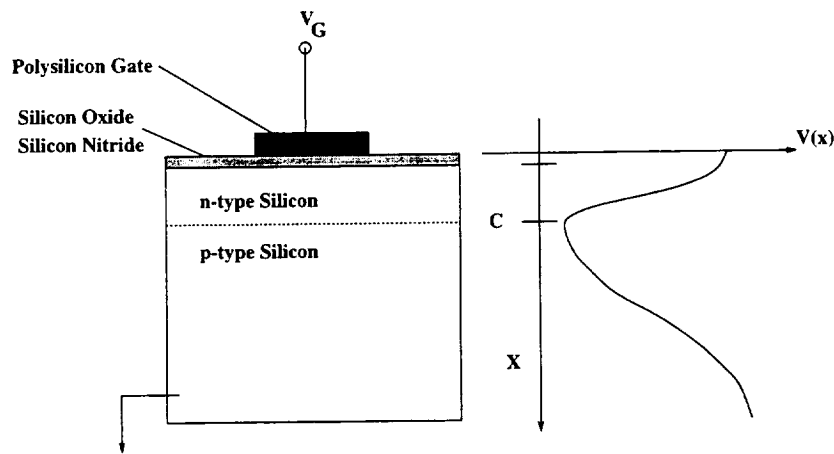


Fig. 2.2— Cross-section of a MOS capacitor showing the potential function. From Gendreau (1995).

is transferred to a serial register and then to the gate of a JFET or a similar charge-sensitive amplifier. This results in a train of voltage pulses. The spatial position of the original pixel can be deduced from the pulse's position in the train. The size of the pulse is proportional to the collected charge and thus to the energy deposited by the incident X-ray.

2.3 Thermal X-Ray Detectors

Moseley et al. (1984) proposed X-ray microcalorimeters as a means of simultaneously attaining high spectral resolution and throughput. In contrast to a bolometer which measures an integrated radiant flux, a calorimeter measures the energy of **individual** X-ray photons by the temperature rise they cause when absorbed in a small sensing element. The concept of a calorimeter is similar to that of a bolometer. However it is subject to more stringent design constraints

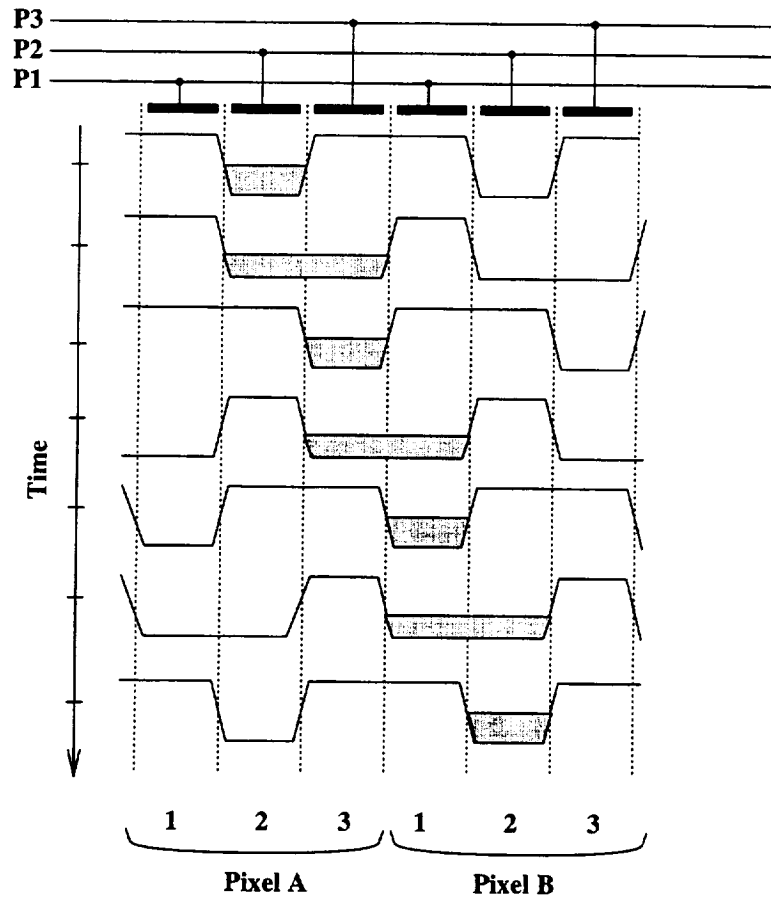


Fig. 2.3— Charge transfer in a three-phase CCD array. From Gendreau (1995). At the top are the electrodes. The curves under these represent voltage profiles at different times and the shaded regions in the curves represent the trapped charge.

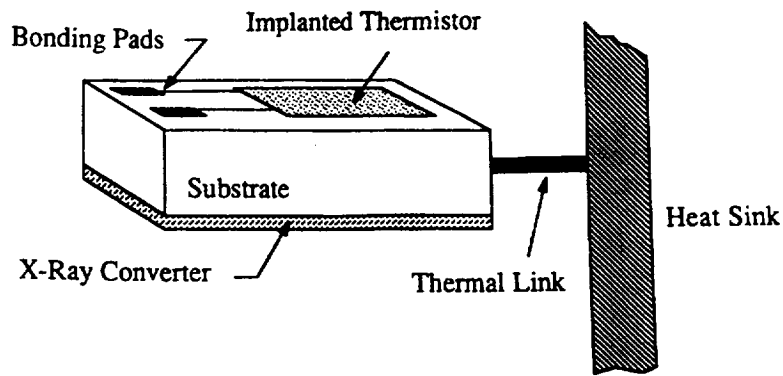


Fig. 2.4— Concept of a microcalorimeter.

due to the necessity of thermalizing individual photons rapidly. Figure 2.4 is a schematic of an X-ray microcalorimeter. An X-ray photon hits an absorber which converts its energy into heat. In its simplest form ($\Delta T \ll T$) the resulting temperature rise is $\Delta T = \frac{E}{C}$ where E is the energy of the photon and C is the heat capacity of the calorimeter. This is sensed by a thermometer, typically consisting of a doped semiconductor. A thermal link to a heat bath conducts heat away from the calorimeter so that the temperature decays exponentially to the baseline value with a thermal time constant $\tau = \frac{C}{G}$ where G is the thermal conductance of the link.

For this device to be useful several conditions must be met. The heat capacity C must be small enough to produce a significant temperature rise. Because the heat capacities of most of the materials used to construct calorimeters vary as T^3 as $T \rightarrow 0$ this may be achieved by operating the device at low temperatures, typically below 100 mK. For applications over the 1-10 keV band, the absorber is a significant contributor to the total heat capacity. The main contributor to the

heat capacity of the calorimeter is the absorber. Normal metals such as gold and silver are excellent absorbers and thermalizers of X-ray photons but their large electron heat capacities render them unsuitable for practical devices. Alternative choices for absorbers are semimetals such as HgTe or superconductors such as tin (e.g. Moseley et al. 1992).

The absorber must have a high X-ray opacity and a low heat capacity, and must convert the photon's energy into phonons in a time much less than τ . Superconductors have lower heat capacities than normal metals. However, in a superconductor much of the energy of a deposited X-ray goes towards breaking Cooper pairs into quasiparticles. When these recombine into Cooper pairs this energy is converted into phonons. One problem is that the quasiparticles can take a long time to recombine which degrades the resolution. Raising the normal electron concentration can reduce this effect. Thus heat capacity and recombination time must be traded off to obtain optimum performance (Stahle et al. 1993).

2.3.1 Calorimeters with Resistive Thermometers

X-Ray microcalorimeters have been constructed by anisotropic etching of single-crystal silicon. This fabrication technique is described by Peterson (1982). The calorimeter volume consists of a back etched panel of silicon with an X-ray absorber and an ion implanted thermistor. This is suspended on four thin silicon legs which provide the thermal link to the heat sink and carry electrical connections. These devices have attained a resolution of 7.3 eV at 6 keV (e.g. McCammon et al. 1993).

An order of magnitude estimate of the best possible energy resolution may be

obtained from the thermodynamic energy fluctuations in the detector (Moseley et al. 1984). The effective number of phonon modes in the detector is $N = C/k_B$. The typical phonon mode has occupation number and rms fluctuation 1 and mean energy $k_B T$. Thus the mean square energy fluctuation is

$$\langle \Delta U^2 \rangle = (k_B T)^2 N = k_B T^2 C. \quad (2-1)$$

It is possible in principle to obtain energy resolutions better than that in Equation 2-1 through negative electrothermal feedback (Mather 1982) if the resistive thermometer is biased so that the temperature derivative of the power dissipation is negative:

$$\frac{dP}{dT} < 0. \quad (2-2)$$

If this condition holds the absorption of an X-ray photon causes the temperature to increase which causes the bias power dissipation to drop. This negative electrothermal feedback tends to return the calorimeter to the base temperature as the thermal energy deposited by the X-ray photon is compensated for by a drop in Joule heating. This allows thermal equilibrium to be reestablished faster than if the deposited heat had to be conducted to the thermal bath. The calorimeter thus has an effective time constant $\tau_{\text{eff}} < \tau$. This means that, when the effects of electrothermal feedback are taken into account, microcalorimeters can be faster and allow higher count rates than those implied by the thermal time constant τ . Electrothermal feedback also suppresses the Johnson noise for frequencies $\ll 1/\tau$. How the detector should be biased depends on the sign of the temperature coefficient of the thermistor

$$\alpha = \frac{d \log R}{d \log T} = \left(\frac{T}{R} \right) \frac{dR}{dT}. \quad (2-3)$$

In the case of ion-implanted thermistors where current is carried by electron hopping

$$R(T) \propto \exp\left(\frac{T_0}{T}\right)^\gamma \quad (2-4)$$

with $\gamma \sim \frac{1}{2}$ so that $\alpha < 0$. Thus, if the thermistor is current biased, the Joule power dissipated will be $P = I^2 R(T)$ so that

$$\frac{dP}{dT} = I^2 \frac{dR}{dT} = \frac{I^2 R}{T} \alpha = \frac{P}{T} \alpha < 0. \quad (2-5)$$

If, however, $\alpha > 0$, as in the case of the transition edge detectors discussed in Section 2.3.1, the detector should be voltage biased. Then $P = V^2/R(T)$ and

$$\frac{dP}{dT} = -\frac{V^2}{R^2} \frac{dR}{dT} = -\frac{V^2}{TR} \alpha = -\frac{P}{T} \alpha < 0. \quad (2-6)$$

If noise from the amplifier and load resistor are neglected the square of the noise equivalent power has two parts:

$$\text{NEP}^2 = \text{NEP}_{\text{Johnson}}^2 + \text{NEP}_{\text{phonon}}^2 \quad (2-7)$$

where

$$\text{NEP}_{\text{Johnson}}^2 \propto 4k_B T P (1 + \omega^2 \tau^2) \quad (2-8)$$

is due to Johnson noise and P is the dc power dissipated in the thermometer. The second term in Equation 2-7 is due to fluctuations in heat transfer across the thermal link:

$$\text{NEP}_{\text{phonon}}^2 = 4k_B T^2 G. \quad (2-9)$$

It can be shown that the energy resolution is

$$\Delta U_{\text{rms}} = \xi \sqrt{k_B T_0^2 C} \quad (2-10)$$

where T_0 is the temperature of the heat sink and the factor ξ is of order unity for semiconductor thermometers with $-\alpha \sim 3-8$. Thus the resolution of an ideal

calorimeter is on the order of the thermodynamic energy fluctuations and scales as $T^{\frac{5}{2}}$ assuming the heat capacity scales as T^3 . The factor ξ is independent of τ and G so the conductance of the thermal link may be chosen to optimize the counting rate without any loss in resolution. It is also a weak function of the temperature coefficient of the thermistor α and $\xi \propto 1/\sqrt{\alpha}$ as $\alpha \rightarrow \infty$. Moseley et al. (1984) calculated that a calorimeter with realistic optimized parameters could have $\xi = 2.56$ and $\sqrt{k_B T^2 C} = 0.15$ eV. This yields a theoretical resolution of 0.45 eV rms or 1.1 eV FWHM.

It has since been found that the ultimate attainable energy resolution is worse than this. One problem is the $1/f$ noise common in solid state devices. Another problem is that the above estimate of the energy resolution assumed that the temperature increase due to the absorption of an X-ray photon was small compared with the base temperature. In practice, if the heat capacity of the detector is small enough, this assumption does not hold and the resulting non-linearity degrades the resolution. The resolution is also degraded by metastable energy storage in the absorber which has already been mentioned. Another problem is that the initial phonon spectrum from an absorbed X-ray is non-thermal (Stahle et al. 1993). The thermistors operate by phonon-assisted electron hopping and the resulting sensitivity to very high energy phonons causes position dependence and degrades the resolution. It is likely that the best resolution attainable by resistive calorimeters operating at 0.1 K will be limited to ~ 5 eV because of these effects.

The X-Ray Quantum Calorimeter (XQC Cui et al. 1994) was a sounding rocket payload consisting of an array of microcalorimeters. It successfully observed the diffuse X-ray background in June 1996. A pre-flight spectrum is

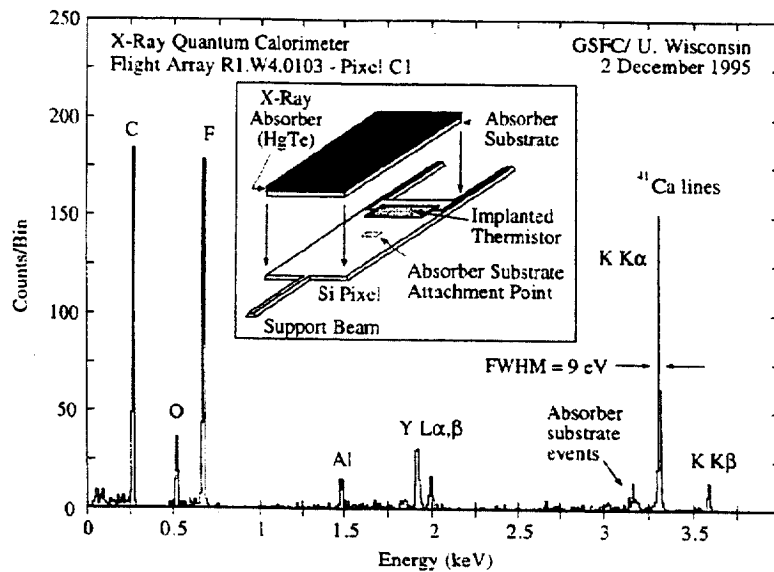


Fig. 2.5— Spectrum obtained from a single pixel of the XQC instrument before launch. The energy resolution is 9 eV.

shown in Figure 2.5.

Superconducting Transition Edge Sensors

Another type of calorimeter is the superconducting transition edge sensor (Irwin 1995; Irwin et al. 1996). The resistive thermometer in this system is a superconducting film which is voltage biased at a point on the superconducting-normal transition. Because α is positive the detector operates with negative electrothermal feedback. The absorption of an X-ray photon results in a drop in current which is measured with a SQUID amplifier. The thermal resistance between the film and substrate will be due to electron-phonon decoupling for thin films at low temperatures or the Kapitza resistance (e.g. Little 1959) for thick films at

higher temperatures. The power flowing to the substrate is

$$P_0 = K(T^n - T_0^n) \quad (2-11)$$

where the thermal conductance is

$$g = nK(T^{n-1} - T_0^{n-1}). \quad (2-12)$$

If electron-phonon decoupling dominates the thermal resistance n will be 5 or 6. If the Kapitza resistance dominates $n = 4$. The effective time constant of a transition edge detector is

$$\tau_{\text{eff}} = \frac{\tau}{1 + \frac{\alpha}{n}}. \quad (2-13)$$

For high-purity films values of $\alpha = 100\text{--}1000$ are feasible. The availability of larger values of α is the only fundamental difference between transition edge detectors and calorimeters with semiconductor thermometers. The much higher values of α allow the transition edge detector to operate in the extreme electrothermal feedback regime where almost all of the energy deposited by an X-ray photon is removed by a decrease in Joule heating. This allows higher counting rates and better energy resolution to be attained, provided an amplifier with a wide bandwidth is used such as the two-stage SQUID amplifiers developed by Welty and Martinis (1993). The fundamental limit on the resolution of transition edge sensors is

$$\Delta E_{\text{FWHM}} = 2.36 \sqrt{4kT^2C \left(\frac{1}{\alpha}\right) \sqrt{\frac{n}{2}}}. \quad (2-14)$$

2.3.2 Thermal X-Ray Detectors with Reactive Thermometers

2.3.3 Kinetic Inductance Thermometry

The idea of kinetic inductance dates from the time of Faraday. Kinetic inductance is essentially the inertial mass of the charge carriers. The energy associated with a current I is

$$E = \frac{1}{2}L_M I^2 + \int_{\text{conductor}} \frac{1}{2} n m_q v^2 d\tau \equiv \frac{1}{2}L_M I^2 + \frac{1}{2}L_k I^2 \quad (2-15)$$

For a uniform current in a homogeneous conductor the kinetic inductance is

$$L_k = \left(\frac{m_q}{n q^2} \right) \left(\frac{l}{\sigma} \right) \quad (2-16)$$

L_k is the *kinetic inductance* of the circuit. L_k depends on the geometry of the conductor through the length l and the cross-sectional area σ of the conductor. It also depends on the material through the number density n of the current carriers, their mass m_q , and their charge q (Meservey and Tedrow 1969).

In most situations L_k is negligible compared to L_M . This is because in a normal metal the time between collisions for the charge carriers τ_c is short so that the kinetic reactance will not be comparable to the ohmic resistance for frequencies less than $\sim 10^{13}$ Hz where $\omega\tau_c \sim 1$. In a superconductor the current is carried without dissipation by Cooper pairs so $\tau_c \rightarrow \infty$. Thus the kinetic reactance dominates the ohmic resistance for all frequencies. The geometric inductance L_M is controlled by the geometry of the circuit. For a long thin superconductor with a ground plane to reduce L_M , L_k may dominate.

The kinetic inductance arises naturally from the first London equation:

$$\mathbf{E} = \frac{\partial}{\partial t} (\Lambda(T) \mathbf{J}_s). \quad (2-17)$$

Substituting into Poynting's theorem and neglecting the normal channel yields (Orlando and Delin 1991)

$$-\oint_{\Sigma} \mathbf{S} \cdot d\mathbf{s} = \frac{d}{dt} \int_V \left(\frac{1}{2} \epsilon \mathbf{E}^2 + \frac{1}{2} \mu_0 \mathbf{H}^2 + \frac{1}{2} \Lambda(T) \mathbf{J}_s^2 \right) dv. \quad (2-18)$$

The third term in the integral may be rewritten

$$\frac{1}{2} \Lambda \mathbf{J}_s^2 = n^*(T) \left(\frac{1}{2} m^* \mathbf{v}_s^2 \right). \quad (2-19)$$

This term represents the kinetic energy of the Cooper pairs whose number density and effective mass are n^* and m^* . So the kinetic inductance depends on the penetration depth

$$\lambda(T) = \sqrt{\frac{\Lambda(T)}{\mu_0}} \quad (2-20)$$

and hence on the temperature.

The inductance of a superconducting stripline is given by (Meyers 1961)

$$L = \mu_0 \frac{l}{w} \left[t + \lambda_s \coth \frac{d_s}{\lambda_s} + \lambda_g \coth \frac{d_g}{\lambda_g} \right] \quad (2-21)$$

where

$$\lambda_{g,s}(T) = \frac{\lambda_{g,s}(0)}{\sqrt{1 - \left(\frac{T}{T_c}\right)^4}} \quad (2-22)$$

is the penetration depth in the superconducting film. The subscripts g and s refer to the ground plane and meander strip, respectively. The length of the meander strip is l , w is its width, t is the thickness of the dielectric layer, and d_g and d_s are the thicknesses of the ground plane and meander strip as shown in Figure 2.6. The critical temperature is T_c and $\lambda(0)$ refers to the penetration depth at absolute zero. This function varies very rapidly with temperature close to T_c . There are two limiting cases which are of interest here. For thick films $d \gg \lambda$ and $L_k \propto \lambda$. For thin films $d \ll \lambda$ and the temperature dependence is stronger:

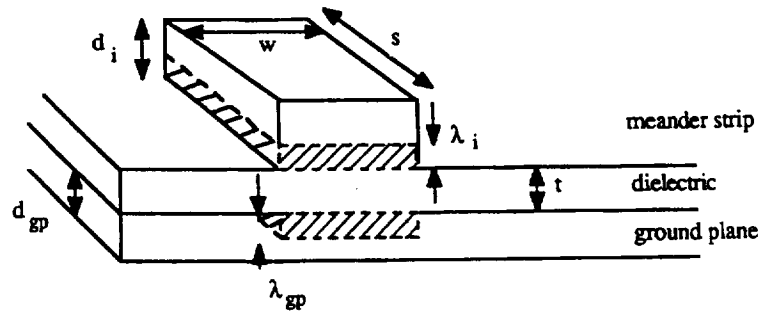


Fig. 2.6— Cross-section of a kinetic inductor. The supercurrents flow approximately in the shaded regions.

$L_k \propto \lambda^2$. Clearly, to maximize sensitivity, a kinetic inductance thermometer should be designed to operate in the latter limit. For a superconductor such as Al ($\lambda(0) \approx 500 \text{ \AA}$) this would require films less than 100 \AA thick.

The elimination of Johnson noise and the use of a SQUID preamplifier could improve the resolution by a factor of ~ 50 over that of a resistive calorimeter with the same total heat capacity.

Chapter 3

X-Ray Observatories

This has been a multi-mission observational project. Each of the X-ray observatories used has its own strengths which allowed me to gain different insights into the nature of Cen X-3. Here I describe the characteristics of these observatories.

3.1 The Broad Band X-Ray Telescope

The Broad Band X-Ray Telescope (BBXRT) was flown as part of the Astro 1 mission on the Space Shuttle Columbia in December 1990 (Serlemitsos et al. 1990). The configuration of BBXRT in the Shuttle's cargo bay is shown in Figure 3.1.

BBXRT consisted of two identical, coaligned telescopes (labeled A and B) with cooled Si(Li) detectors. The telescope mirrors were conical approximations to the Wolter Type I geometry (VanSpeybroeck and Chase 1972). This allowed lightweight X-ray-reflecting foils to be used which could be nested as shown in Figure 3.2 to maximize the effective area at the expense of position resolution. Each BBXRT telescope had 118 coaxially nested mirrors.

The calibration of the instruments is discussed in detail by Weaver et al.

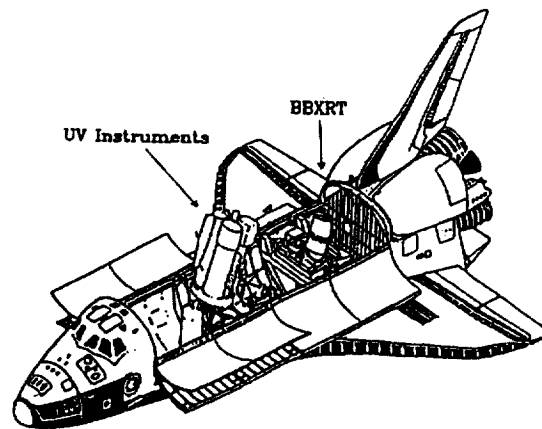


Fig. 3.1— BBXRT in the Space Shuttle's cargo bay. (Weaver 1993).

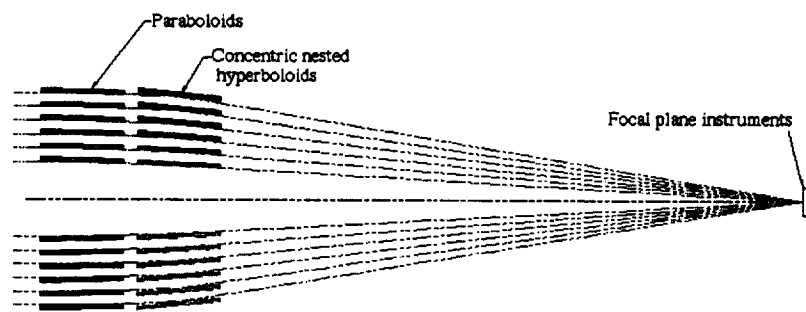


Fig. 3.2— Nested X-ray mirrors.

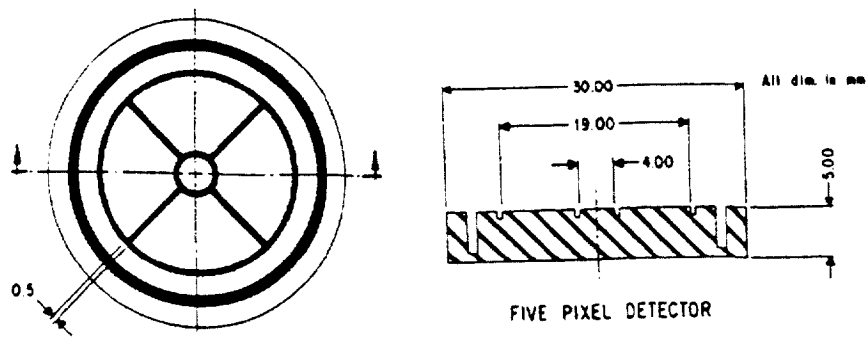


Fig. 3.3— Layout of the BBXRT segmented detectors (Serlemitsos et al. 1984).

(1995). Each segmented detector consisted of a central pixel (denoted A0 or B0), with a field of view 4 arcmin in diameter, surrounded by four outer pixels giving the detector a total field of view 17 arcmin in diameter. The point spread function was such that about 62% of the events from a point source fell on the central pixel for an on-axis pointing. The energy resolution was about 150 eV FWHM at 6 keV in the central pixels.

Photon arrival times were recorded with a resolution of 63 μ s. There were five photon quality flags recorded with each event. These used anticoincidence techniques to reject spurious events which were probably not due to X-ray photons. Events which were detected simultaneously with events in the same or other pixels were labeled with the pulse-pulse and pixel-pixel flags respectively. Events which had a deposited charge greater than about 14 keV were flagged as very large events (VLE). Firings of the opto-feedback circuits caused events to be labeled with the LED flag. The final anticoincidence flag was against triggering of the charged particle guard detector.

3.2 The European X-Ray Observatory Satellite

The high, elliptical orbit of the European X-Ray Observatory Satellite (EXOSAT) allowed uninterrupted pointings lasting for days.

3.2.1 The Gas Scintillation Proportional Counter

EXOSAT's Gas Scintillation Proportional Counter (GSPC) is shown in Figure 3.2.1. It had a FWHM energy resolution of 10% at 6 keV. The energy resolution was proportional to $E^{-1/2}$. The detector's beryllium window formed a section of a sphere. In front of this was a mechanical collimator that provided a 45' FWHM field of view. The gas cell was filled with 95% xenon and 5% helium at a pressure of 1 atmosphere.

3.3 The Advanced Satellite for Cosmology and Astrophysics

The Advanced Satellite for Cosmology and Astrophysics (ASCA) is the fourth Japanese X-ray astronomy satellite.

3.3.1 The X-Ray Telescope

The X-Ray Telescope (XRT) consists of four identical X-ray telescopes with focal length 3.5 m. The telescopes are mounted on an extendable optical bench which was expanded after launch to place the focal plane at the detectors. Each telescope is made up of 120 concentric aluminum foils 125 μm thick which are nested about 1 mm apart. Like those in the BBXRT mirrors, the foils are ar-

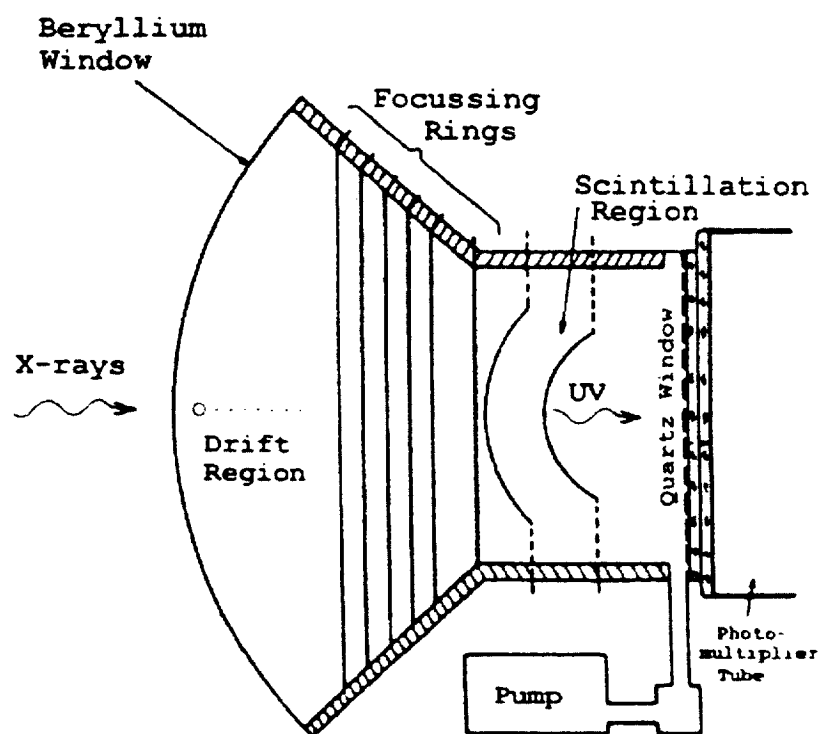


Fig. 3.4— The EXOSAT GSPC (Peacock et al. 1981).

ranged in a conical approximation to the Wolter geometry. X-Rays are reflected at grazing angles of $0.5''$ by a 60 nm layer of gold. The pass band is 0.5–12 keV and the spatial resolution is $2.9''$ (half-power diameter). The telescope's plate scale is such that this corresponds to 2.9 mm at the focal plane.

3.3.2 The Solid State Imaging Spectrometers

There are two Solid State Imaging Spectrometers (SIS). Each SIS has four front-illuminated CCD chips. The chips are mounted side by side to form a square. Each chip consists of a 420×422 array of pixels. The field of view of each SIS camera is $22 \times 22'$. The energy resolution is 2% FWHM at 5.9 keV.

In normal operation the SIS is operated in one-CCD mode. Observations using all four CCDs of each SIS were only carried out during the performance verification phase of the mission. The mode in which the SIS is read out determines the spatial and timing resolution. In bright mode the CCD is read out once every four seconds, with full spatial information. Unfortunately, Cen X-3 is sub-Nyquist for this sampling frequency so bright mode data is not useful for pulse-phase resolved spectroscopy. In fast mode the CCD is read out every 16 ms. This timing resolution is achieved by sacrificing spatial information. The spatial information in fast mode is reduced to one bit. This bit tells us whether an X-ray event occurred inside or outside a rectangular region of the chip. The source is usually contained within this region which is set by the telescope operator after the first pass over a ground station. Its purpose is to allow observations of bright sources that might saturate the telemetry. If the count rate is too high, only events occurring outside the discrimination region will be transmitted to the ground station. One problem with fast mode is that it does not allow the

removal of hot and flickering pixels. Problems caused by these effects should be less than in bright mode, however, because of the shorter integration time.

The XRT's response to incident X-rays depends on the off-axis and azimuthal angles of the source. The only way to determine these for fast mode is by also carrying out bright mode observations of the source. A map of the SIS CCD is made with each point weighted by the number of X-ray counts. This weighted map is used to generate an auxilliary response file (ARF). This ARF file takes into account the XRT response. The energy response of the CCD detectors is contained in a redistribution matrix file (RMF). In generating the RMF, changes in the gain of the detectors are taken into account. These changes occur because of degradation by charged particles. For SIS data taken in bright mode, these gain changes can be applied directly to the pulse-height-analyser (PHA) data to create pulse invariant (PI) data. PI spectral data will all have the same energy-channel relationship and can thus be added.

3.3.3 The Gas Imaging Spectrometers

There are two Gas Imaging Spectrometers (GIS: Ohashi et al. 1991). Their layout is shown in Figure 3.5. There is a ground mesh just above the quartz window. The beryllium entrance window is held at a potential of -7 kV relative to this. The cloud of photoelectrons created by an incident X-ray drifts to the accelerating grid which is at a potential of -6 kV. The cloud is then accelerated by the strong field in the emission region, collisionally exciting xenon atoms. These emit ultraviolet scintillation photons which are detected with a position-sensitive phototube. The GIS energy resolution is $7.8\% \sqrt{5.9 \text{ keV}/E}$. Its spatial resolution is 0.5 mm which is better than that of the XRT. The charged-particle

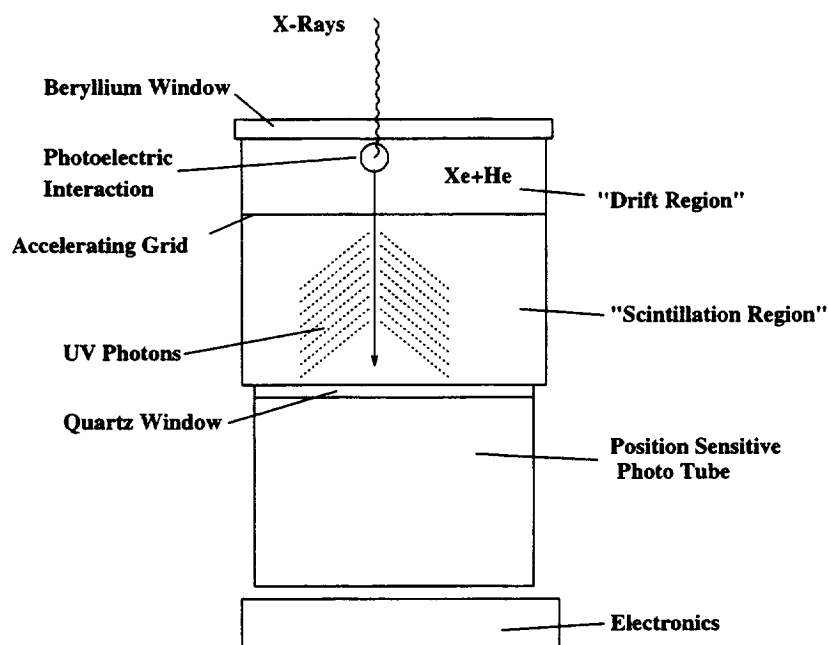


Fig. 3.5— Layout of the ASCA GIS (Gendreau 1995).

background is rejected by pulse rise-time discrimination.

3.4 The Rossi X-Ray Timing Explorer

The Rossi X-Ray Timing Explorer was launched in December 1996. It carries three telescopes. The All Sky Monitor (ASM) provides continuous monitoring of the X-ray sky in the 2–10 keV band. The observatory has been designed to slew quickly and bring its other two telescopes to bear on targets of opportunity. The ASM also continuously monitors the intensities of bright sources and can be used to ensure that an observation takes place when the target is in the appropriate

intensity state.

3.4.1 The Proportional Counter Array

The Proportional Counter Array (PCA) consists of five coaligned proportional counter units (PCUs). Each PCU has three detector layers which contain xenon. Background rejection is effected with side and back guard chambers containing xenon and a front cell containing propane. The PCA has a nominal bandpass of 2–60 keV and an energy resolution of 18% at 6 keV.

3.4.2 The High Energy X-Ray Timing Experiment

The High Energy X-Ray Timing Experiment (HEXTE) consists of two clusters of phoswich scintillation detectors (see Section 2.2.1). Background subtraction is done by rocking on and off the source. The two clusters are pivoted so that they rock perpendicular to each other. The detectors dwell on the source for 16 s. It takes 2 s to move to the background field and 2 s to move back. Thus the background dwell time is 12 s. The background pointing offset can be set to $\pm 3^\circ$ or $\pm 1.5^\circ$. HEXTE's energy resolution is about 17% at 60 keV (Rothschild et al. 1998). Both HEXTE and the PCA have a circular field of view with a FWHM of 1° .

3.5 Summary

The various X-ray observatories used in this work have different characteristics which make them useful for investigating different properties of Cen X-3. BBXRT was useful for iron line spectroscopy as it covered the iron line region

with high spectral resolution and an extremely low background. Although it covered the iron line region with worse spectral resolution than BBXRT, the EXOSAT GSPC had a better high energy response which allowed the shape of the continuum spectrum to be investigated. The ASCA SIS has slightly better spectral resolution than BBXRT, allowing the iron line to be further resolved. The spectral resolution of the ASCA GIS is only slightly better than that of the EXOSAT GSPC but the imaging capabilities allow more reliable subtraction of the X-ray background. The RXTE PCA covers the energy range from 15 to 60 keV. HEXTE covers the range from 15 to 200 keV. The background subtraction in HEXTE is better than that in the PCA but it has poorer energy resolution. In Figure 3.6 I show the energy responses of these instruments. These are **total** effective area curves appropriate for the data analysed in this work. They were derived from the ARF and RMF files that were generated for the Cen X-3 data. Because of vignetting the effective areas shown here will generally be smaller than the advertised values. In Table 3.5 I list the X-ray observatories used in this dissertation along with the main results.

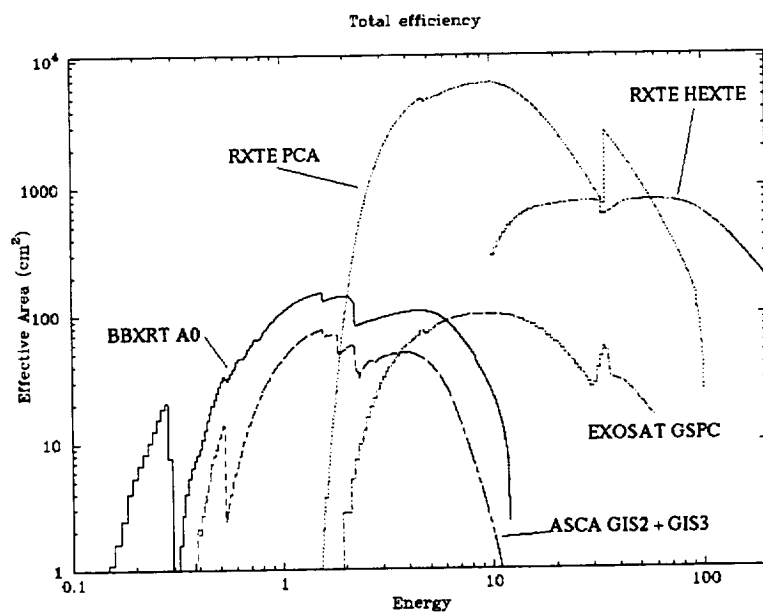


Fig. 3.6— Comparison of the effective areas of the X-ray telescopes used in this work. The SIS effective area is not much different from that of the GIS and has been omitted for clarity.

Table 3.1. X-ray observatories and results used in this dissertation.

Mission	Mission Dates	Results
EXOSAT	1983 May 26–1986 April 9	Continuum Spectrum — consistent with cyclotron opacity
BBXRT	1990 December 2–11	Partially resolved iron lines, predicted CSRF from QPO
ASCA	1993 February 20–	Resolved iron lines, 6.4 keV line pulsed
RXTE	1995 December 30–	Detected CSRF

Chapter 4

Centaurus X-3

4.1 Orbital Properties

Centaurus X-3 was discovered in May 1967 during a survey of the southern sky with a sounding rocket carrying proportional counters (Chodil et al. 1967). Observations with Uhuru later showed that the X-ray flux was modulated by regular pulsations (Giacconi et al. 1971) with a 4.8 s period. On the basis of Doppler variations in its pulse period observed with Uhuru, Cen X-3 was the first of the X-ray sources to be established as a binary (Schreier et al. 1972). The X-ray eclipses which occur every 2.1 days suggest a high inclination angle i . Assuming an eclipse half angle of 40° , Conti (1978) estimated the radius of the companion R_c to be $12.5 R_\odot$ and $i > 80^\circ$. Clark et al. (1988) estimated the eclipse half angle as 32.9° and derived a mass of $(1.23 \pm 0.60)M_\odot$ for the neutron star. After reviewing the available data van Kerkwijk et al. (1995) derived the 95% confidence values $M_x = 1.09^{+0.57}_{-0.52}M_\odot$, $M_c = 18.9^{+4.0}_{-1.8}M_\odot$, $R_c = 11.1^{+1.8}_{-1.1}R_\odot$, and $i > 66^\circ$. The companion is a highly reddened O-type star known as V779 Cen or Krzemiński's star. From the optical reddening a distance of ~ 8 kpc has been inferred, with a lower limit of 6.2 kpc (Krzemiński 1974). Because Cen X-3 has

not been detected in radio there is no dispersion measure to compare with this and the distance is uncertain. Day and Tennant (1991) used the EXOSAT ME to observe soft emission during two eclipses. They interpreted this as a dust-scattered halo and calculated the distance to the source as 5.4 ± 0.3 kpc. The absolute distance to the source does not affect any of the results of this work except the calculated luminosities. For convenience the distance to Cen X-3 will be taken to be 8 kpc.

The binary parameters of Cen X-3 have been well determined (Nagase et al. 1992; Joss and Rappaport 1984, and references therein). The pulsar is spinning up with $\dot{P}/P \approx 2.3 \times 10^{-4} \text{ yr}^{-1}$ (Nagase et al. 1992). This is due to the accretion of matter with a high specific angular momentum (Ghosh et al. 1977; Ghosh and Lamb 1979a,b). The orbital period is decreasing with $\dot{P}_{\text{orb}}/P_{\text{orb}} \approx -1.74 \times 10^6 \text{ yr}^{-1}$ (Nagase et al. 1992) due to unstable tidal dissipation (Kelley et al. 1983).

4.2 Mass Transfer

The spectral classification of the companion star (O6–8f), the presence of residual emission at mid-eclipse, and the broad eclipse transitions indicate that there is a strong stellar wind. This wind reprocesses the emission from the compact source and would be expected to have a significant effect on the X-ray spectrum. The observed high state luminosity $\sim 10^{38} \text{ erg s}^{-1}$ (van der Klis et al. 1980) is too large to be accounted for by spherical wind accretion alone (Petterson 1978). Thus, at least in the high state, most of the mass transfer must take place by another mechanism such as tidal enhancement of the wind or Roche

lobe overflow.

Because of the high X-ray luminosity of the source it is expected that there is a region of extreme ionization surrounding the neutron star and extending to a distance greater than the radius of the companion (Hatchett and McCray 1977; Blondin 1994b). This would rule out the presence of a normal line-driven wind from the region of the companion facing the neutron star. This is because highly stripped ions are transparent to the ultraviolet radiation that drives such a wind. Day and Stevens (1993) have suggested that when the source is in the high luminosity state the accretion is instead driven by a wind which is thermally excited by the intense X-ray flux. However a line-driven wind may still be driven from the part of the companion not illuminated by the X-ray source. This shadow wind will quickly become ionized when it is exposed to the X-ray source and it will cease to be radially accelerated by radiation from the companion (Blondin 1994a). This stalled wind may be responsible for episodes of absorption detected around orbital phase 0.6 (Pounds et al. 1975)

4.3 Formation of an Accretion Disk.

Bonnet-Bidaud and van der Klis (1979) showed that even if the accretion is from the stellar wind, the mass accretion rate will be large enough to require an accretion disk to remove angular momentum from infalling material. Tjemkes et al. (1986) used a simple geometric model to analyze the optical light curve and found that ellipsoidal variations alone were unable to account for the observed amplitude. They obtained a satisfactory description of the light curves by including the effects of X-ray heating of the companion and optical emission

from a Roche lobe filling accretion disk ($R_{\text{disk}} \approx 2.4 \times 10^{11}$ cm). The average V band light curve is shown in Figure 4.1. Khruzina and Cherepaschuk (1986) similarly found that an accretion disk with $R_{\text{disk}} = 2.44 \pm 0.84 \times 10^{11}$ cm was required and that the companion almost filled its Roche lobe, having a filling factor $\mu = 0.995 \pm 0.005$. Equation 1-8 gives

$$R_{\text{circ}} \approx 5.8 \times 10^{10} \text{ cm} \quad (4-1)$$

while the distance from the neutron star to the L_1 point is

$$b \approx 2.8 \times 10^{11} \text{ cm} \quad (4-2)$$

which is larger than R_{circ} as expected. This is because the material in the disk will spread towards both larger and smaller radii than R_{circ} as the angular momentum shed by the accreting matter is transported to the outer parts of the disk.

The existence of an accretion disk is also implied by the presence of 40 mHz quasi-periodic oscillations (QPO). These were discovered by Tennant (1988) in EXOSAT ME data. They were also present in Ginga data (Takeshima et al. 1991). These are believed to be due to the interaction between the accretion disk and the magnetosphere.

4.4 The X-Ray Light Curve

The average X-ray luminosity has been known to vary by a factor of ~ 8 on a timescale of months between the source's high and low states. Friedhorsky and Terrel (1983) found that this behavior had a characteristic timescale of 120–165 days but found no evidence for periodicity. More recent results from the

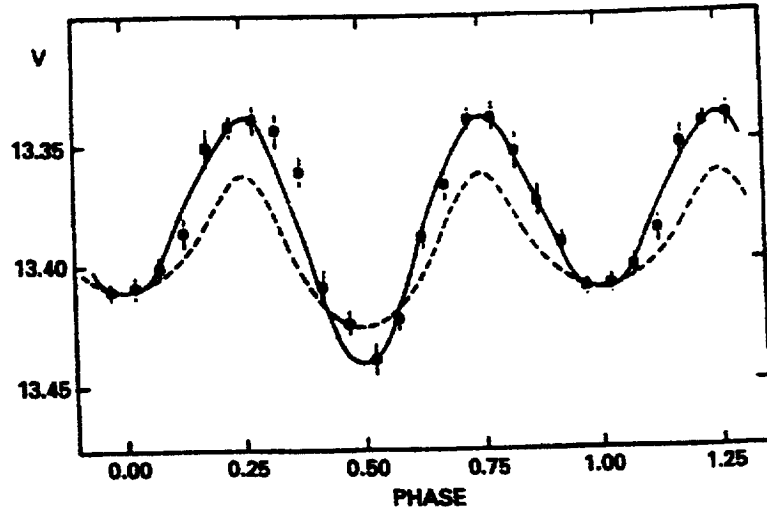


Fig. 4.1— Average V band light curve of Cen X-3 (Tjemkes et al. 1986). The solid curve includes the effects of X-ray heating and an accretion disk while the dashed curve only includes ellipsoidal variations.

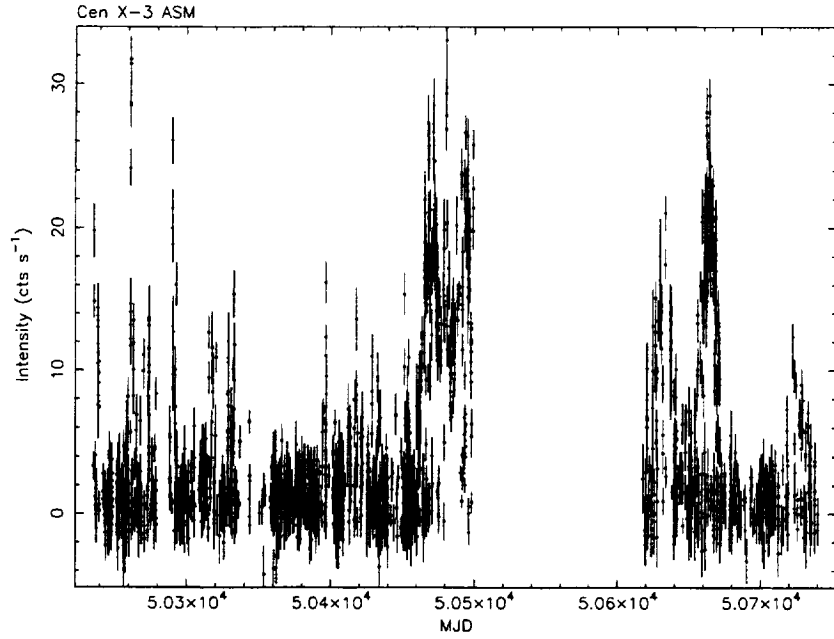


Fig. 4.2— Long-term X-ray light curve of Cen X-3 obtained with the RXTE ASM.

RXTE All Sky Monitor (ASM) show that Cen X-3's X-ray emission is more variable than this on a timescale of days. Figure 4.2 shows the long-term X-ray light curve of Cen X-3 obtained with the ASM. These are quick-look results provided by the ASM/RXTE team. Gaps in the light curve are due to the source being too faint to detect. New results on the variability of Cen X-3's luminosity will be presented in Chapter 8.

The pulse shape is also variable, changing from an asymmetric single peak in the high state to a rarely observed double peaked structure in the low state (e.g. Long et al. 1975; Tuohy 1976; Nagase et al. 1992). Relatively short term variability in the pulse profile has also been observed (e.g. Schreier et al. 1976;

van der Klis et al. 1980). Examples of this short-term variability will be shown in later chapters where I propose that they are due to luminosity-induced changes in the structure of the accretion column.

Day and Stevens (1993) have suggested that the source's high and low states are the result of positive feedback between the X-ray emission and an X-ray excited wind. The X-ray emission of the neutron star excites the wind which increases the mass accretion rate and thus the X-ray luminosity until the source becomes buried in an optically thick wind and possibly behind a flared accretion disk and switches off. A prediction of this model is that the column density and iron line equivalent width should be much higher in the low state than in the high state.

4.5 The X-Ray Spectrum

Figure 4.3 shows a typical X-ray spectrum of Cen X-3 observed with the EXOSAT GSPC (see Chapter 6). The data have been unfolded from the instrument response. The pulse-phase averaged spectrum between 1 and 20 keV is fitted by a power law with photon index ~ 1 , modified by interstellar absorption and an exponential roll off to higher energies. There is also an iron emission feature between 6 and 7 keV (White et al. 1983, and references therein) which has been found to pulsate with an amplitude $\sim 50\%$ of the mean intensity (Takalo et al. 1990; Day et al. 1993). The energy of this feature varies with pulse phase and from observation to observation. Nagase et al. (1992) modeled the iron line as a blend of 6.4 keV and 6.7 keV lines. They found that the 6.4 keV line underwent

an abrupt eclipse, implying that the size of its emission region was

$$D_{6.4} \lesssim 3 \times 10^{10} \text{ cm} \approx 1 \text{ light-second.} \quad (4-3)$$

The 6.7 keV line had a much broader partial eclipse which means that

$$D_{6.7} \gtrsim 8 \times 10^{11} \text{ cm} \approx 27 \text{ light-second.} \quad (4-4)$$

Comparing these values with Figure 1.3 it is clear that $D_{6.7}$ is comparable to the radius of the companion. The constraint on $D_{6.4}$ is satisfied comfortably by the Alfvén radius ($R_A \sim 3 \times 10^8 \text{ cm}$ from Equation 1-54). Day et al. (1993) consider back illumination of an incomplete Alfvén shell by one pole of the neutron star to be the most likely source of the pulsed 6.4 keV line.

In order to explain the observed properties of the iron lines in Cen X-3 we must be able to specify where the radiation is emitted, how is it reprocessed and what the physical conditions in those places are. Because of the intense X-ray flux one might expect that all the matter close to the neutron star should be completely ionized. However the results of Nagase et al. (1992) show relatively un-ionized iron emission within 1 light-second of the neutron star. This is possible because the accretion disk is not fully ionized. It is dense enough for recombination to keep the ionization parameter $\xi = \frac{L_x}{n_e r^2}$ low. The time required for local thermodynamic equilibrium (LTE) to be attained is proportional to the inverse of the electron density n_e . For a 10^4 K plasma with $n_e \sim 10^{16} \text{ cm}^{-3}$ LTE is established in less than $1 \mu\text{s}$ (Thorne 1988). This suggests that matter entering the accretion disk will quickly recombine. I have calculated the radial dependence of the properties of an accretion disk based on the model of Shakura and Sunyaev (1973). The results are shown in Figure 4.4. The luminosity has been assumed to be $10^{37} \text{ erg s}^{-1}$. The radial dependence of ξ is calculated for

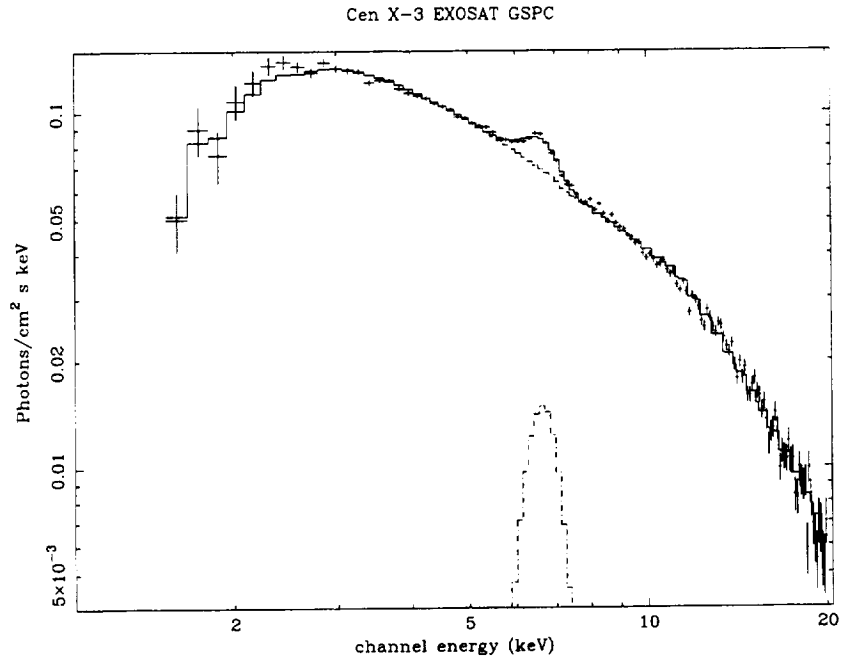


Fig. 4.3— Typical pulse-phase averaged X-ray spectrum of Cen X-3 observed with the EXOSAT GSPC. The data have been unfolded from the instrument response. The spectrum is a power law with photon index ~ 1 which falls off to low energies due to interstellar absorption and has an exponential roll off above 10 keV. The prominent feature between 6 and 7 keV is due to Fe K_{α} emission.

normal incidence of the X-ray flux on the disk and thus describes an upper limit to ξ . From Equation 1-54 the inner disk is truncated at $r = r_A \approx 3 \times 10^8$ cm and the disk parameters have been calculated for radii greater than this. This means that the disk can contribute a fraction $R_x/r_A \sim 10^{-2}$ of the total luminosity. Thus the only observable X-rays from the disk will be reflected. The low calculated value of the ionization parameter ξ suggests that photoionization will not be important for iron in the disk. This model does not include the effects of X-ray heating by radiation from the neutron star. The radiation temperature will be

$$T_{\text{rad}} = 1.1 \times 10^5 L_{37}^{\frac{1}{2}} R_{10}^{-\frac{1}{2}} \text{ K} \quad (4-5)$$

assuming a face-on disk.

Figure 4.4 shows that the inner accretion disk is a plausible emission site for the 6.4 keV fluorescent iron line. If this is the case the physical width of the line may place an upper limit on the temperature of the fluorescing matter and the Keplerian rotation speed of the magnetosphere.

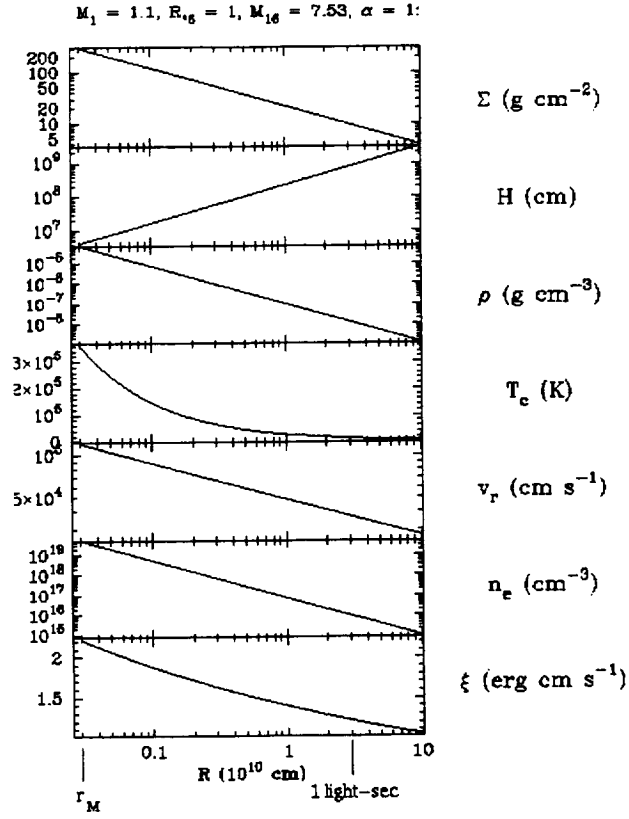


Fig. 4.4— Radial dependence of the properties of an accretion disk based on the model of Shakura and Sunyaev (1973) with $\alpha = 1$. This calculation assumes $M_1 = M_x/M_\odot = 1.1$, $R_6 = 1$, and $L_{37} = 1$. The parameters shown, from top to bottom, are the disk mass per unit area Σ , the disk scale height H , the disk density ρ , the central temperature T_c (in the midplane of the disk), the radial drift speed v_r , the electron density n_e , and the ionization parameter ξ .

Chapter 5

Resolving the Iron Line — BBXRT

5.1 The Observation

Cen X-3 was observed on December 9, 1990 from 13:10:12 to 13:38:20 UT yielding about 1600 s of usable data. At the time of the observation, the pulsar was at orbital phase $\sim +0.27$, measured from mid-X-ray eclipse. Because this was a daytime shuttle observation the star cameras were switched off and an aspect solution was not available. However, the position of the source relative to the center of the A0 pixel was deduced by comparing the ratios of counting rates in the central and outer pixels with those predicted by a ray tracing model. It was found that the source was 1.4 arcmin off axis in A0 and 2.2 arcmin off axis in B0. Thus, in the B telescope, much of the flux fell on the mask separating the pixels.

5.1.1 Background rejection

During the observation the Space Shuttle passed through the South Atlantic Anomaly (SAA). The SAA is an area of low geomagnetic rigidity over the At-

lantic ocean off the east coast of Brazil. It is due to the misalignment between the earth's magnetic and rotational axes. Because the earth's magnetic field is lower than the average in this region charged particles trapped in the inner radiation belt can penetrate down to an altitude of 250 km. X-Ray detectors are usually switched off or placed in a safe mode during SAA passages because of the high charged-particle background.

The anticoincidence features of BBXRT worked well, allowing useful data to be obtained during the SAA transit. Contaminating events were removed by rejecting those for which any of the quality flags were set and the analysis was restricted to energies above 1 keV. The latter also removed geocoronal contamination but caused no loss of information as the source is heavily absorbed below 1 keV. This is the first time a celestial X-ray source has been successfully observed through an SAA passage.

Contamination from the galactic ridge is a concern for sources which are near the galactic equator. Assuming a background flux of $8 \times 10^{-8} \text{ erg cm}^{-2} \text{ s}^{-1} \text{ sr}^{-1}$ in the 2–11 keV band (Koyama et al. 1986), the flux detected by the A0 pixel should be $\sim 3 \times 10^{-14} \text{ erg cm}^{-2} \text{ s}^{-1}$. This is much smaller than the continuum and iron line fluxes detected by BBXRT (4×10^{-9} and $8 \times 10^{-11} \text{ erg cm}^{-2} \text{ s}^{-1}$, respectively) so emission from the galactic ridge can safely be neglected.

5.2 Results

5.2.1 Timing analysis

The apparent pulse period was obtained by epoch folding and found to be $4.81250 \pm 0.00074 \text{ s}$. Barycentric corrections were applied to this period and it

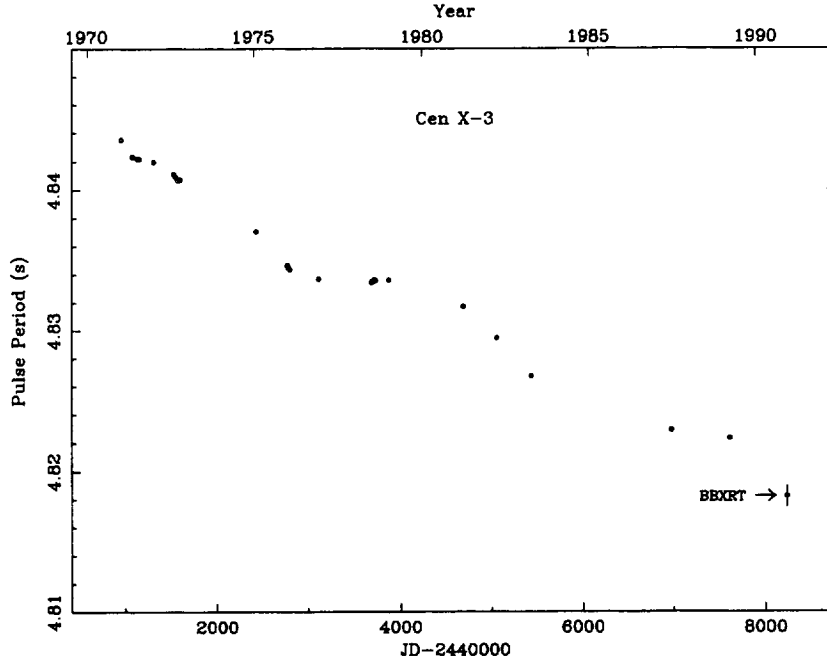


Fig. 5.1— The long-term behavior of the pulse period of Cen X-3. The overall trend is a secular spin up at an average rate of $\dot{P}/P = -2.26 \times 10^{-4} \text{ yr}^{-1}$.

was then corrected for the orbital motion of the neutron star using the ephemeris of Nagase et al. (1992). The inertial pulse period is $4.81823 \pm 0.00074 \text{ s}$. When this is combined with previous measurements (Nagase et al. 1992, and references therein) the average rate of change of the pulse period from a weighted fit is $\dot{P}/P = -2.26 \times 10^{-4} \text{ yr}^{-1}$. The long-term behavior of the pulse period is shown in Figure 5.1. The spin up rate exhibits short term fluctuations which have been attributed to variations in the accretion rate (van der Klis et al. 1980).

The average pulse profile in the energy range 1–12 keV obtained from BBXRT is shown in Figure 5.2. The dependence of the pulse shape on energy was investigated by binning the event data into 1 keV energy bins and folding it with the

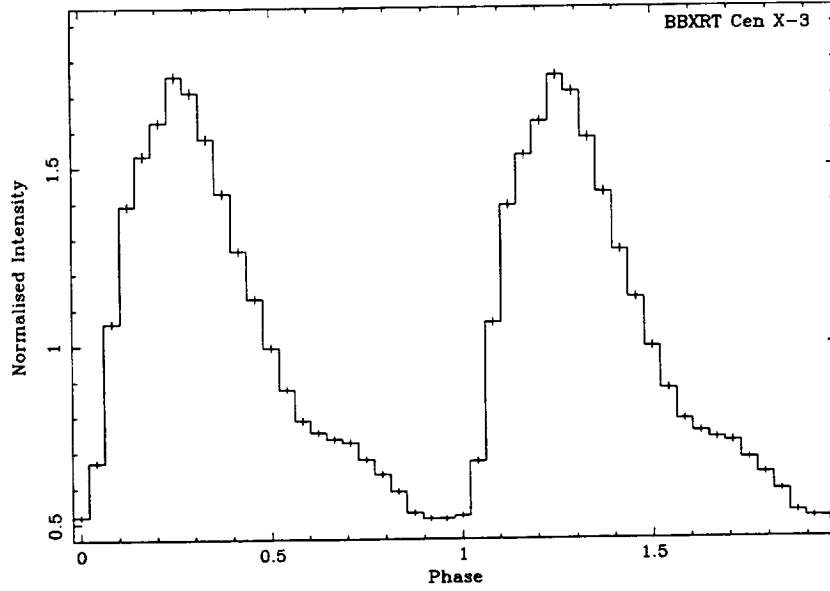


Fig. 5.2— The average pulse profile in the energy range 1–12 keV. The profile is single peaked with a small interpulse which is slightly less prominent at low energies.

pulse period. The profile was found to become slightly less double-peaked at low energies. Figure 5.3 shows the folded light curves over different energy bands.

As shown in Figure 5.4, the previously observed QPO (Takeshima et al. 1991) is evident in the BBXRT data. The QPO peak is well fit by a Lorentzian with centroid 40.7 ± 1.1 mHz and FWHM 4.6 ± 3.4 mHz. The values obtained by Takeshima et al. for the centroid and FWHM were 35 ± 2 and 10 ± 5 mHz, respectively. To test for variations in the QPO power with energy the data were binned into 1 keV energy bins between 1 and 7 keV. Data between 7 and 12 keV were included in a single 5 keV energy bin to improve the counting statistics. The power spectra were obtained and fit to a Lorentzian centered at $\nu = 0$, a power law, a Lorentzian for the QPO, and three narrow Lorentzians for the

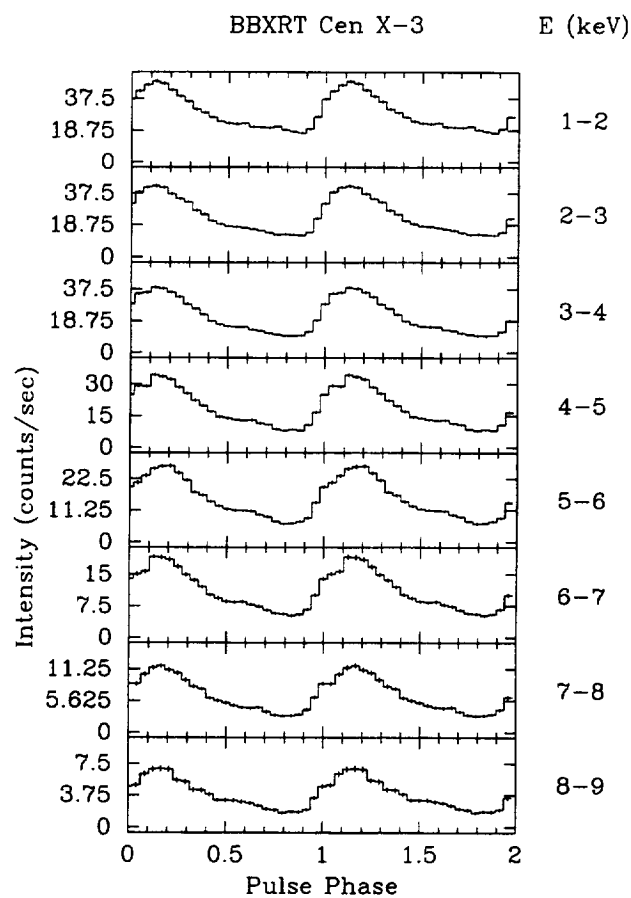


Fig. 5.3— Energy resolved pulse profiles. The A0 data were binned into 1 keV energy bins and folded with the pulse period.

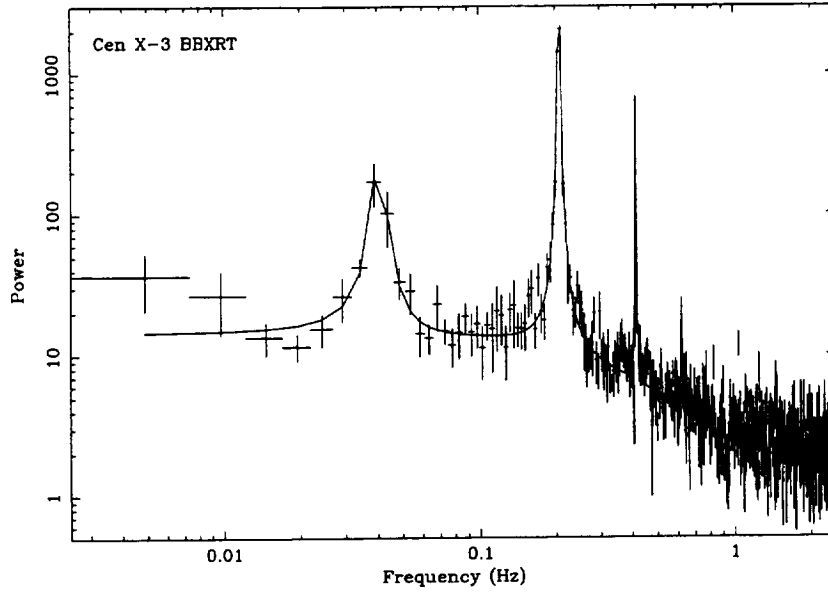


Fig. 5.4— Average power spectrum of Cen X-3 in the energy range 1–12 keV. The A0 data have been fit with a Lorentzian centered at $\nu = 0$, a power law, and four Lorentzians for the QPO, fundamental, and harmonics, in increasing order of frequency.

fundamental and first and second harmonics of the 4.8 s pulse period. The integrated power in the QPO was divided by the total integrated power (up to the Nyquist frequency) to obtain the relative intensity of the QPO. It was found that the relative intensity was well fit by a constant in energy, with $\chi^2 = 6.3$ for six degrees of freedom. The value thus obtained for the relative intensity of the QPO was 7.8 ± 1.2 %.

5.2.2 Spectroscopy of the pulse-phase averaged data

The source was nearly centered in the A0 pixel. However, because of the 0.8 arcminute offset between the two telescopes the source fell further off axis

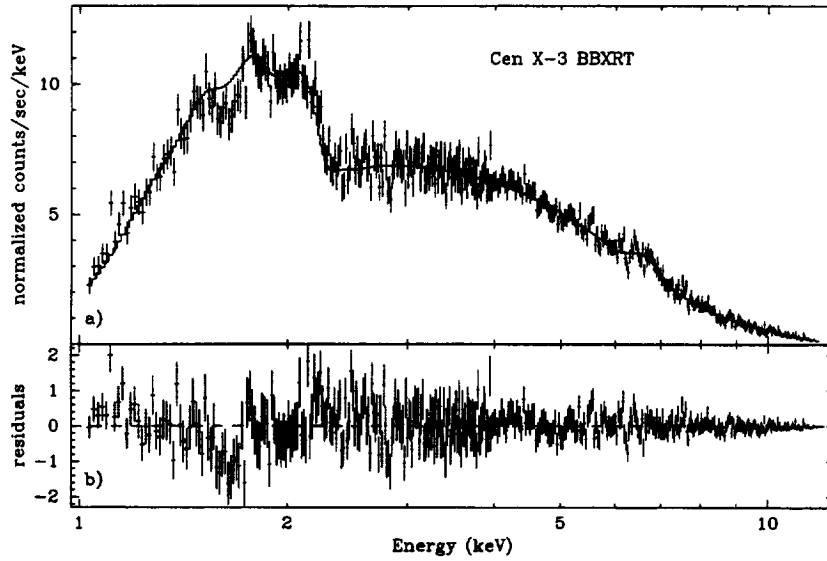


Fig. 5.5— (a) The phase average spectrum of Cen X-3 folded through the telescope response. The A0 data have been fit with an absorbed power law and a Gaussian emission feature at 6.7 keV. (b) The residuals to the fit. Features between 1 and 3 keV are due to instrumental effects. The excesses around 6.4 keV and 7.5 keV may be due to the presence of Fe K_{α} and Ni K_{α} .

in the B0 pixel. Thus B0 detected only half as many events as A0, yielding poorer counting statistics. Because systematic calibration uncertainties can affect results from a high quality spectrum more than those from a low quality one, the A0 and B0 data were treated separately. Thus, in the preliminary analysis fits were performed to the A0 data only. The pulse-phase averaged spectrum detected with the A0 pixel is shown in Figure 5.5.

The spectra of most X-ray binaries may be described by a power law with an exponential roll off above some cutoff energy E_c (e.g. White et al. 1983). The cutoff energy is generally in the range 10-20 keV (Nagase et al. 1992). The present data do not require such a roll off. This indicates that E_c is greater than

the upper limit of BBXRT's energy range (12 keV), in agreement with previous observations (Nagase et al. 1992). The best fit model is an absorbed power law continuum, typical of high mass X-ray binaries, and emission at 6.67 ± 0.07 keV (modeled using a Gaussian). The centroid of the emission line corresponds to transitions of helium-like iron. The photon index is 1.10 ± 0.02 , the absorption column $N_H = (1.28 \pm 0.04) \times 10^{22} \text{ cm}^{-2}$, and the iron emission line has equivalent width 198 ± 45 eV and FWHM 740 ± 210 eV. Fits to the A0 data are summarized in Table 5.1.

If the continuum is modeled by a simple absorbed power law there are residuals of about 10% between 1 and 3 keV. They lie close in energy to the silicon K and gold M_{IV} and M_V edges, respectively. Similar residuals are present, but are less significant, in the B0 data because of the poorer counting statistics. It was found that these could be removed from the A0 data by including two more components in the model: Gaussian absorption at 1.5 ± 0.1 keV and gaussian emission at 2.24 ± 0.04 keV. These have equivalent widths of 69 ± 43 and 16 ± 9 eV respectively. Taken together, these features are significant at the 84% confidence level. When they are included in the model the value obtained for the column density, N_H , is slightly lower, changing from 1.28 to $1.17 \times 10^{22} \text{ cm}^{-2}$. A similar correction to the BBXRT response was necessary for another bright source, Cyg X-2 (Smale et al. 1993). Fits to spectra of the Crab obtained with BBXRT have residuals around 1.7 and 2.2 keV due to uncertainties in modeling the Au and Si edges (Weaver et al. 1995). Owens et al. (1997) have shown that these features in the Crab spectrum are due to X-ray absorption fine structure and are a consequence of the high spectral resolution of BBXRT combined with the brightness of the source. These features in the A0 data were thus inter-

preted as instrumental effects. It must be emphasized that these residuals only appear in data from bright sources such as the Crab. In the majority of BBXRT observations the counting rates were much lower and these residuals were not detectable. In their analysis of the spectrum of Cyg X-1, Marshall et al. (1993) dealt with these instrumental features by ignoring a narrow band of channels around 1.7 and 2.2 keV. It was decided that the same approach would be appropriate for the Cen X-3 data. Ignoring these channels lowered χ^2 significantly and did not appreciably change the continuum parameters. This enabled us to obtain acceptable fits to the A0 data.

Analysis of the B0 data yielded similar results. The iron K emission line energy obtained from the B0 data is slightly lower than that obtained with the A0 data as shown in Table 5.1. However, the model which was fit to A0 gives an acceptable χ^2 when it is fit to the B0 data and only the overall normalization is allowed to vary. The residuals around the silicon and gold edges are not as large as in the A0 data and it is not necessary to remove them to obtain a satisfactory fit. A simultaneous fit to the A0 and B0 data yields an emission line whose FWHM is 0.78 ± 0.18 keV with a centroid energy of 6.63 ± 0.06 keV and equivalent width 200 ± 40 eV.

The presence of residuals around 6.4 keV led us to include a second emission line in the model fit to the A0 data. The best-fit centroid energy for this line is 6.40 ± 0.03 keV. This would correspond to fluorescence of iron in low ionization stages. Its equivalent width is 42 ± 18 eV. The best fit value for its physical width is zero with a 90% confidence upper limit for one interesting parameter of 120 eV FWHM which is less than the FWHM energy resolution. Inclusion of this line in the fit pushes the energy of the broad line to 6.77 ± 0.05 keV

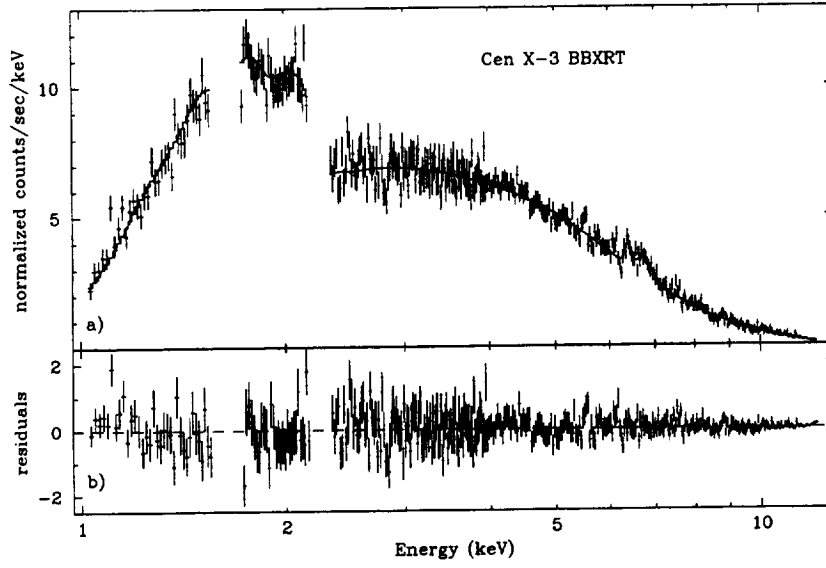


Fig. 5.6— (a) Folded A0 data fit with narrow and broad iron lines at 6.4 and 6.7 keV. (b) Residuals to the fit.

and changes its physical and equivalent widths to 420 ± 180 eV FWHM and 128 ± 37 eV respectively. The fit is shown in Figure 5.6. A two line simultaneous fit to the A0 and B0 data yields similar results as shown in Table 5.1. Although the 6.4 keV line is certainly physically plausible, it is only significant at the 97.2% or 2.2σ level in the A0 data. A second line is not required to obtain a satisfactory fit to the B0 data. This is consistent with the 50% lower counting rate in the B0 pixel as compared with the A0 pixel. When this model is fit to the B0 data the two lines become degenerate.

Table 5.1. Spectral parameters of fits to phase average data.

Detector	A0	B0	A0 and B0
Model 1: Absorbed power law			
N_H (10^{22} cm $^{-2}$)	1.28 ± 0.04	1.26 ± 0.06	1.27 ± 0.03
α	1.10 ± 0.02	1.06 ± 0.03	1.09 ± 0.02
χ^2_ν/ν	1.326/393	1.151/384	1.241/778
Model 2: Absorbed Power Law with one emission line			
N_H (10^{22} cm $^{-2}$)	1.13 ± 0.04	1.29 ± 0.06	1.30 ± 0.03
α	1.14 ± 0.03	1.10 ± 0.04	1.13 ± 0.02
E (keV)	6.67 ± 0.07	6.5 ± 0.1	6.63 ± 0.06
σ (keV)	0.32 ± 0.09	0.4 ± 0.2	0.34 ± 0.08
EW (eV)	198 ± 45	210 ± 71	200 ± 40
χ^2_ν/ν	1.086/389	1.049/381	1.071/775

Detector	A0	B0	A0 and B0
Model 3: Absorbed power law with two emission lines *			
N_H (10^{22} cm $^{-2}$)	1.31 ± 0.04	...	1.30 ± 0.03
α	1.13 ± 0.02	...	1.12 ± 0.02
E_1 (keV)	6.77 ± 0.05	...	6.73 ± 0.09
σ_1 (keV)	0.18 ± 0.07	...	0.25 ± 0.13
EW_1 (eV)	128 ± 37	...	142 ± 54
E_2 (keV)	6.40 ± 0.03	...	6.40 ± 0.03
σ_2 (keV)	< 0.052	...	< 0.055
EW_2 (eV)	42 ± 18	...	36 ± 23
χ^2_ν/ν	1.069/386	...	1.066/770

Detector	A0	B0	A0 and B0
Model 4: Absorbed power law with narrow lines fixed at 6.4, 6.7, 6.93, and 7.53 keV			
N_H (10^{22} cm $^{-2}$)	1.31 ± 0.04	1.28 ± 0.06	1.30 ± 0.03
α	1.13 ± 0.02	1.08 ± 0.03	1.12 ± 0.01
$EW_{6.4}$ (eV)	53 ± 14	54 ± 20	53 ± 11
$EW_{6.7}$ (eV)	60 ± 15	41 ± 21	54 ± 12
$EW_{6.93}$ (eV)	41 ± 15	< 38	33 ± 12
$EW_{7.53}$ (eV)	26 ± 17	< 22	17 ± 14
χ^2_ν/ν	1.063/388	1.076/380	1.074/774

*When this model is fit to the B0 data the two lines become degenerate.

Note. — All errors are for 90% confidence in one interesting parameter.

There is also a feature at 7.5 keV which corresponds to K_{α} emission from neutral nickel. It is doubtful that this is astrophysical in origin because there are residuals around 7.5 keV in both central pixels when the Crab spectrum is fit (Weaver et al. 1995). It is possible that this line is due to fluorescence in the nickel mesh of the detector's blocking filter. When this feature is fit by a narrow line in the A0 data it is significant at the 2σ level. It is not required by the B0 data and when it is included in a fit to B0 an equivalent width consistent with zero results.

Fitting a blend of three narrow lines to the iron emission feature instead of a broad and a narrow line yields a χ^2 which is not significantly different. Such a fit to the A0 data is shown in Figure 5.8. It includes another narrow line which is significant at the 2σ confidence level to fit the suspected nickel feature. The energies of these lines were fixed at 6.4, 6.7, 6.93, and 7.53 keV, corresponding to emission by un-ionized iron, helium- and hydrogen-like iron and un-ionized nickel. Thus the data are consistent with either a broad line or a blend of narrow lines with physically plausible energies. In an attempt to distinguish between the two line and four line models, the energy range was restricted to 5.5–8 keV and the data were fitted with the continuum parameters held fixed. The continuum parameters were those obtained from fits to the 1–12 keV data. F-tests (Bevington 1969) were still unable to distinguish between the two models.

An attempt was made to improve the counting statistics and uncertainties by relaxing the data quality filter. Fits were made to data in which the only events rejected were those that had the VLE, pulse-pulse, or pixel-pixel flags set. The resulting light curve was flat as the telescope passed through the SAA, indicating that contaminating events were being rejected without significant loss

of good data. This is because most of the background events from the SAA were at low energies and had already been rejected by restricting the analysis to energies above 1 keV. The spectral parameters agreed with those obtained from fits to the data which had all flagged events removed. The uncertainties in the derived parameters are slightly smaller with the relaxed quality filter but all of the fits have unacceptably high values of χ^2 .

5.2.3 Pulse phase resolved spectroscopy

To investigate the dependence of the spectral parameters on pulse phase the A0 data were binned into five phase bins and the data from each phase bin were fit to an absorbed power law with one Gaussian emission line at ~ 6.7 keV. No significant variation in the intensity of the iron line was seen. However, due to the poor counting statistics, the data do not rule out the presence of variability. The 90% confidence upper limit on the variation in line strength is 70%, which is consistent with the 50% variation in iron line intensity detected by Day et al. (1993) in Ginga data. There is some evidence for variation of the column density and photon index with pulse phase. The best-fit values of these parameters are plotted against pulse phase in Figure 5.7. The column density appears to vary in phase with the flux and the photon index appears to vary roughly 180 degrees out of phase with it. This apparent flattening of the continuum at the pulse peak has been observed before (White et al. 1983). These variations may be due to changes in the emission geometry which occur as the neutron star rotates, or, more likely, they may indicate that these models are too simple and that the continuum is more complex than a single absorbed power law.

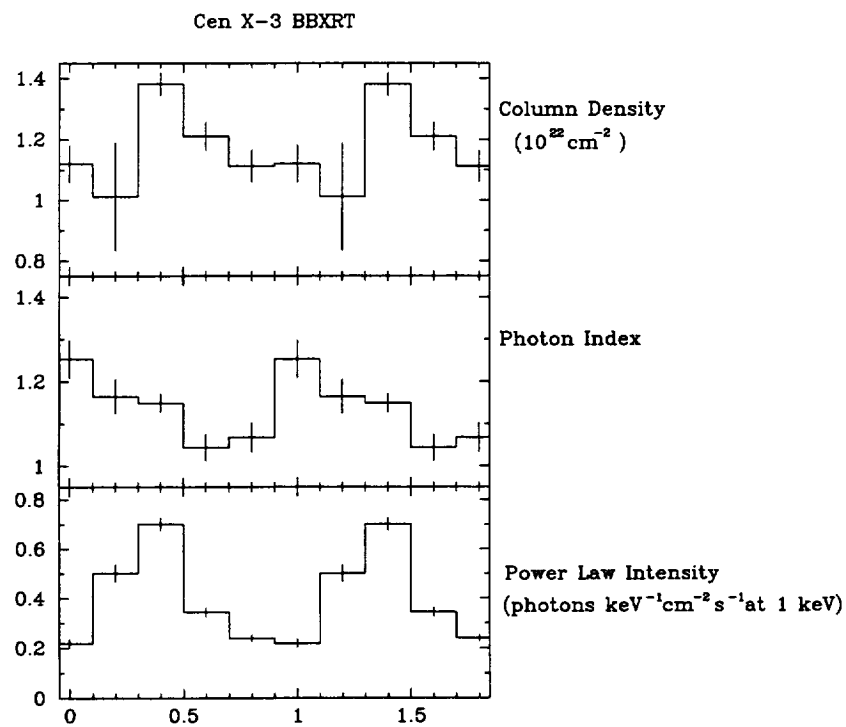


Fig. 5.7— Variation of spectral parameters with pulse phase. Error bars represent 90% confidence intervals.

5.3 Discussion

5.3.1 The pulse profile

The pulse profile observed with BBXRT is single-peaked with a weak secondary pulse. The secondary pulse appears slightly weaker at low energies. The pulse profile is similar to that seen in previous observations of Cen X-3 most of the time (e.g. White et al. 1983). However, the pulse profile observed during the Ginga observation had two peaks of comparable amplitude. This double-peaked pulse profile is seen only rarely (e.g. Long et al. 1975; Tuohy 1976; Nagase et al. 1992).

The unabsorbed luminosity observed with BBXRT was $3.29 \times 10^{37} \text{ erg s}^{-1}$ in the 2–10 keV band assuming a distance of 8 kpc. This value was derived using the relaxed data quality filter described in Section 5.2.2 in order to minimize the effect of rejected events. In the high post-egress phase of the Ginga observation the 1–37 keV luminosity was $5 \times 10^{37} \text{ erg s}^{-1}$ which corresponds to a luminosity in the 2–10 keV band of $2.4 \times 10^{37} \text{ erg s}^{-1}$. This indicates that the differences in the pulse profile of Cen X-3 observed with Ginga and BBXRT may be due to luminosity induced changes in the structure of the accretion column as observed in EXO 2030+375 (Parmar et al. 1989). Precession of the neutron star or variable obscuration might also be involved.

5.3.2 The Fourier power spectrum

Quasi-periodic oscillations (QPO) were discovered with EXOSAT observations of Cen X-3 (Tennant 1988). They are also present in Ginga (Takeshima et al. 1991) and BBXRT data. Takeshima et al. argue that the Ginga data are consis-

tent with the beat frequency mass accretion model of QPOs (Alpar and Shaham 1985; Shibazaki and Lamb 1987). This model assumes the presence of a Keplerian disk in which there are density and magnetic field fluctuations and is thus appropriate since Cen X-3 is believed to be a magnetized neutron star with disk accretion. Interactions between the magnetosphere of the neutron star and fluctuations in the inner disk give rise to modulation of the mass accretion rate, and hence the X-ray luminosity. This modulation is at a harmonic of the beat frequency between the rotation frequency of the neutron star and that of the magnetospheric boundary layer. Thus the QPOs in Cen X-3 are consistent with the existence of an accretion disk.

The QPO detected with BBXRT has a centroid frequency of 40.7 ± 1.1 mHz while the value obtained by Takeshima et al. was 35 ± 2 mHz. If the beat frequency model is correct, the angular frequency of the QPO will be $\omega = \Omega_K(r_A) - \Omega_0$ if the pulsar is spinning up or $\omega = \Omega_0 - \Omega_K(r_A)$ if it is spinning down, assuming that ω is the fundamental beat frequency. Here r_A is the Alfvén radius which represents the inner edge of the accretion disk, $\Omega_K(r_A) = (GM)^{\frac{1}{2}} r_A^{-\frac{3}{2}}$ is the Keplerian angular frequency at that radius, and Ω_0 is the angular frequency of the magnetosphere which co-rotates with the neutron star. Long term monitoring of Cen X-3 with the BATSE instrument on the Compton Gamma Ray Observatory (Finger et al. 1994) has revealed that the spin up of the pulsar is accomplished by alternating episodes of increase and decrease in the pulse period at rates greater than the average spin up rate. This indicates that the accretion rate is such that the neutron star is close to equilibrium between magnetic braking and angular momentum accretion. The low frequency of the QPO also suggests that the Keplerian rotation frequency at the magnetic boundary layer

is close to the rotation frequency of the magnetosphere, as would be expected if the system is close to equilibrium between spinning up and spinning down. At the time of the BBXRT observation the pulsar could be either spinning up or down so that $\Omega(r_A) = \Omega_0 \pm \omega$ which implies

$$r_A = 5.1 \times 10^8 (\Omega_0 \pm \omega)^{-\frac{1}{2}} \left(\frac{M}{M_\odot} \right)^{\frac{1}{3}} \text{ cm.} \quad (5-1)$$

The Alfvén radius may also be estimated from the magnetic dipole moment and mass accretion rate (Elsner and Lamb 1977):

$$r_A = 3.2 \times 10^8 \dot{M}_{17}^{-\frac{2}{7}} \mu_{30}^{\frac{4}{7}} \left(\frac{M}{M_\odot} \right)^{-\frac{1}{7}} \text{ cm.} \quad (5-2)$$

Here μ_{30} is the magnetic dipole moment of the neutron star in units of 10^{30} G cm^3 and \dot{M}_{17} is the mass accretion rate in units of 10^{17} g s^{-1} . In terms of the luminosity $\dot{M} = L/c^2 \epsilon$ where ϵ is the energy conversion efficiency for 2–10 keV X-rays. Thus the magnetic dipole moment is

$$\mu_{30} = 2.4 (\Omega_0 \pm \omega)^{-\frac{7}{6}} L_{37}^{\frac{1}{2}} \epsilon_{0.1}^{-\frac{1}{2}} \left(\frac{M}{M_\odot} \right)^{\frac{5}{6}} \quad (5-3)$$

where $\epsilon_{0.1}$ is the conversion efficiency in units of 0.1. With $\Omega_0 = 1.3040 \text{ rad s}^{-1}$, $\omega = 0.2557 \text{ rad s}^{-1}$, $L_{37} = 3.29$, and assuming that the pulsar is spinning up this yields the value

$$\mu = 2.6 \times 10^{30} \epsilon_{0.1}^{-\frac{1}{2}} \left(\frac{M}{M_\odot} \right)^{\frac{5}{6}} \text{ G cm}^3. \quad (5-4)$$

This corresponds to a surface magnetic field

$$B = \frac{2.6 \times 10^{12} \epsilon_{0.1}^{-\frac{1}{2}} \left(\frac{M}{M_\odot} \right)^{\frac{5}{6}}}{R_6^3} \text{ G} \quad (5-5)$$

where R_6 is the neutron star radius in units of 10^6 cm .

The value obtained from the BBXRT data for the surface magnetic field of Cen X-3 may be used to estimate the energy of the fundamental cyclotron resonance. The observed fundamental energy of a cyclotron resonance feature is

$$E_{obs} = \frac{E_0}{1+z} \quad (5-6)$$

where

$$E_0 = 11.6 \times \left(\frac{B}{10^{12} \text{ G}} \right) \text{ keV} \quad (5-7)$$

and

$$z = \left(1 - \frac{2GM}{Rc^2} \right)^{-\frac{1}{2}} - 1 \quad (5-8)$$

is the gravitational redshift. Thus the observed energy of the fundamental cyclotron resonance is expected to be

$$E_{obs} = \frac{29 \varepsilon_{0.1}^{-\frac{1}{2}} \left(\frac{M}{M_\odot} \right)^{\frac{5}{6}}}{R_6^3} \sqrt{1 - \frac{0.41}{R_6}} \text{ keV}. \quad (5-9)$$

If on the other hand the pulsar is spinning down

$$B = \frac{4.2 \times 10^{12} \varepsilon_{0.1}^{-\frac{1}{2}} \left(\frac{M}{M_\odot} \right)^{\frac{5}{6}}}{R_6^3} \text{ G} \quad (5-10)$$

and

$$E_{obs} = \frac{48 \varepsilon_{0.1}^{-\frac{1}{2}} \left(\frac{M}{M_\odot} \right)^{\frac{5}{6}}}{R_6^3} \sqrt{1 - \frac{0.41}{R_6}} \text{ keV}. \quad (5-11)$$

However this situation is unlikely as in this case the incoming matter would be repelled by a centrifugal barrier and the source would switch off.

If the emission region extends far enough above the neutron star surface to sample a smaller B field the observed energy of the cyclotron feature will be less than this. Nagase et al. (1992) report that the shape of the spectrum of Cen X-3

is consistent with a high energy roll off of the form $\exp(-L(E))$ where

$$L(E) = \frac{\tau(W E/E_0)^2}{(E - E_0)^2 + W^2} \quad (5-12)$$

The form of this roll off is that of a cyclotron scattering resonance feature where E_0 is the energy of the resonance and W is its width. The fit obtained to the Ginga data by Nagase et al. suggested that $E_0 = 30 \pm 2$ keV. However this result is inconclusive as the inferred resonance energy was at the upper limit of the LAC's bandpass. Makishima et al. (1992) described the cyclotron resonance features detected with Ginga in several X-ray pulsars. The observed resonance energies ranging from 7 to 40 keV imply surface magnetic fields of $(0.6 - 3.5) \times 10^{12}$ G. The lack of definite evidence for a cyclotron feature below 30 keV suggests that Cen X-3 may have a relatively larger surface magnetic field. The values estimated from the QPO are consistent with this.

5.3.3 Comparison of results with previous observations of the iron line

Although the evidence for a 6.4 keV line is weak in this observation, the Ginga observations of 1989 are consistent with lines at both 6.4 and 6.7 keV (Nagase et al. 1992). However, the resolution of the instrument was not sufficient to determine their widths. As mentioned in Section 4.5, these lines were observed with Ginga as the pulsar went into eclipse. The 6.7 keV line underwent a gradual, partial eclipse, while that of the 6.4 keV line was abrupt. This indicated that the sizes of the emission sites of the 6.4 and 6.7 keV lines were $\lesssim 3 \times 10^{10}$ cm and $\gtrsim 8 \times 10^{11}$ cm respectively. Also, the assumed stellar wind density ($\sim 10^{22}$ cm $^{-2}$) was too small to produce the 180 eV equivalent width observed with Ginga for the

6.4 keV line. Thus, it was concluded that the 6.4 keV line was due to fluorescence of relatively un-ionized matter near the accretion disk and the 6.7 keV line was due to fluorescence of the extended ionized stellar wind.

The Alfvén radius may be estimated from Section 5.3.2 as $r_A \approx 4 \times 10^8$ cm which is close to the value obtained by Nagase et al. for the size of the 6.4 keV emission region. Line emission would not be expected from inside the magnetosphere because of the extreme ionization conditions there. This suggests that fluorescence of material in the inner accretion disk is responsible for the 6.4 keV emission.

At the same orbital phase as the BBXRT observation, the line luminosities derived from the Ginga observation were 5×10^{35} erg s⁻¹ for the the 6.4 keV line and $\sim 1 \times 10^{35}$ erg s⁻¹ for the 6.7 keV line, assuming a distance of 8 kpc. The unabsorbed line luminosities found with BBXRT were 1.3×10^{35} and 5×10^{35} erg s⁻¹ respectively, assuming the same distance. In order to check this, the A0 data were rebinned so that their resolution matched that of the Ginga LAC (Makino and the ASTRO-C Team 1987). The iron emission was fit with a single Gaussian. The best fit line energy was 6.63 ± 0.09 keV. The value obtained with Ginga for the line energy in the high post-egress orbital phase was 6.50 ± 0.08 keV, reflecting the different relative intensities of the 6.4 and 6.7 keV components. The lower equivalent width obtained for the 6.4 keV line during the BBXRT observation could be produced by reprocessing in a wind of column density $\sim 10^{22}$ cm⁻² (Makishima 1986). It is possible that luminosity dependent changes in the angular distribution of emission from the neutron star could alter the relative strengths of the 6.4 and 6.7 keV lines, especially if they are produced at different reprocessing sites.

5.3.4 The origin of the broad emission feature at 6.7 keV

A possible source of the 6.7 keV line emission is the surface of the companion star which faces the pulsar. The considerable X-ray heating of the stellar surface might produce the high temperatures and ionization required for a broad 6.7 keV emission line. In fact Day and Stevens (1993) have suggested that ionization conditions at the companion's surface are so extreme that a radiatively driven stellar wind cannot exist and the wind is instead driven by X-ray heating. It is possible that if one of the pulsar beams is sweeping across the face of the companion star it could cause fluorescence, giving rise to a pulsing 6.7 keV line. However, since the line undergoes only a partial eclipse (Nagase et al. 1992) at least some of the emission must come from a more extended source such as an ionized stellar wind. Another possibility is that the source of the 6.7 keV line is relatively compact and that the partial eclipse seen in the Ginga data and the broadening might be due to scattering in an extended medium. If a significant fraction of the photons from this line are scattered by electrons in the stellar wind, this might explain the partial eclipse seen in the Ginga data. However, the column density of the wind (Nagase et al. 1992) is too low to produce significant Compton scattering ($\tau \sim \sigma_T N_H \sim 10^{-2}$).

If the 6.7 keV line is produced by fluorescence in the stellar wind its observed equivalent width should be compatible with the wind column density. An estimate of the equivalent width from K fluorescence of iron in an optically thin slab is given by Kallman (1991) as

$$EW = \varepsilon_{line} \frac{L(\varepsilon_{th})}{L(\varepsilon_{line})} \sigma_{th} \omega_K x y N \quad (5-13)$$

where ε_{line} is the line energy, $L(\varepsilon_{th})$ is the ionizing specific luminosity at the

threshold energy for K shell photoionization, $L(\varepsilon_{line})$ is the ionizing specific luminosity at the line energy, σ_{th} is the cross section for K shell photoionization at the threshold energy, ω_K is the fluorescence yield, x is the fraction of the iron in the ionization state of interest, y is the iron abundance, and N is the equivalent hydrogen column density. For a 6.7 keV line due to emission by Fe XXV, $\omega_K \sim 0.5$ (Krolik and Kallman 1987), $\varepsilon_{th} = 8.8$ keV (Lotz 1968), and $\sigma_{th} = 2 \times 10^{-20} \text{ cm}^2$ (Reilman and Manson 1978). Taking $y = 3 \times 10^{-5}$ (solar abundance) yields an equivalent width

$$EW = 1.5 \text{ keV } N_{24} x \quad (5-14)$$

where N_{24} is the equivalent hydrogen column density in units of 10^{24} cm^{-2} . An equivalent width of $\sim 120 \text{ eV}$ implies a column density of $\sim 8 \times 10^{22} \text{ cm}^{-2}$, assuming that $x = 1$. From the size of the 6.7 keV line emission site and the ratio of the scattering continuum to the intrinsic emission Nagase et al. (1992) estimated a column density of stellar wind of a few times 10^{22} cm^{-2} . Thus the column density of the ionized wind may be sufficient to produce the observed equivalent width.

Bulk motions of the wind might explain the large width of the 6.7 keV line. Speeds of the order of 9000 km s^{-1} would be required to produce a broadening $\Delta E_{FWHM} \sim 400 \text{ eV}$. Another possible broadening mechanism is the thermal motions of the wind. However an ion temperature of $\sim 10^{11} \text{ K}$ would be required to produce the observed width. If the broad 6.7 keV line originates near the magnetosphere where there are very high rotation velocities ($\sim 5000 \text{ km/s}$) Doppler broadening could easily account for the observed width.

A more likely explanation is that the 6.7 keV line is a blend of several narrow resonance and fluorescence lines of Fe XXI–Fe XXVI with energies ranging from

6.5 to 6.9 keV. This interpretation is supported by ASCA observations of Cen X-3 during eclipse (Ebisawa et al. 1996). The iron K emission was resolved into three lines at 6.4, 6.7, and 7.0 keV. While one would expect the spectrum of the source to be qualitatively different during eclipse because of the obscuration of the pulsar, it is not unlikely that these emission lines could be present outside of eclipse. Figure 5.8 shows the data with such a multiple line fit. A 2σ narrow line at 7.5 keV is also included which may be an instrumental feature due to Ni K_{α} . The narrow lines have equivalent widths typically $\lesssim 50$ eV which is consistent with fluorescence in the stellar wind. Although the fit is not statistically better than for the two line model, the most plausible explanation for the large physical width of the iron emission feature is that it is in fact a blend of narrow lines. The fact that using physically plausible line energies in the multiple line model does not make the fit worse also supports this. These data are consistent with a picture in which the H- and He-like lines originate in the photoionized stellar wind, which accounts for the gradual eclipse of the features observed with Ginga. The 6.4 keV line would be produced mainly by fluorescence of material irradiated by the X-ray beams. A clear prediction of this model is that the 6.4 keV line should be pulsed at the 4.8 s spin period. Day et al. (1993) were unable to determine which of the iron lines were pulsating. For the BBXRT data counting statistics only allow an upper limit of 70% on the amplitude of any pulsations.

5.4 Conclusions

The physical width of the 6.7 keV iron line in Cen X-3 has been measured for the first time out of X-ray eclipse. The blending of several lines from highly

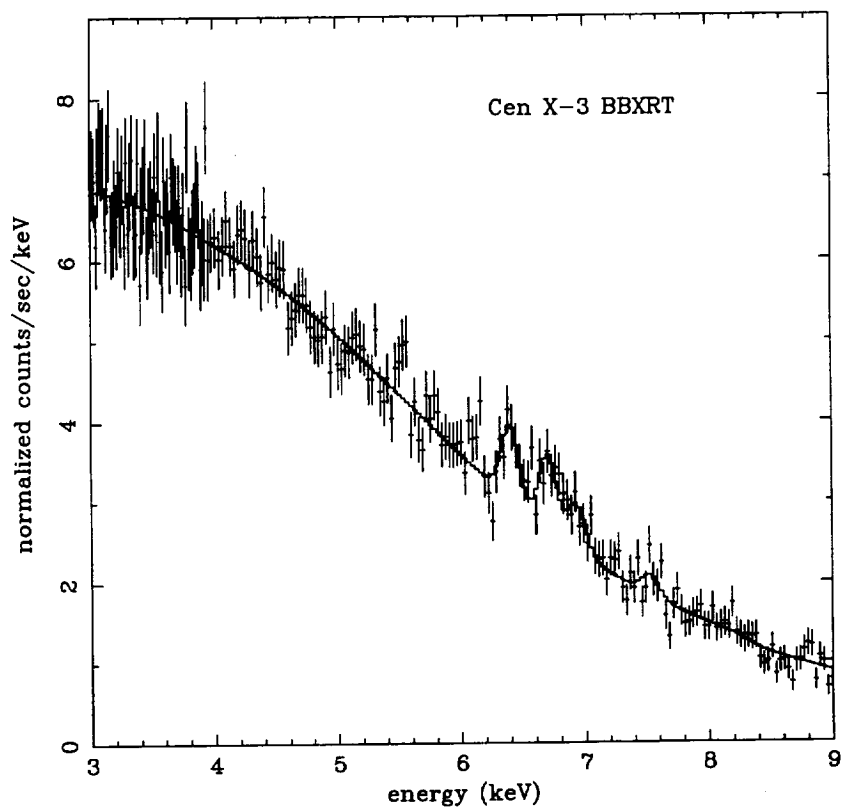


Fig. 5.8— Folded A0 data fit to four narrow lines with energies 6.4, 6.7, 6.93, and 7.53 keV. These energies correspond to emission by un-ionized iron, helium- and hydrogen-like iron, and un-ionized nickel.

ionized iron must be invoked to explain the width of this line if it originates in the extended stellar wind. If this is in fact the case, ASCA should be able to easily resolve these lines. The presence of iron emission at 6.4 keV and 6.7 keV simultaneously indicates that there are at least two distinct emission sites. Fluorescence in a localized region of relatively low ionization is most likely responsible for the 6.4 keV emission. The broad 6.7 keV feature is a blend of several narrow lines due to the scattering of radiation from the neutron star in an extended highly ionized stellar wind. One would then expect to observe pulsations in the 6.4 keV line. If the size of the source of the 6.7 keV emission feature is greater than $\sim 8 \times 10^{11}$ cm, as the Ginga observations indicate, any pulsations in the 6.7 keV line should be washed out by the light travel time across the source. Another objection to pulsations of the 7.6 keV line caused by illumination of the stellar wind by the beamed X-ray emission of the pulsar is that the pulse might be smeared out by the wind's finite recombination time. Nagase et al. (1992) estimated that the average electron density in the region where $\xi > 10^3$ was $5 \times 10^{10} \leq n_e \leq 8 \times 10^{11} \text{ cm}^{-3}$. Using the fitted formulae of Arnaud and Raymond (1992) for the radiative recombination and dielectronic recombination coefficients ($\alpha_r(T)$ and $\alpha_{di}(T)$, respectively), and assuming $n_e = 10^{11} \text{ cm}^{-3}$ and $T = 10^4$ K, the recombination rate for Fe XXVI will be

$$1/\tau_{\text{recomb}} = (\alpha_r(T) + \alpha_{di}(T))n_e = 58.4 \text{ s}^{-1}. \quad (5-15)$$

Thus Fe XXV that has been photoionized by the pulsar's beam will recombine on a timescale of $\tau_{\text{recomb}} \approx 0.02$ s which is much shorter than the 4.8 s pulse period. Thus, the recombination time of Fe XXVI to Fe XXV should not significantly smear out any pulsation of the 6.7 keV line.

No significant variations with pulse phase in the intensity of either iron line

were detected in the BBXRT data. The 90% confidence upper limit on the variation in line strength is 70%, which is consistent with with the detection reported by Day et al. (1993).

Chapter 6

The Continuum Spectrum — EXOSAT GSPC

6.1 Motivation

My study of these data was motivated by the tentative identification by Nagase et al. (1992) of the high energy cut-off in Cen X-3's spectrum with cyclotron opacity. It seemed that, if a CSRF was detectable, pulse phase resolved measurements would help distinguish between a slab and a column emission geometry which cause radiation to be emitted as pencil or fan beams, respectively (see Figures 1.9 and 1.8). The energy of a cyclotron absorption feature is expected to be greatest when the angle between the line of sight and the magnetic field is zero (Mészáros and Nagel 1985a). Thus for a pencil beam the CSRF energy should be greatest at the pulse maximum (when the line of sight is closest to the magnetic field direction). For a fan beam it should be at a minimum at the pulse maximum (when the line of sight is normal to the magnetic field). Comparing their calculations with observations of the CSRF in Her X-1 Mészáros and Nagel (1985b) concluded that the pulsar radiated as a pencil beam. For luminous pulsars such as Her X-1 and Cen X-3 it is expected that there is a radiation deceleration shock above the surface of the neutron star producing a column geometry and

a fan beam (e.g. Wang and Frank 1981). In the case of 4U 1538-52, Bulik et al. (1992) modeled the pulse phase dependence of the spectrum. They obtained quantitative agreement with pulse phase resolved observations of the cyclotron line made with Ginga and found evidence for differences in temperature and opening angle for the polar caps.

6.2 The Observations

Cen X-3 was observed by EXOSAT six times. In this chapter I consider data taken with the gas scintillation proportional counter (GSPC) during two of these observations when the source was in its high state. Four datasets were extracted from these two observations. The telescope is described by Peacock et al. (1981) and in Section 3.2.1. The GSPC observations of Cen X-3 have already been used to investigate the pulse-phase dependence of the iron line intensity by Takalo et al. (1990). Thus I will concentrate on the shape of the continuum spectrum in this study. Takalo et al. combined GSPC data from three observations including the present two and detected pulsations. They also divided their data into five orbital phase bins. Because of the variable nature of the source I chose to keep the observations separate. The datasets used in this analysis are listed in Table 6.1.

The GSPC's overall effective area (150 cm^2) is much smaller than that of the medium energy detector (ME; 1600 cm^2), but around 7 keV the efficiency of the GSPC becomes greater than that of an ME Ar detector half. In addition, the GSPC's energy resolution is better than that of the ME by a factor of two. Thus the GSPC is more suitable than the ME Ar detectors for iron line spectroscopy. Also, the GSPC's effective area is greater than that of the ME's Ar detectors

Table 6.1. The GSPC Data.

Dataset	Date	Orbital Phase	Exposure (s)	L_{37}^{\dagger}	EW^{\ddagger}
1	1985 May 21	0.81–0.91	16312	1.6	246 ± 11
2*	1985 May 22	0.95–0.13	31288	0.02	1700 ± 1200
3	1985 May 22	0.30–0.60	10776	2.1	250 ± 11
4	1985 August 9	0.61–0.87	45072	2.7	249 ± 12

*Eclipse

\dagger Unabsorbed luminosity in the 2–20 keV band in units of 10^{37} erg s $^{-1}$ assuming a distance of 8 kpc.

\ddagger Pulse-phase averaged iron line equivalent width (eV).

at high energies. The effective energy range of the GSPC was 2–25 keV for the gain settings of the present data. Previous studies of data from the ME have investigated the orbital and pulse phase dependence of the iron line amplitude and have used the fitted column density as a probe of the structure of the stellar wind (e.g. Day and Stevens 1993).

6.3 Data Analysis and Results

6.3.1 Background Subtraction

The data had barycentric corrections and orbital motion corrections applied before being extracted into twenty pulse-phase resolved spectra. The pulse-phase average spectra were also extracted. For the 1985 May data the slow spectrum was used as background. The background subtraction is acceptable between 2 and 25 keV and this was the energy range chosen for spectral fitting. For the 1985 August data we used the standard blank sky background because of a lack of good slow data. In this case the subtraction was worse and the energy range for fitting was restricted to 3–24 keV.

6.3.2 Spectroscopy of the pulse-phase averaged data

The high state non-eclipse spectrum

Three different forms for the continuum spectrum were compared with the data. The first was the canonical power law with an exponential cut-off. This did not give acceptable fits, as shown in Table 6.2. The second was a black body with thermal bremsstrahlung. Takalo et al. (1990) report that this was the model

that fitted the Cen X-3 GSPC spectra best. The best-fit parameters with this model are shown in Table 6.3. The third was the non-relativistic Comptonization model of Sunyaev and Titarchuk (1980). I chose this in preference to the NPEX model of Mihara (1995) because it has fewer free parameters with more direct physical interpretations. There is a caveats, however. Since this Comptonization model is appropriate for a non-magnetized cloud of hot electrons it is unclear how well the derived parameters will apply to the conditions in Cen X-3's accretion column. Nevertheless, the large optical depth ($\tau \sim 17$) would appear to make the details of the geometry less important. The fact that this model fits the data well justifies its use. The fit results are shown in Table 6.4. Most of the contributions to χ^2 in fits to the cut-off power law model come from the high energy part of the spectrum. It was found that this model gave improved fits to the pulse-phase averaged data with the addition of a CSRF. This is similar to what was also seen in Ginga observations of Cen X-3 (Nagase et al. 1992). The fitted cyclotron energy inferred from the Ginga data was higher at around 30 keV, however, which is close to the upper end of the bandpass of the Ginga LAC. Thus a fourth model was selected: a power law with cyclotron absorption, as shown in Table 6.5. The pulse-phase average spectra are shown in Figures 6.1, 6.2, and 6.3.

The pulse phase averaged equivalent width of the iron line is ~ 200 eV. The spectra did not require an iron absorption edge deeper than that due to the interstellar absorption. For dataset 1 the 90% confidence upper limit of the depth of an absorption edge at 7 keV is 1.39×10^{-2} . This would be expected to produce an iron K_{α} fluorescence line at 6.4 keV with an equivalent width of at most 16 eV if the fluorescing medium surrounds the source. The iron line was

Table 6.2. Pulse-phase average data fitted to a cut-off power law.

Dataset:	1	3	4
N_H (10^{22} cm $^{-2}$)	1.8 ± 0.2	2.6 ± 0.2	2.31 ± 0.07
α	1.28 ± 0.02	1.28 ± 0.02	1.34 ± 0.03
I_{PL} (cts s $^{-1}$ keV $^{-1}$ at 1 keV)	0.62 ± 0.03	0.81 ± 0.03	1.18 ± 0.09
E_c (keV)	11.8 ± 0.38	11.0 ± 0.1	11.5 ± 0.1
E_f (keV)	8.4 ± 0.6	9.6 ± 0.3	8.8 ± 0.2
E_{Fe} (keV)	6.46 ± 0.05	6.63 ± 0.04	6.55 ± 0.07
σ_{Fe} (keV)	0.51 ± 0.09	0.45 ± 0.07	0.85 ± 0.06
I_{Fe} (cts s $^{-1}$ keV $^{-1}$)	0.014 ± 0.002	0.018 ± 0.002	0.0324 ± 0.0008
χ^2_{ν} (d.o.f.)	1.618(156)	2.303(156)	2.343(134)

Table 6.3. Pulse-phase average data fitted to a black body and thermal bremsstrahlung.

Dataset:	1	3	4
N_H (10^{22} cm $^{-2}$)	2.2 ± 0.6	2.3 ± 0.2	1.4 ± 0.3
kT_{BB} (keV)	3.21 ± 0.08	3.21 ± 0.05	3.08 ± 0.05
R_{BB} (km)*	1.9 ± 0.8	1.9 ± 0.5	2.3 ± 0.4
kT_{Brem} (keV)	4.7 ± 1.6	8.6 ± 1.8	9.6 ± 1.2
I_{Brem} (cts s $^{-1}$ keV $^{-1}$ at 1 keV)	1.2 ± 0.3	1.13 ± 0.07	1.43 ± 0.08
E_{Fe} (keV)	6.40 ± 0.05	6.62 ± 0.04	6.44 ± 0.05
σ_{Fe} (keV)	0.3 ± 0.1	0.25 ± 0.06	0.38 ± 0.06
I_{Fe} (cts s $^{-1}$ keV $^{-1}$)	0.010 ± 0.002	0.012 ± 0.001	0.015 ± 0.002
χ^2_{ν} (d.o.f.)	1.237(156)	1.352(156)	0.997(134)

*Radius of emission region derived from the black body flux.

Table 6.4. Pulse-phase average data fitted to a Comptonization model.

Dataset:	1	3	4
N_H (10^{22} cm $^{-2}$)	1.1 ± 0.2	2.0 ± 0.2	1.3 ± 0.3
kT (keV)	3.55 ± 0.06	3.5 ± 0.04	3.40 ± 0.02
τ	17.1 ± 0.4	16.9 ± 0.3	17.1 ± 0.3
I (cts s $^{-1}$ keV $^{-1}$ at 1 keV)	0.57 ± 0.03	0.77 ± 0.03	1.01 ± 0.05
E_{Fe} (keV)	6.40 ± 0.05	6.62 ± 0.03	6.44 ± 0.05
σ_{Fe} (keV)	0.25 ± 0.09	0.23 ± 0.06	0.37 ± 0.06
I_{Fe} (cts s $^{-1}$ keV $^{-1}$)	0.008 ± 0.001	0.011 ± 0.001	0.014 ± 0.002
χ^2_{ν} (d.o.f.)	1.337(157)	1.238(157)	1.073(135)

Table 6.5. Pulse-phase average data fitted to a power law and CSRF.

Dataset:	1	3	4
N_H (10^{22} cm $^{-2}$)	0.9 ± 0.3	1.7 ± 0.3	0.8 ± 0.3
α	1.03 ± 0.06	0.96 ± 0.07	0.98 ± 0.05
I_{PL} (cts s $^{-1}$ keV $^{-1}$ at 1 keV)	0.42 ± 0.04	0.50 ± 0.05	0.68 ± 0.06
τ_{Cy}	2.5 ± 0.6	2.0 ± 0.3	1.68 ± 0.05
E_{Cy} (keV)	24 ± 2	22 ± 2	20.4 ± 0.5
W_{Cy} (keV)	14 ± 4	22 ± 8	16 ± 2
E_{Fe} (keV)	6.42 ± 0.05	6.62 ± 0.03	6.45 ± 0.05
σ_{Fe} (keV)	0.32 ± 0.08	0.25 ± 0.06	0.40 ± 0.06
I_{Fe} (cts s $^{-1}$ keV $^{-1}$)	0.010 ± 0.001	0.013 ± 0.001	0.017 ± 0.002
$\chi^2_{\nu}(\text{d.o.f.})$	1.164(155)	1.175(155)	0.781(133)

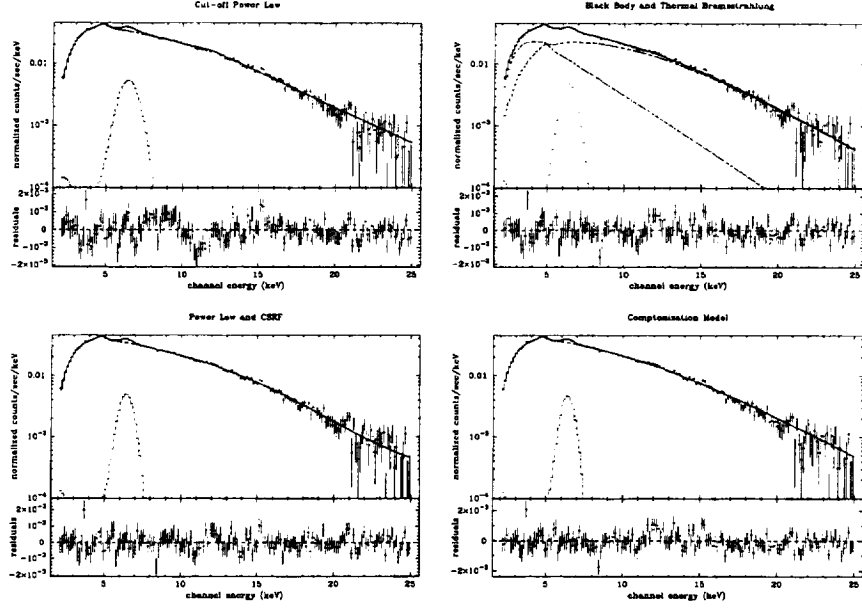


Fig. 6.1— Pulse-phase average data from dataset 1 fitted to different spectral models. Clockwise from upper left: power law with a high-energy exponential cut-off, black body and thermal bremsstrahlung, non-relativistic Comptonization model, power law with cyclotron absorption. Each model includes interstellar absorption and a Gaussian iron emission line.

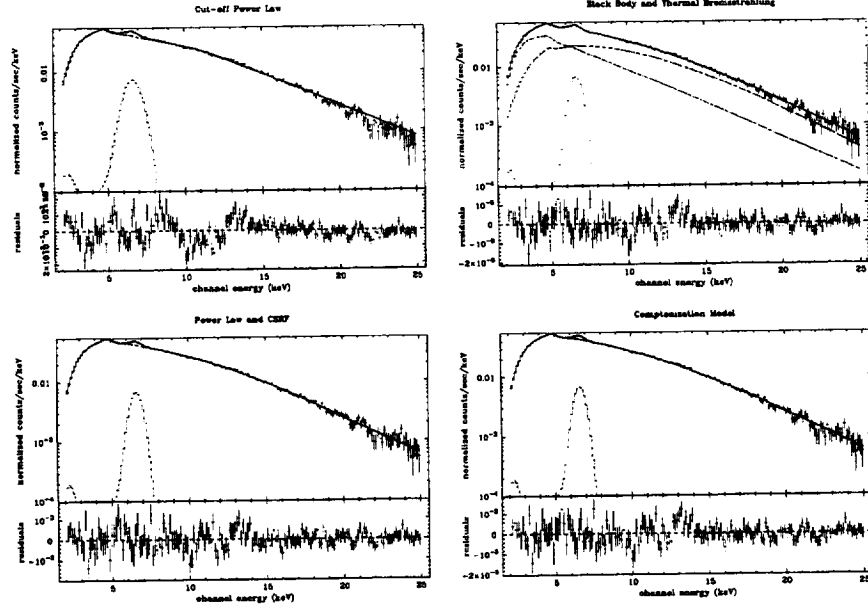


Fig. 6.2— Pulse-phase average data from dataset 3 fitted to different spectral models. Clockwise from upper left: power law with a high-energy exponential cut-off, black body and thermal bremsstrahlung, non-relativistic Comptonization model, power law with cyclotron absorption. Each model includes interstellar absorption and a Gaussian iron emission line.

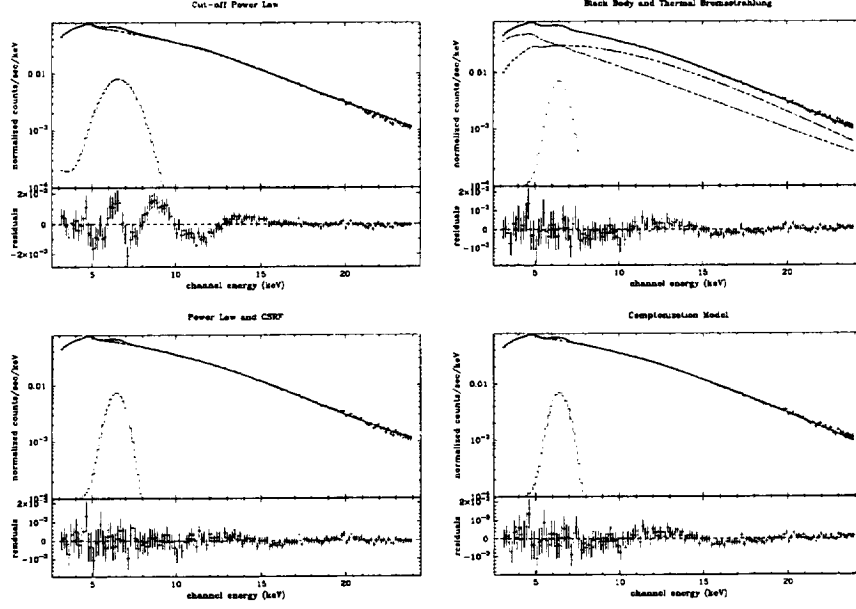


Fig. 6.3— Pulse-phase average data from dataset 4 fitted to different spectral models. Clockwise from upper left: power law with a high-energy exponential cut-off, black body and thermal bremsstrahlung, non-relativistic Comptonization model, power law with cyclotron absorption. Each model includes interstellar absorption and a Gaussian iron emission line.

better fit by a single Gaussian than by multiple narrow Gaussians.

An attempt was made to improve the counting statistics by simultaneously fitting the GSPC data from dataset 1 with contemporaneous data from the ME. Although acceptable fits to both the ME and GSPC data could be obtained separately, when the data were fit to the same model with only the overall normalization allowed to be different between the data sets, the fits were unacceptable. Allowing the GSPC gain to vary improved the fits but not enough to make them acceptable. Nevertheless, the best fit values of the overall normalizations of the data sets differed only by a few percent as did the calculated model fluxes. These slight differences between spectra derived from the ME and GSPC may be due to differences in background subtraction or to uncertainties in the responses. It should be noted that the ME has a much smaller effective area than the GSPC above 10 keV. The best fit model was a non-relativistic Comptonized spectrum with interstellar absorption and Gaussian iron emission. This had $\chi^2_\nu = 1.760$ for 224 degrees of freedom and $\chi^2_\nu = 1.31$ with the addition of 2% systematic errors to the model. When the energy range was restricted to 2–10 keV, however, $\chi^2_\nu = 1.033$ for 75 degrees of freedom. These fits are shown in Figure 6.4.

The eclipse spectrum

The eclipse spectrum (dataset 2) is well fit by a thermal bremsstrahlung model with a temperature of $7.2^{+9.5}_{-3.3}$ keV or $8^{+11}_{-4} \times 10^7$ K. There is also fluorescent iron emission with centroid energy 6.4 ± 0.1 keV. The line has no discernible physical width, with an upper limit of 0.28 keV. The line's intensity is $(1.3 \pm 0.5) \times 10^{-3}$ cts s⁻¹ cm⁻². The column density during eclipse is not well

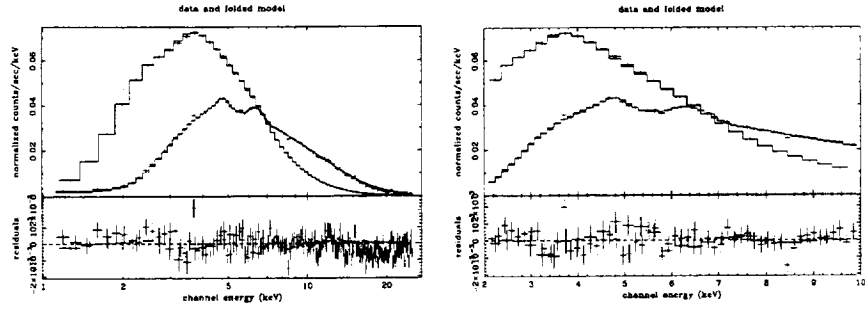


Fig. 6.4— Simultaneous fits to GSPC and ME Ar H1 data from dataset 1 in 1–25 and 2–10 keV energy ranges. The best model is a non-relativistic Comptonized spectrum with interstellar absorption and Gaussian iron emission.

constrained. The 90% confidence upper limit on N_H is $4.4 \times 10^{22} \text{ cm}^{-2}$. The drop in the iron line energy is due to recombination of the stellar wind during the X-ray eclipse. To see that this is reasonable, we can calculate the recombination rates using the fitted formulae of Arnaud and Raymond (1992) for the radiative recombination and dielectronic recombination coefficients ($\alpha_r(T)$ and $\alpha_{di}(T)$, respectively). Nagase et al. (1992) estimated that the average electron density in the region where $\xi > 10^3$ was $5 \times 10^{10} \leq n_e \leq 8 \times 10^{11} \text{ cm}^{-3}$. So, assuming $n_e = 10^{11} \text{ cm}^{-3}$ and $T = 10^4 \text{ K}$, the recombination rate for Fe II will be

$$1/\tau_{\text{recomb}} = (\alpha_r(T) + \alpha_{di}(T))n_e = 0.058 \text{ s}^{-1}. \quad (6-1)$$

The recombination rates increase with ionization stage as the screening of the central Coulomb field decreases. The recombination rate for Fe XXVI is 58.4 s^{-1} . Thus, when the neutron star is occulted by the companion, the photoionized stellar wind will recombine on a timescale τ_{recomb} that is short compared to the eclipse duration.

6.3.3 Pulse phase resolved spectroscopy

The data were divided into twenty pulse-phase resolved bins. The minimum number of counts per bin for dataset 1 was 2.6×10^4 which ensured adequate counting statistics. It was found that the column density, N_H , was not well constrained by either the GSPC or the ME. Thus in the pulse-phase resolved fits N_H was fixed at the best-fit value from the fits to the pulse-phase averaged data. Takalo et al. (1990) do not state which continuum parameters (if any) they held fixed in their pulse-phase resolved fits. In each case the iron line energy has no significant variation with pulse phase. Takalo et al. (1990) also report that the iron line energy is constant with pulse phase. Thus the iron line energy was fixed at the phase-average value. Takalo et al. (1990) fixed the iron line width at 0.1 keV for pulse-phase resolved spectroscopy. In the present analysis it is clear from the pulse-phase average fits that the iron line has a finite physical width and it is not appropriate to fit it with a narrow Gaussian. Thus the iron line physical width was fixed at the pulse-phase average value as was the cyclotron line width.

The pulse-phase dependence of the fitted parameters is shown in Figures 6.5, 6.6, and 6.7. The pulse-phase dependence of the iron line intensity is consistent with the results of Takalo et al. (1990).

6.4 Discussion and Conclusions

6.4.1 The pulse profile

The pulse profile derived from dataset 1 consists of an asymmetric main peak separated from a smaller peak by 180° . In dataset 3 the pulse profile is triple-

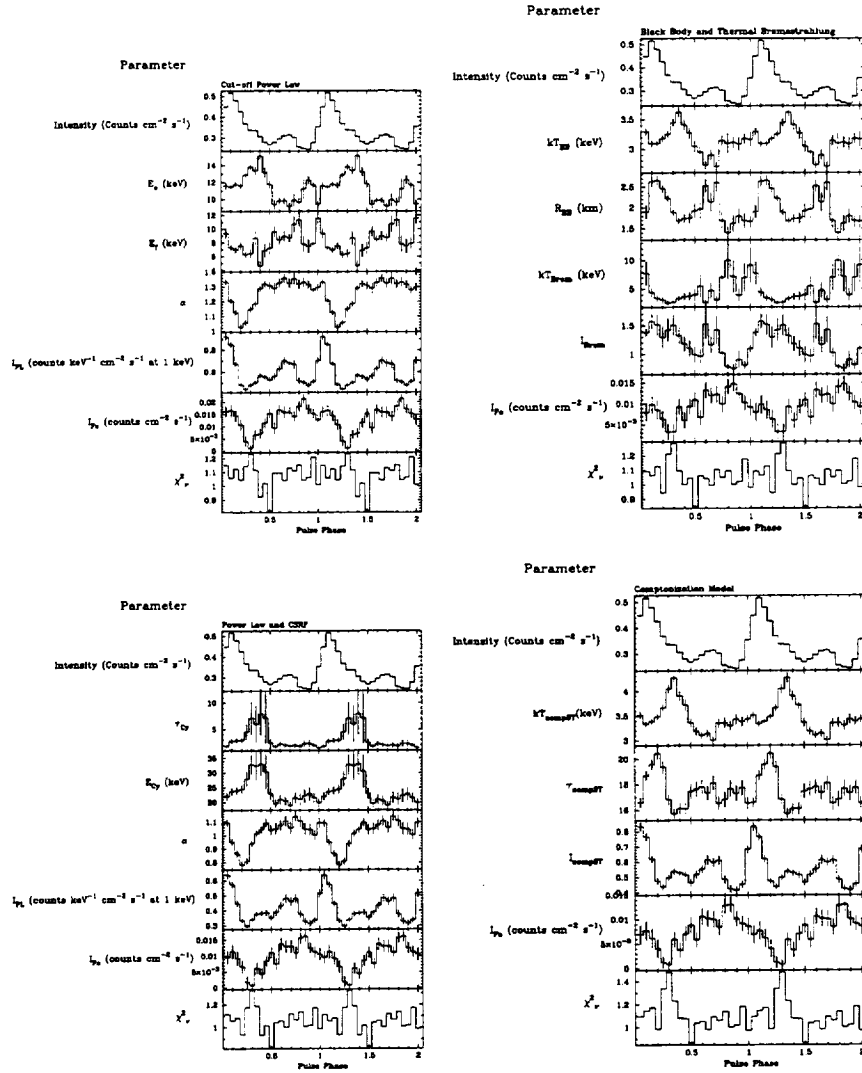


Fig. 6.5— Variation of spectral parameters with pulse phase. The data from dataset 1 were fitted to four different models. Clockwise from upper left: power law with interstellar absorption and an exponential cut-off, black body and thermal bremsstrahlung, non-relativistic Comptonization model, power law with cyclotron absorption. The iron line energy and width and the column density were fixed at the pulse-phase average values.

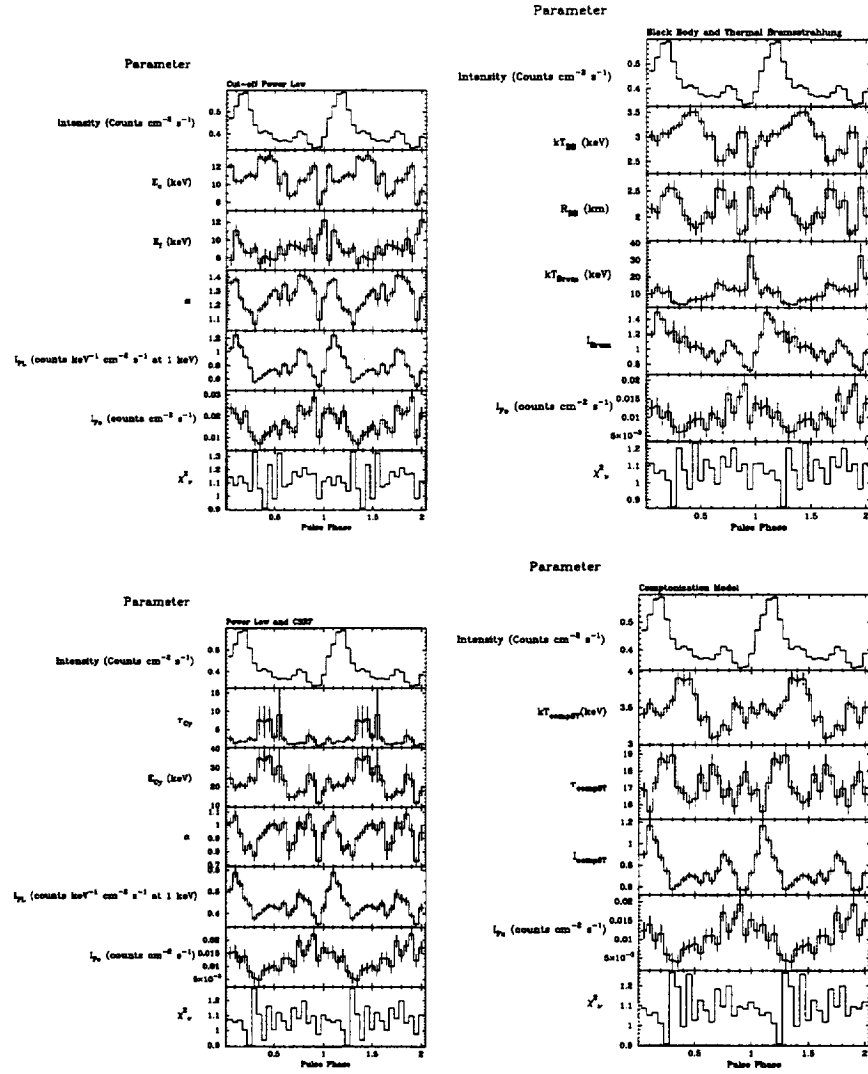


Fig. 6.6— Variation of spectral parameters with pulse phase. The data from dataset 3 were fitted to four different models. Clockwise from upper left: power law with interstellar absorption and an exponential cut-off, black body and thermal bremsstrahlung, non-relativistic Comptonization model, power law with cyclotron absorption. The iron line energy and width and the column density were fixed at the pulse-phase average values.

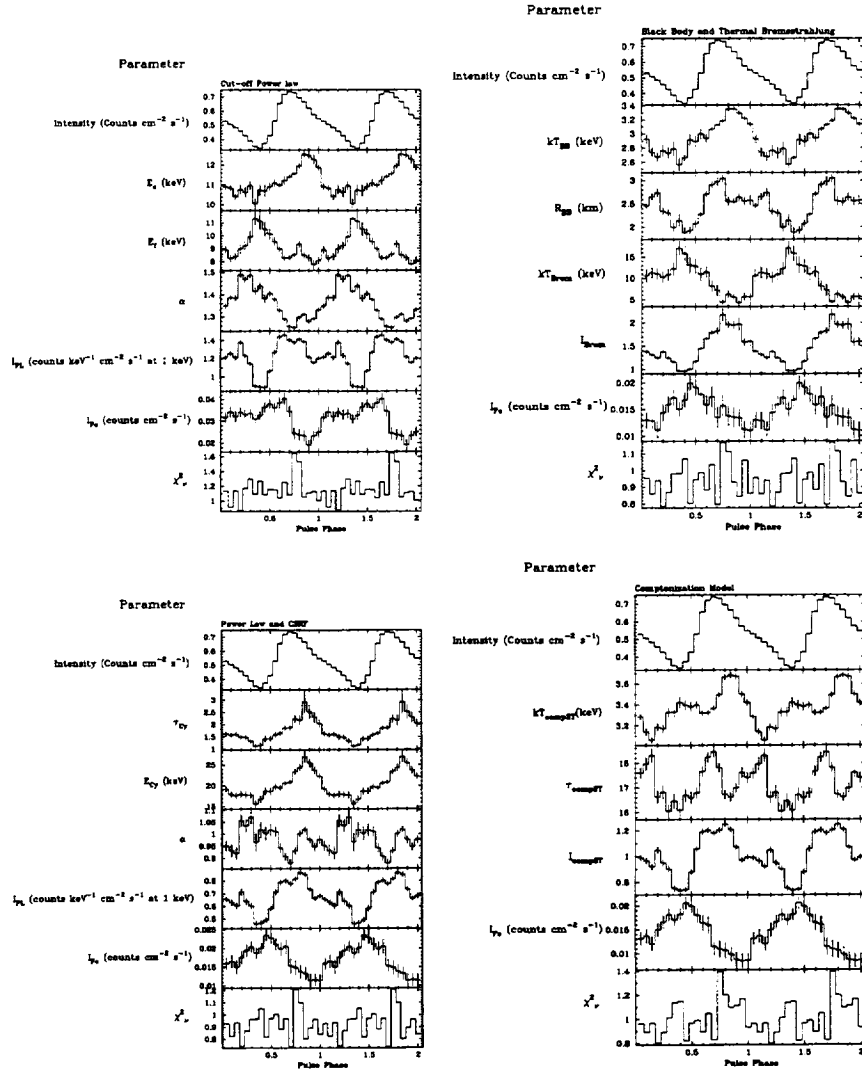


Fig. 6.7— Variation of spectral parameters with pulse phase. The data from dataset 4 were fitted to four different models. Clockwise from upper left: power law with interstellar absorption and an exponential cut-off, black body and thermal bremsstrahlung, non-relativistic Comptonization model, power law with cyclotron absorption. The iron line energy and width and the column density were fixed at the pulse-phase average values.

peaked. For dataset 4 the pulse profile is less well-defined, comprising a broad, asymmetric peak.

6.4.2 The continuum spectrum

There are significant, systematic variations in the continuum spectrum with pulse phase. The shape of the continuum spectrum in these data may be explained satisfactorily by either a black body plus thermal bremsstrahlung or a Comptonization model. In the former case the black body may approximate the spectrum of radiation from the accretion column and the thermal bremsstrahlung component may be due to the extended stellar wind or possibly a shock above the neutron star's surface. The canonical cut-off power law does not fit the data well. The best-fitting model is a power law with a cyclotron scattering cut-off. This does not necessarily mean that a CSRF has been detected. The inferred cyclotron line energy is suspiciously close to the upper limit of the energy range used in fitting the spectra. This was also noted by Nagase et al. (1992). When the data are fitted to a power law with cyclotron absorption the apparent cyclotron energy varies with pulse phase. The variation of the cyclotron energy with pulse phase is determined by the structure of the accretion column. If most of the accretion takes place on the polar caps the luminosity of Cen X-3 can be close to the Eddington limit. Thus the accretion flow is dominated by radiation pressure. It is likely that the accreting matter is decelerated in a collisionless shock some distance above the surface of the neutron star. This would lead to a fan-beam emission pattern, with the pulse maximum occurring for viewing directions normal to the magnetic field. One would then expect the maximum depth of the cyclotron resonance to coincide with the pulse minimum.

The maxima of the cyclotron depth τ_{Cy} and the cyclotron energy E_{Cy} appear to coincide with a bump in the falling part of the pulse profile's main peak. We could thus interpret this third peak as the phase when we see both poles at 90° .

6.4.3 The Iron Line

The iron line has a finite physical width which is consistent with its identification as a blend of lines from neutral and highly ionized iron. The absence of a deep absorption edge at 7.1 keV indicates that the line is caused mainly by reflection of the continuum by a fluorescing medium.

One disturbing fact is that the pulse-phase average iron line width depends on the continuum model. This effect is most evident in Figure 6.3 where the iron line has an unphysical width due to the poor modelling of the continuum by the cut-off power law model. Nevertheless, the pulse-phase dependence of the iron line intensity appears to be consistent between different continuum models.

Chapter 7

Effects of Reflection — ASCA

7.1 Motivation

The results of Chapter 5 indicated that pulse and orbital phase-resolved spectroscopy of Cen X-3 outside of X-ray eclipse would be useful. Previous observations had shown that several Fe K lines were present; a 6.4 keV line emitted from a region within 1 lt-sec of the neutron star and lines at 6.7 and 6.9 keV probably emitted from over much of the binary system. At least one of the lines was modulated at the 4.8 sec pulse period, but it was not possible to tell which one. Using the SIS to observe from orbital phase 0.2–0.8 it might be possible to determine which lines are modulated and physically locate the sites of the X-ray emission components in a massive X-ray binary for the first time.

7.2 The Observation

Cen X-3 was observed outside of eclipse with ASCA from 1995 February 1 10:57 to 1995 February 2 20:47 UT. The observation covered orbital phases 0.1–0.8 where phase 0 refers to mid-eclipse. The gradual X-ray eclipse lasts from orbital

phase ~ 0.8 to ~ 0.2 . The SIS was operated in fast mode except for some short intervals in bright mode. These bright mode observations were necessary to determine the position of the source on the SIS CCDs since fast mode sacrifices spatial information in favor of better time resolution.

7.3 Results

7.3.1 Timing analysis

Barycentric corrections were applied to the GIS data and 34 folded pulse profiles were obtained. Pulse arrival time analysis was complicated by the variability of the pulse profile. Therefore each profile was fitted to a truncated Fourier cosine series and the pulse minimum found. The pulse minimum was then used as the fiducial phase in determining the pulse arrival times. The arrival times were fitted to a circular ephemeris of the form

$$t_n = t_0 + P_0 n + a_x \sin i \cos\left(\frac{2\pi(t_n - T_{ecl})}{P_{orb}}\right) \quad (7-1)$$

where P_0 is the inertial pulse period, $a_x \sin i$ is the projected semi-major axis of the pulsar's orbit, T_{ecl} is the epoch of mid-eclipse, and P_{orb} is the orbital period at the time of the observation. The derived orbital parameters are shown in table 7.1. Introduction of eccentricity (Kelley et al. 1983) or a non-zero \dot{P}_0 did not improve the fit. Once the ephemeris was determined the photon arrival times were corrected for the orbital motion of the pulsar.

Table 7.1. Orbital parameters from pulse arrival time analysis.

Parameter	Value
$a_x \sin i/c$	39.67 ± 0.08 s
P_0	4.815988 ± 0.000008 s
P_{orb}	2.091 ± 0.005 days
T_{ecl}	MJD 49749.189 \pm 0.002

Note. — Errors are for 90% confidence in one interesting parameter.

7.3.2 The Light Curve

The GIS light curve is shown in Figure 7.1. The intensity increases systematically through the observation except for a flare at orbital phase 0.4 during which the intensity increases by a factor of 2.5 and decays on a timescale of $(3.6 \pm 0.4) \times 10^3$ s. The flare is accompanied by a slight softening of the light curve, as shown in Figure 7.2. The general trend is for the hardness ratio to decrease as the intensity increases, indicating that the X-ray spectrum is luminosity dependent.

In the Fourier power spectrum of the pre-eclipse data there is a possible QPO. The centroid frequency is 47.4 ± 0.2 mHz (see Figure 7.3). There is also a possible but marginal QPO in the post-flare data (see Figure 7.4).

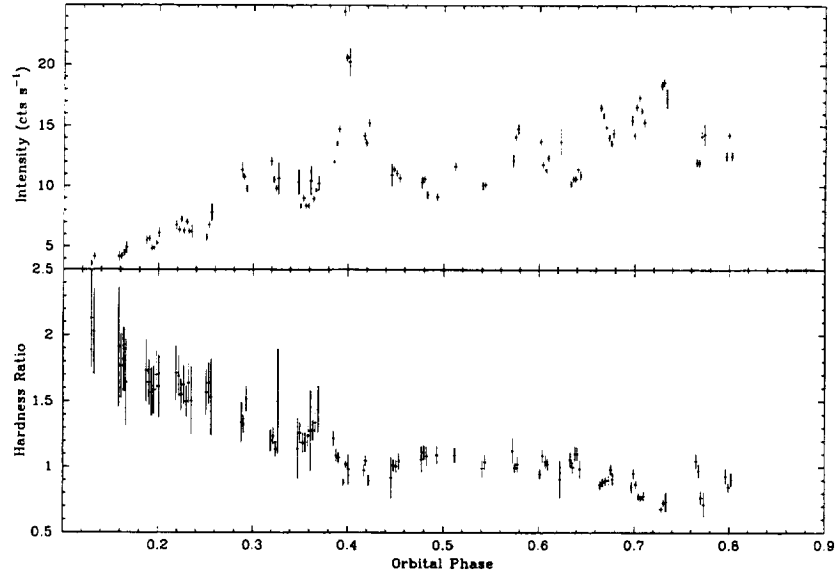


Fig. 7.1— Light curve and hardness (4.5–11 keV / 0.7–4.5 keV) plotted against orbital phase. Data from GIS2 and GIS3 have been combined. The gradual X-ray eclipse covers orbital phases ~ 0.8 – 0.2 .

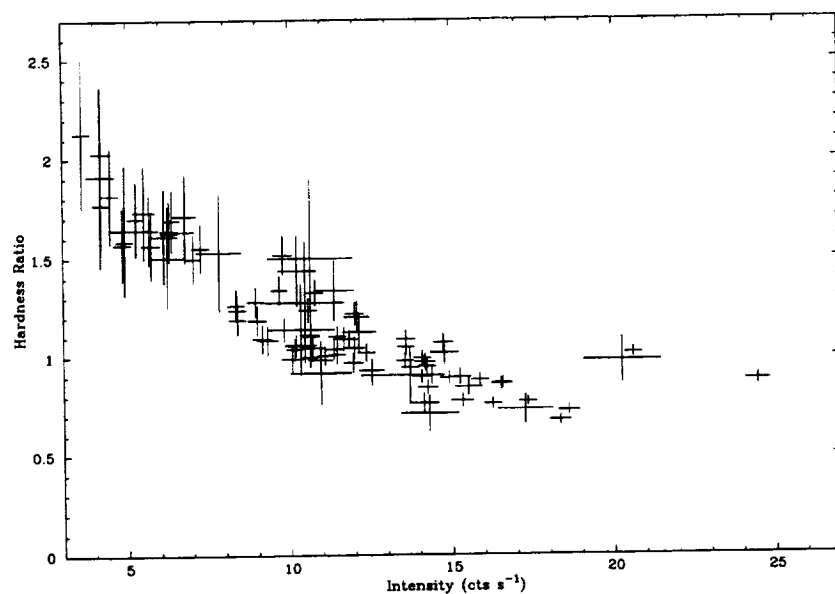


Fig. 7.2— Hardness plotted against intensity. Two distinct regions are evident. The points on the right hand side (intensity $\gtrsim 20$ cts s $^{-1}$) are due to the flare at orbital phase 0.4 where the intensity increases with little change in the hardness. In the left hand region the spectrum becomes softer as the intensity increases.

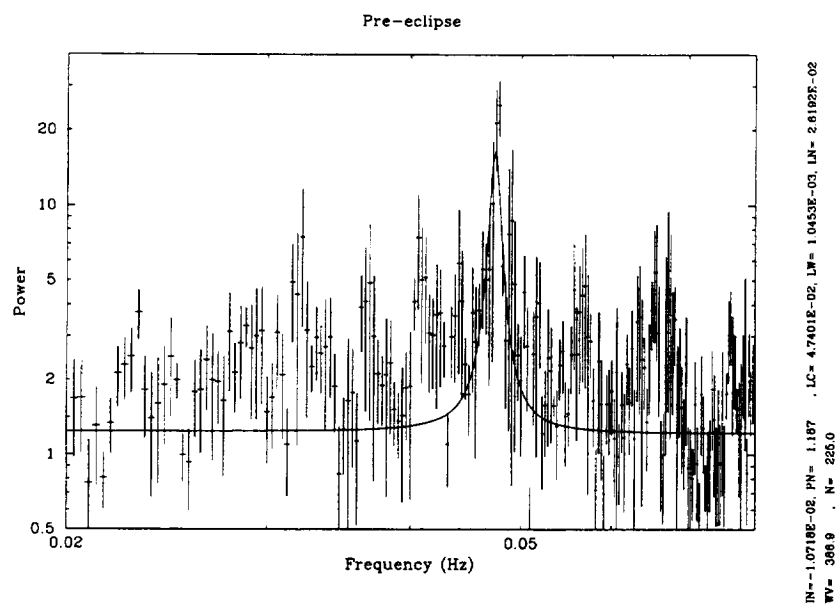


Fig. 7.3— Possible QPO in pre-eclipse data.

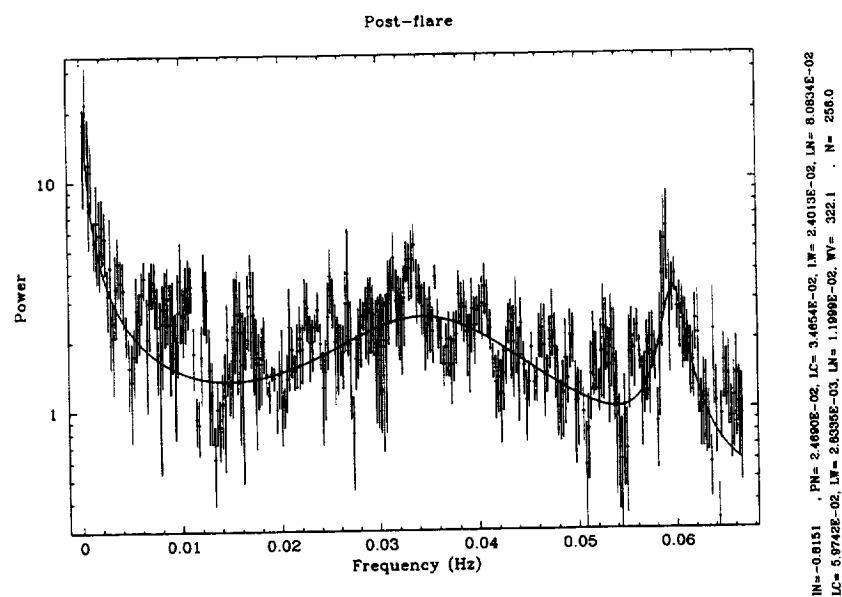


Fig. 7.4— Possible QPO in post-flare data.

7.3.3 The pulse profile

The average pulse profile consists of two peaks of similar size separated by $\sim 110^\circ$. Figure 7.5 shows the folded intensity and hardness profiles for different orbital phases. The factor of four change in the X-ray intensity through the observation is accompanied by significant changes in the pulse profile. The profile also has different energy dependence at different orbital phases.

7.3.4 Spectroscopy

Figure 7.6 shows the SIS1 fast mode spectrum of the iron line region. The continuum has been modeled with a power law and a broad Gaussian. This broad Gaussian may be due to Comptonization of the 6.4 keV iron line. In any case, a single power law continuum does not fit the data well. The iron emission complex is clearly resolved into three components — a 6.4 keV fluorescent line, a line at 6.7 keV due to emission by Fe XXV, and a line at 6.97 keV due to emission by Fe XXVI. The best-fit parameters are shown in Table 7.2. The average GIS spectrum is shown in Figure 7.7. A single power-law continuum did not give a satisfactory fit. The best-fit continuum model had the form

$$I(E) = e^{-\sigma EN_{H1}}(e^{-\sigma EN_{Hm}} I_m E^{-\alpha} + e^{-\sigma EN_{Hh}} I_h E^{-\alpha} + I_s E^{-(\alpha+2)}) \quad (7-2)$$

where the interstellar column density, N_{H1} , was fixed at $1.3 \times 10^{22} \text{ cm}^{-2}$. The first power law component represents direct emission from the neutron star, the second may be due to reflection from cold matter near the neutron star, and is constrained to have the same photon index. Figure 7.8 shows how this reflected component may arise. The third component models interstellar dust scattering and its energy dependence is constrained to be softened by a factor of E^{-2} relative

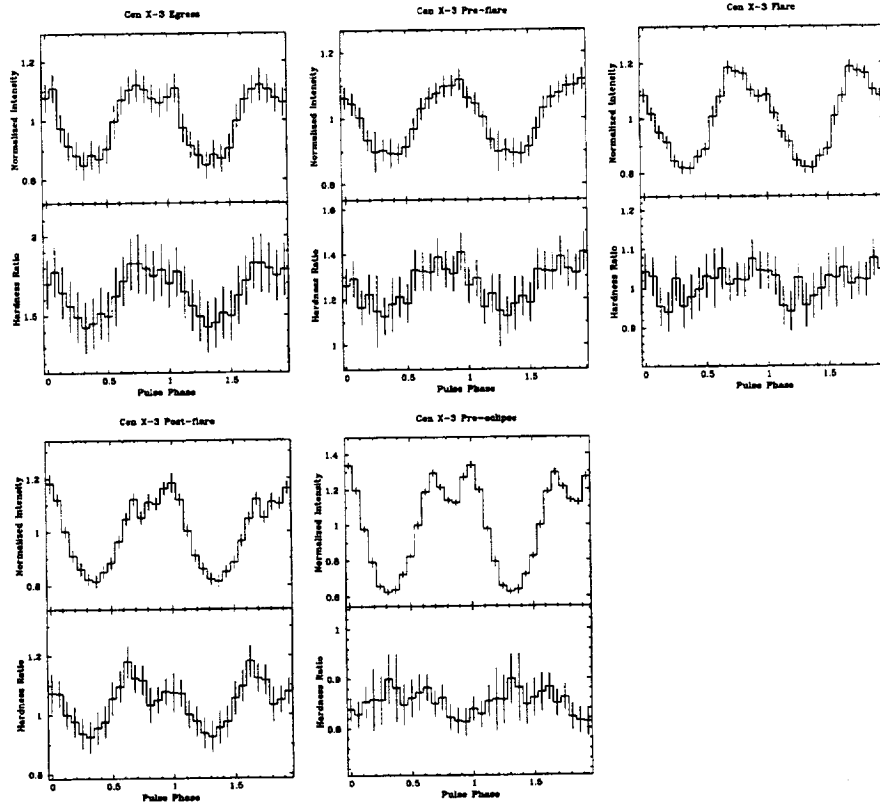


Fig. 7.5— Orbital phase resolved GIS pulse profiles and hardness ratios. The upper panel is the 0.7–11 keV intensity divided by the pulse-phase average. The lower panel is the ratio of the 0.7–4.5 keV count rate to the 4.5–11 keV count rate.

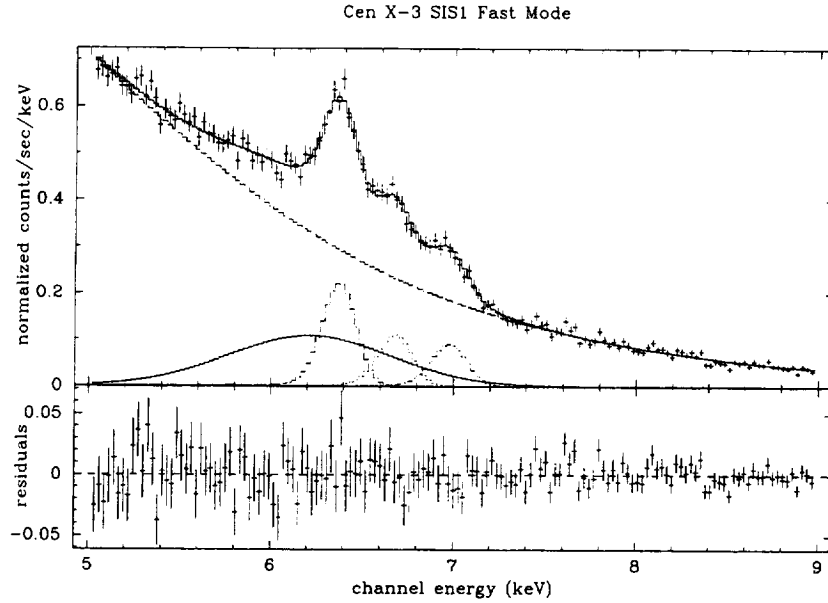


Fig. 7.6— SIS1 fast mode spectrum of iron line region showing resolved emission lines at 6.4, 6.7, and 6.9 keV.

to the direct component. This assumes that the Rayleigh-Gans approximation for the differential scattering cross-section holds. Below 2 keV the exact Mie solution for scattering of X-rays by interstellar dust grains is more appropriate. However, due to the fact that the observed intensity falls off quickly below 2 keV it is assumed that the simpler Rayleigh-Gans approximation holds even though it overestimates the scattering intensity (Smith and Dweck 1998).

This model gave a significantly better fit to the observation-averaged spectrum than the model of Ebisawa et al. (1996) in which α was fixed at 1.0.

It is convenient to refer to the three continuum components as the medium, hard, and soft components, respectively, and identify them with the subscripts m , h , and s . To the medium component were added narrow lines at 1.85, 2.01, and

Table 7.2. Observation-average best fit parameters from SIS1 data.

Parameter		Value
α	Photon Index	0.68 ± 0.02
$I_{\text{P.L.}}^{\text{a}}$		0.0406 ± 0.0004
E_1^{b}	Fe I	6.377 ± 0.009
I_1^{c}		21 ± 1
E_2^{b}	Fe XXV	6.68 ± 0.02
I_2^{c}		13 ± 1
E_3^{b}	Fe XXVI	6.97 ± 0.01
I_3^{c}		13 ± 1
$E_{\text{broad}}^{\text{b}}$	Comptonized iron line?	6.33 ± 0.03
σ_{broad}	Gaussian width in keV	0.44 ± 0.03
$I_{\text{broad}}^{\text{c}}$		47 ± 2

^aPower law intensity in $\text{cts keV}^{-1} \text{cm}^{-2} \text{s}^{-1}$ at 1 keV

^bGaussian emission line centroid energy in keV

^cLine intensity in $10^{-4} \text{cts cm}^{-2} \text{s}^{-1}$

Note. — Errors are for 90% confidence in one interesting parameter. The energy range has been restricted to 5–9 keV for spectral fitting.

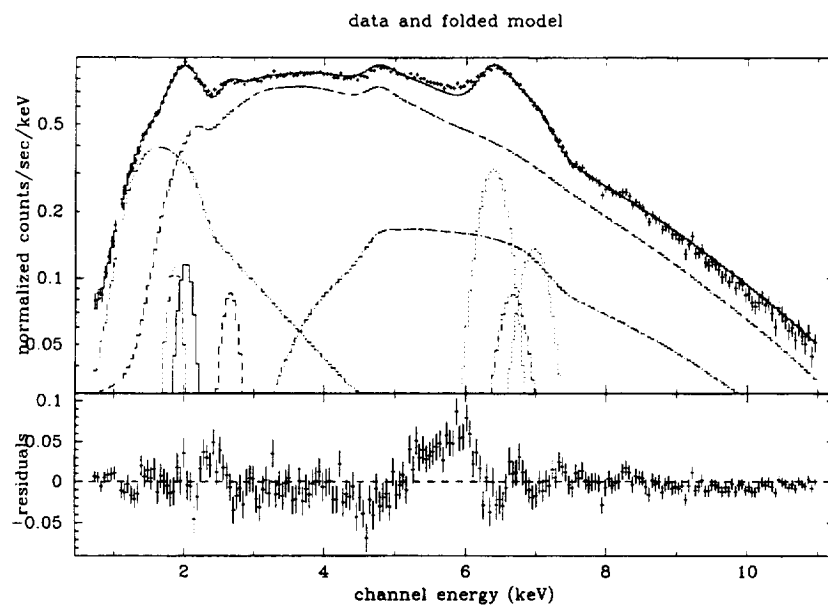


Fig. 7.7— Observation-average GIS spectrum. The iron line region is fitted with three narrow lines at 6.4, 6.67, and 6.97 keV.

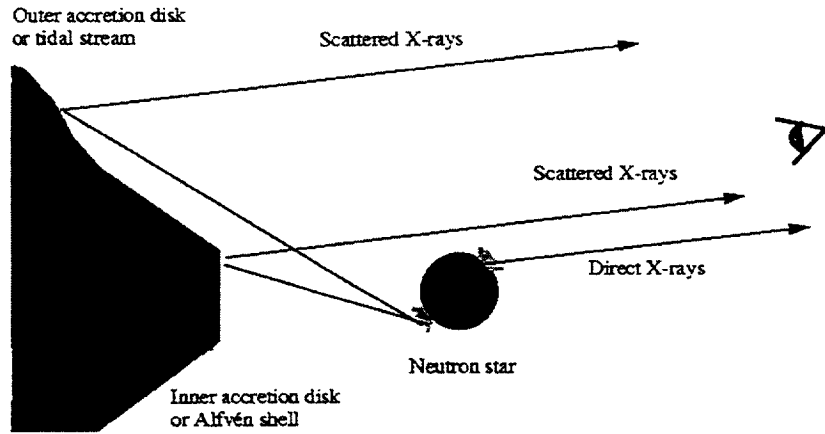


Fig. 7.8— Possible origin of a reflected component in the X-ray spectrum (not to scale). The observer sees direct emission from one polar cap and scattered X-rays from material that is backlit by the other polar cap.

2.64 keV, corresponding to emission from Si XII, Si XIV, and S XVI, respectively. To the hard component was added a 6.4 keV narrow line with centroid energy 6.4 keV. This is due to fluorescence of iron in low ionization stages. This fit yielded an unacceptably high χ^2_ν . The poor fit is due to the presence of residuals around 6 keV. Allowing the 6.4 keV line to have a finite width improved the fit but it was still unacceptable. When a broad Gaussian with centroid energy ~ 6.3 keV was added to the hard component an acceptable fit was obtained as shown in Figure 7.9. This component may be due to Comptonization of the 6.4 keV iron line. The best fit spectral parameters are shown in Table 7.3.

In order to examine the iron line equivalent widths the GIS data were fitted with the energy range restricted to 5–8 keV. The continuum model was a power law with iron K-edge absorption. The iron line complex was modeled by three narrow lines with centroid energies fixed at 6.4, 6.67, and 6.97 keV. This model

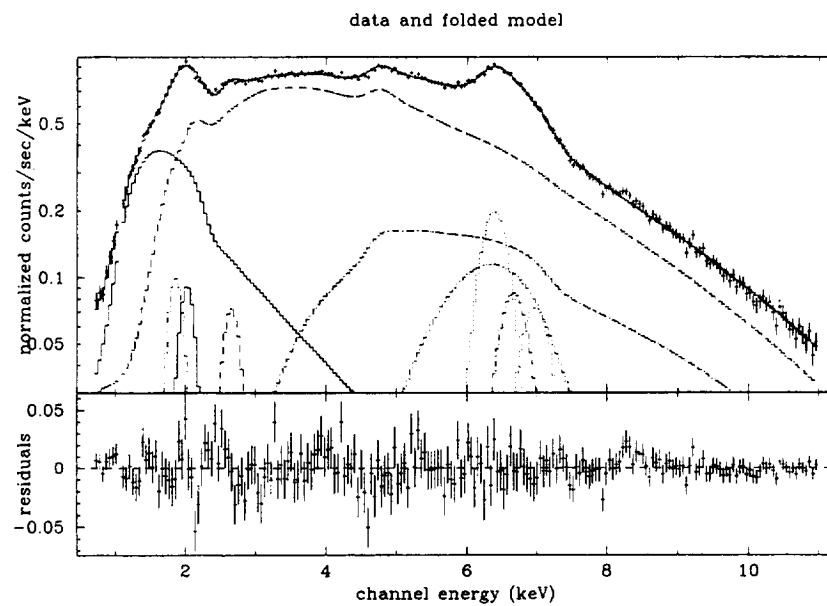


Fig. 7.9— Observation-average GIS spectrum. The model is the same as that in Figure 7.7 but with a broad Gaussian at 6.36 keV

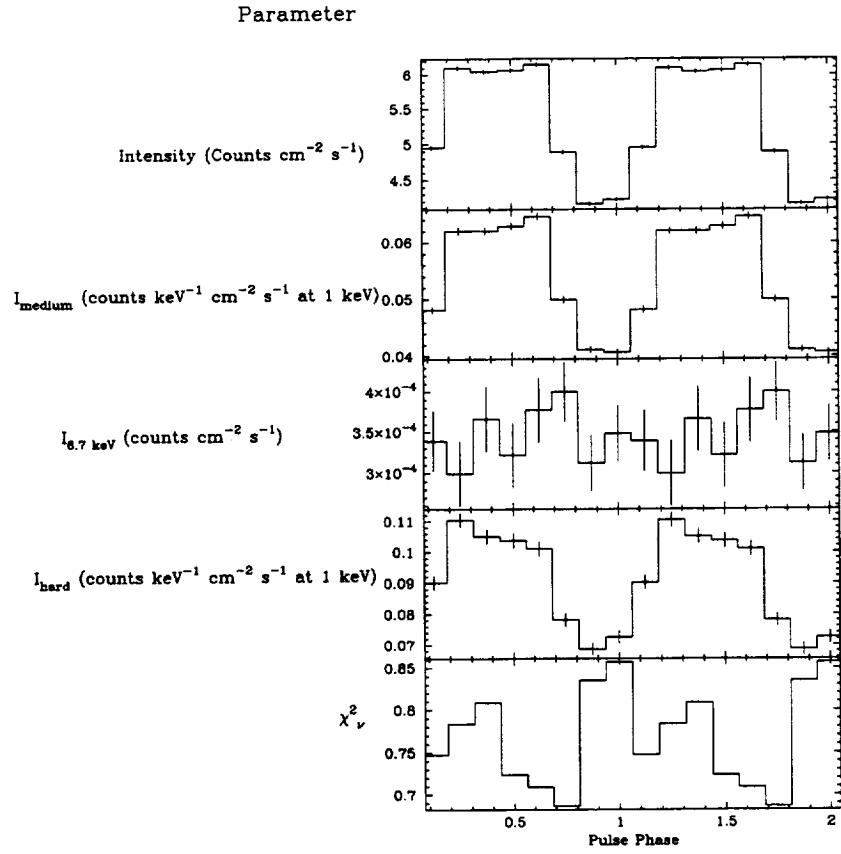


Fig. 7.10— Variation of spectral parameters with pulse phase.

Table 7.3. Observation-average best fit parameters from GIS data.

Parameter		Value
α	Photon Index	1.29 ± 0.13
$I_{\text{medium}}^{\text{a}}$		0.0354 ± 0.0067
$I_{6.67}^{\text{b}}$	Fe XXV	3.79 ± 0.78
$I_{6.97}^{\text{b}}$	Fe XXVI	3.6 ± 0.9
$I_{1.85}^{\text{b}}$	Si XII	14.8 ± 4.0
$I_{2.01}^{\text{b}}$	Si XIV	8.9 ± 2.6
$I_{2.64}^{\text{b}}$	S XVI	4.13 ± 0.97
$N_{H\text{medium}}$	$(10^{22} \text{ cm}^{-2})$	3.25 ± 0.24
$I_{\text{hard}}^{\text{a}}$		0.0219 ± 0.0035
$I_{6.4}^{\text{b}}$	Fe I	12 ± 2
E_{broad}	Gaussian centroid energy in keV	6.34 ± 0.11
$\sigma_{\text{broad}}^{\text{b}}$	Gaussian width in keV	0.78 ± 0.12
$I_{\text{broad}}^{\text{b}}$		28.2 ± 5.7
$N_{H\text{hard}}$	$(10^{22} \text{ cm}^{-2})$	25.1 ± 5.6
$I_{\text{soft}}^{\text{a}}$		0.027 ± 0.001

^aPower law intensity in $\text{cts keV}^{-1} \text{ cm}^{-2} \text{ s}^{-1}$ at 1 keV

^bLine intensity in $10^{-4} \text{ cts cm}^{-2} \text{ s}^{-1}$

Note. — Errors are for 90% confidence in one interesting parameter.

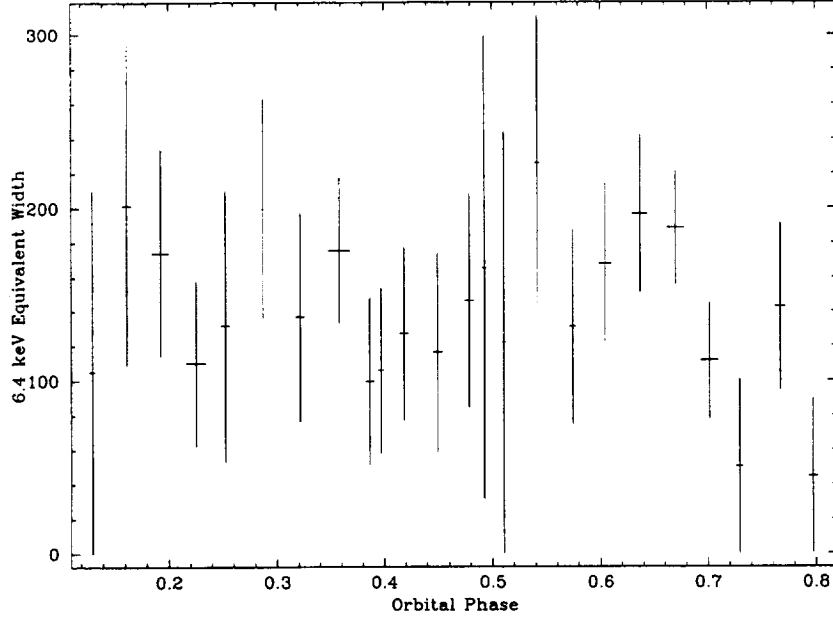


Fig. 7.11— Variation of fluorescent iron line equivalent width with orbital phase. Errors are for 90% in one interesting parameter.

fitted a spectrum extracted from all the GIS high bitrate data well. Pulse-phase averaged spectra were extracted from 24 time intervals. The edge energy and the power law index were fixed at the observation-average value. This yielded acceptable fits to the 24 spectra. The 6.4 keV iron line equivalent width is plotted versus orbital phase in Figure 7.11.

Because of the limitations of counting statistics, pulse-phase resolved spectroscopy of these 24 intervals was not feasible. Thus, the observation was divided into five intervals. These are denoted “eclipse egress”, “pre-flare non-eclipse”, “flare”, “post-flare non-eclipse”, and “pre-eclipse” phases. The corresponding orbital phase intervals were $\phi = 0.12 - 0.26$, $\phi = 0.18 - 0.38$, $\phi = 0.38 - 0.42$,

$\phi = 0.44 - 0.64$, and $\phi = 0.66 - 0.8$, respectively. These spectra were fitted to the continuum model of equation 7-2. The three iron lines were included in the fit. The 6.36 keV broad feature was not required. However, allowing the 6.4 keV line's width to vary improved the fit. The ratio of the 6.4 keV line to the hard power power law intensity and the ratio of the 6.67 and 6.97 keV recombination lines were fixed. Also, α was fixed at the observation-average value. Clear variations in the continuum spectra are apparent in figures 7.12 and 7.13.

7.4 Discussion

7.4.1 The pulse profile

The pulse profile of Cen X-3 has been observed as an asymmetric single peak in the high state (e.g. Audley et al. 1996, , see Chapter 5) and a double peaked structure in the low state (e.g. Nagase et al. 1992).

The mean unabsorbed 2–10 keV luminosity during the present observation was 5×10^{36} erg s⁻¹, while it was 3.29×10^{37} erg s⁻¹ during the BBXRT observation when the profile had a single asymmetric peak (Audley et al. 1996). The pulse profile varies during the present observation, becoming less double-peaked during the “flare” at $\phi = 0.4$. Another trend which is evident from figure 7.5 is that the two peaks in the profile appear to swap places as the intensity increases. Before the “flare” the peak which follows the pulse minimum dominates. After the “flare” the peak which precedes the minimum is more prominent. During the “flare” itself this latter peak is less significant and the pulse profile is in effect an asymmetric single peak, as often seen in Cen X-3’s high state.

This indicates that the observed differences in the pulse profile of Cen X-

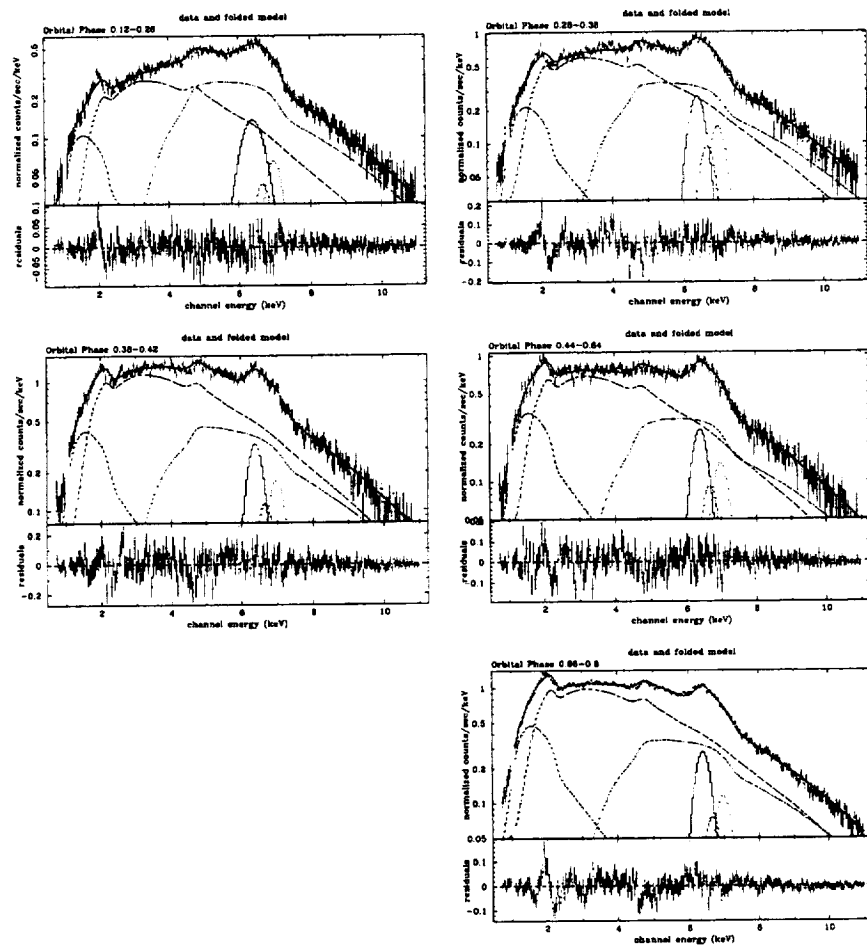


Fig. 7.12— Pulse-phase averaged spectra at different orbital phases.

Orbital Dependence of Spectral Parameters

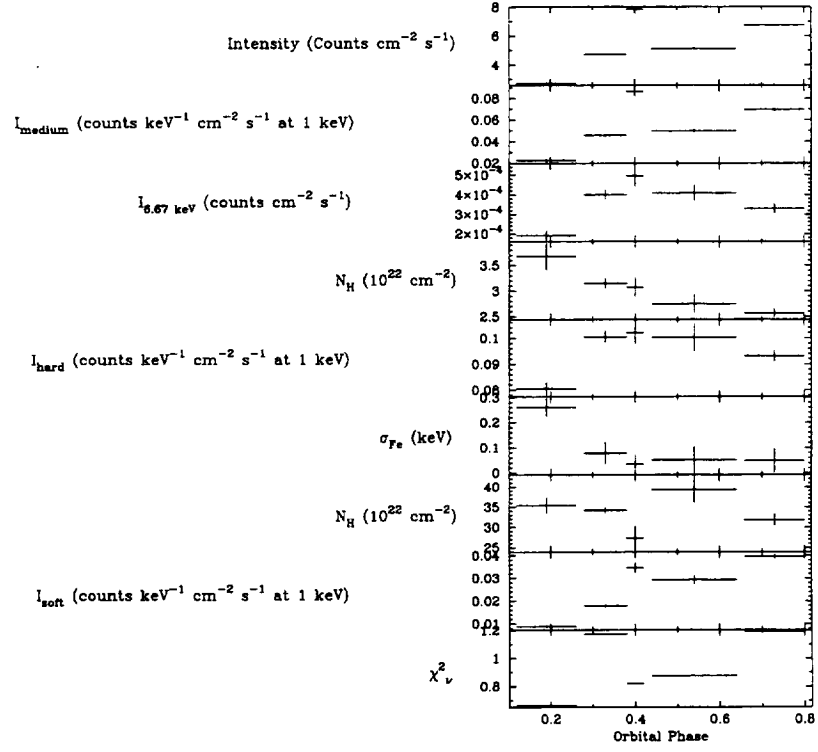


Fig. 7.13— Orbital dependence of spectral parameters.

3 may be due to luminosity induced changes in the structure of the accretion column as observed in EXO 2030+375 (Parmar et al. 1989).

7.4.2 The X-Ray Spectrum

The Continuum

Mihara (1995) successfully modeled the spectra of several X-ray binaries with a continuum of the form $I(E^{-\alpha_1} + E^{\alpha_2}) \exp(-\frac{E}{kT})$ where α_2 was fixed at the value 2. The first term represents the usual power law which is dominant below 10 keV and the second term has the form of blackbody radiation. However Mihara could not obtain a good fit to the Ginga data on Cen X-3 with a continuum model of this form. The fit could be improved either by allowing α_2 to vary or by including a CSRF with $E_0 \sim 40$ keV. When this model was fitted to the observation-averaged GIS spectrum the fit was significantly worse than that obtained with the three component continuum model. In this case also, there were residuals around 6 keV. This indicates that these features may be associated with the 6.4 keV fluorescent iron line rather than deficiencies in the continuum model.

The pulse-phase dependence of the intensities of the medium- and high-energy power law components is shown in figure 7.14.

The three component continuum can explain the changes in the X-ray spectrum. I interpret these changes as being due to a gradual “switching on” of the source. As the X-ray luminosity increases, so does the X-ray excited wind. Thus the strength of the medium component which is probably due to direct emission from the neutron star increases through the observation.

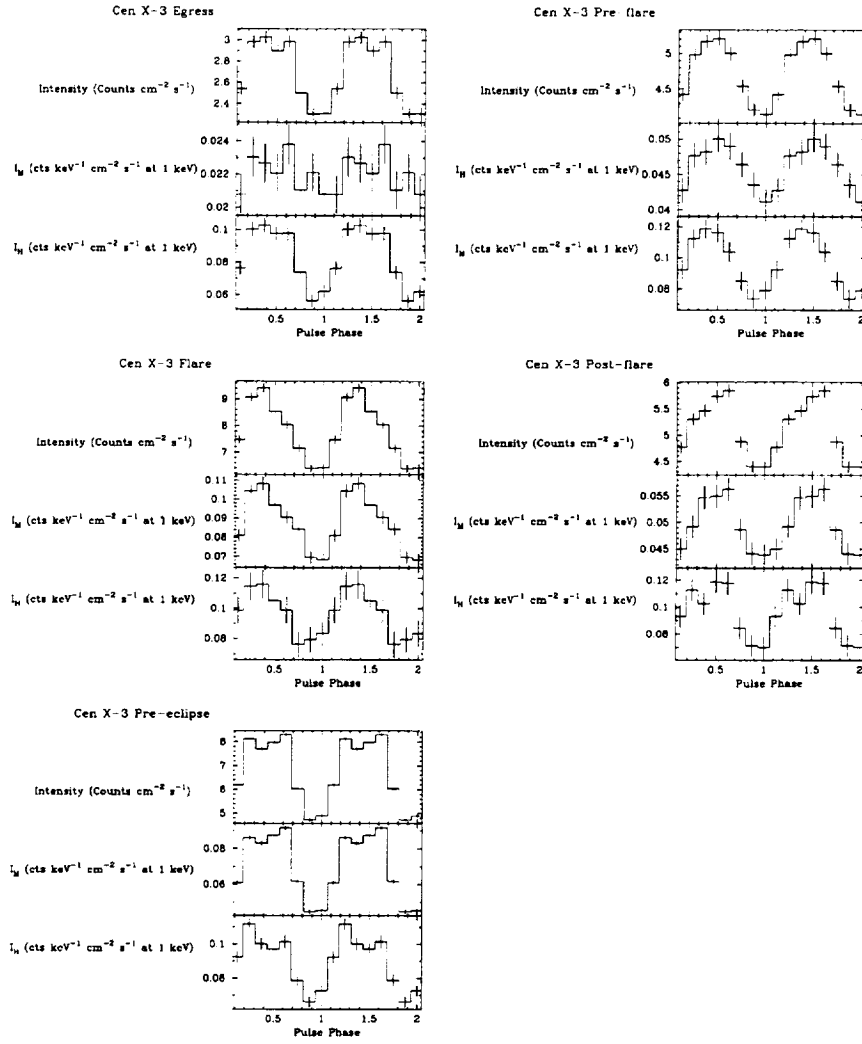


Fig. 7.14— Variation of hard and medium component power law intensities with pulse phase.

The Iron Line

While there is evidence for Comptonization of the iron line in the observation-averaged spectrum, it is not readily apparent in the pulse- and orbital-phase resolved spectra due to the limitations of counting statistics.

The maximum energy change of a photon of energy E_0 undergoing one Compton scattering is

$$\Delta E = \frac{E_0}{1 + \frac{m_e c^2}{2E_0}} \quad (7-3)$$

which is 0.16 keV for $E_0 = 6.4$ keV. This assumes that the electron's kinetic energy is much smaller than the photon energy. Thus the centroid energy of the broad Gaussian feature (6.34 ± 0.11 keV) is consistent with scattering by cold electrons with a single scattering event per reflected photon, on average. The large width (708 ± 120 eV) must also be explained. Assuming that the He to H ratio is 0.1 the optical depth for scattering is

$$\tau_s = 1.2 \sigma_T N_H \quad (7-4)$$

where $\sigma_T = 6.65 \times 10^{25} \text{ cm}^{-2}$ is the Thompson cross section. With a column density $N_H \approx 2.5 \times 10^{23} \text{ cm}^{-2}$, as obtained from the observation-average spectrum, the optical depth will be ~ 0.2 so that Comptonization of the iron line will have some effect on its profile (e.g. George and Fabian 1991; Yaqoob 1997). If the broad 6.36 keV feature originates near the magnetosphere the high rotation velocities ($\sim 5000 \text{ kms}^{-1}$) would contribute to the observed width through Doppler broadening.

The pulse-phase averaged equivalent width of the 6.4 keV line is approximately 140 eV and does not vary much over the observation. As Day et al. (1993) pointed out, an equivalent width this high is more consistent with reflec-

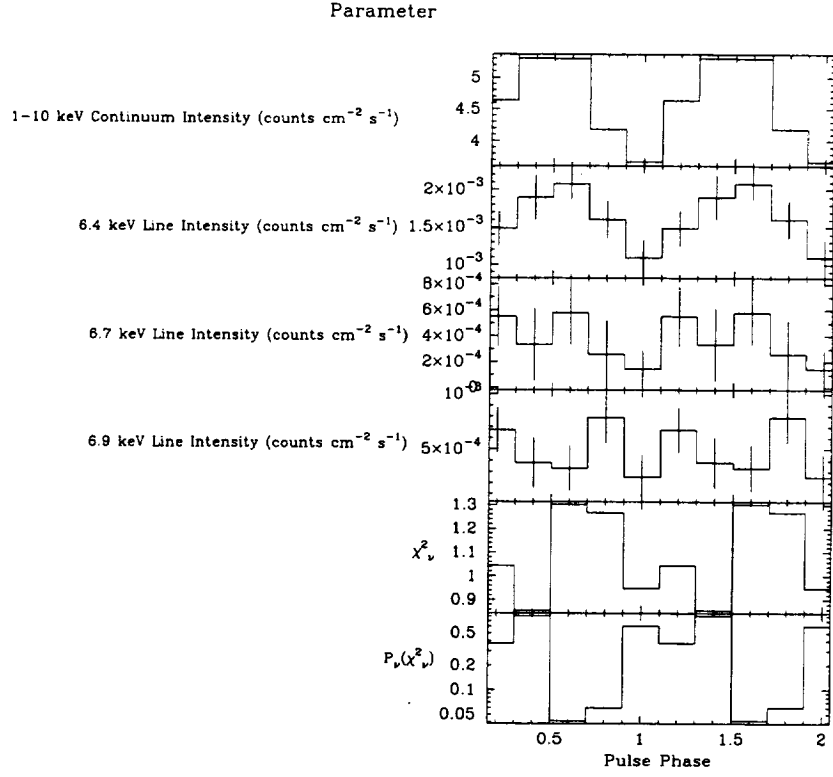


Fig. 7.15— Variation of iron line intensities with pulse phase.

tion than fluorescence in material surrounding the source because it does not require such a high column density (Makishima 1986).

The pulse-phase dependence of the iron lines is shown in figure 7.15. The 6.4 keV line is pulsing with an amplitude of about 50% while the 6.7 and 6.9 keV lines are constant. This supports the model where the 6.4 keV line is due to fluorescence of matter near the neutron star and the 6.7 and 6.9 keV recombination lines are generated in the extended ionized stellar wind.

7.4.3 Pulsar Geometry

The swapping of the two peaks in the pulse profile could be a geometrical effect. As the pulsar orbits the companion one magnetic pole comes into view while the other is obscured and is seen in reflection (medium component). However it is clear that there are at least two components required to describe the spectrum.

The “flare” might be due to the pulsar encountering a region of enhanced density in the stellar wind, causing an increase in the mass accretion rate. However the short duration of the “flare” requires that this accretion occurs directly to the pulsar and not through the accretion disk. This is due to the small radial drift velocities expected in the thin, optically thick disk model of Shakura and Sunyaev (1973, see Figure 4.4). An increase in the mass accretion rate feeding the disk would be expected to be smeared out over a timescale of days. Another possibility is an enhancement in the rate of thermonuclear burning on the surface. While the instabilities that cause type I X-ray bursts on non-magnetic neutron stars are ruled out by Cen X-3’s strong magnetic field (e.g. Lewin et al. 1995), it might be possible for unstable carbon burning to cause a flare lasting minutes to hours (Bildsten 1995, 1997; Bildsten and Brown 1997). However, given the much lower efficiency of thermonuclear fusion, the “flare” is easier to explain as an increase in the mass accretion rate.

The most likely explanation is that the “flare” is due to an impulsive increase in the accretion rate caused by a clump of matter in the inner accretion disk. The existence of such a clump might be expected to be accompanied by a QPO if the beat frequency mass accretion model is correct. QPOs are detected in the pre-eclipse data and, with marginal confidence, in the post-flare data. In the pre-eclipse data the QPO’s centroid frequency is 47.4 ± 0.2 mHz and its width is

1.3 ± 0.9 mHz. In the case of the post-flare data there is a possible feature around 60 mHz and a knee at ~ 34 mHz. QPOs with frequencies above around 40 mHz have not been seen in Cen X-3 before. The QPO frequency during the BBXRT observation was 40.7 ± 1.1 mHz. The BBXRT unabsorbed luminosity was 3.29×10^{37} erg s $^{-1}$ in the 2–10 keV band, while the mean luminosity during the ASCA observation was 5×10^{36} erg s $^{-1}$. As the luminosity, and hence the mass accretion rate, decrease the Keplerian rotation frequency at the magnetosphere $\Omega_K(r_A)$ should also decrease. One then expects the QPO frequency ($\omega = \Omega_K(r_A) - \Omega_0$ if $\Omega_K(r_A) > \Omega_0$) to decrease. If the possible QPOs seen in the ASCA data are real, they would imply that the QPO frequency has increased with a decrease in luminosity. There are several ways this could happen. If $\Omega_K(r_A) < \Omega_0$, the QPO frequency will be $\omega = \Omega_0 - \Omega_K(r_A)$. However, the centrifugal barrier would tend to inhibit accretion through the propeller effect and switch off the source. Another possibility is that the QPOs are harmonics of the fundamental beat frequency. It is also possible that these features are produced by some mechanism other than the beat frequency mass accretion model.

7.5 Conclusions

The spectrum appears to be modified by a component due to reflection by cold matter near the neutron star, probably the accretion disk. There are luminosity-induced variations in the pulse profile. It appears that this observation caught the source in the act of turning on (Day and Stevens 1993).

Chapter 8

Cyclotron Line — RXTE

8.1 Motivation

Makishima et al. (1992) describe cyclotron scattering resonance features (CSRF) in nine X-ray binary pulsars. The discovery of seven of these was made possible by the improved energy resolution and effective area of the Ginga LAC (Makino and the ASTRO-C Team 1987). A 110 keV CSRF has also been observed in the spectrum of the transient X-ray binary pulsar A 0535+262 (Kendziorra et al. 1994; Grove et al. 1995). Even if this is the first harmonic of a less significant feature at ~ 55 keV the magnetic field ($\sim 4.5 \times 10^{12}$ G) is higher than any other derived for an accreting neutron star by CSRF observations. Detection of this feature was made possible by the high energy response of the TTM and HEXE instruments on board the Mir space station and the OSSE instrument on board the Compton Gamma Ray Observatory. It was expected that the large effective area, energy resolution, and high energy response of the RXTE PCA and HEXTE detectors combined would similarly increase the number of observed CSRF in accreting neutron stars from the ten detected so far.

Direct measurements of the magnetic fields of X-ray binaries are important

because they provide information on the evolution of the systems. Additional measurements of pulsar magnetic fields are required to determine if these fields decay. A measurement of the field of the relatively young pulsar Cen X-3 would help settle the question of neutron star field decay and a CSRF observation is the only method which can make this measurement directly from X-ray observations. A direct measurement of the magnetic field from a CSRF would also place constraints on the parameters of the neutron star and the structure of the accretion column. The width of the CSRF would provide a measure of the spatial extent of the accretion column.

Mihara (1995) successfully modeled the spectra of several X-ray binaries with a continuum of the form $I(E^{-\alpha_1} + E^{\alpha_2}) \exp(-\frac{E}{kT})$ where α_2 was fixed at the value 2. The first term represents the usual power law which is dominant below 10 keV and the second term has the form of blackbody radiation. This composite model approximates an unsaturated Comptonized spectrum. However he could not obtain a good fit to the Ginga data on Cen X-3 with a continuum model of this form. The fit could be improved either by allowing α_2 to vary or by including a CSRF with $E_{Cy} \sim 40$ keV. In any case it was clear that, whatever the choice of continuum model, there are unexplained features in the spectrum in Cen X-3 cannot be described well by a simple exponential cut-off. In the OSO 8 spectra of Cen X-3 there was an apparent flattening of the spectrum at the pulse maximum (White et al. 1983). It is possible that this was due to variations in cyclotron absorption.

There had been no direct observation of a CSRF in the spectrum of Cen X-3 apart from the tentative detections at 30 keV with Ginga (Nagase et al. 1992) and at $\gtrsim 20$ keV in the EXOSAT GSPC data (see Chapter 6). In each case the

cyclotron line energy is suspiciously close to the upper limit of the detector's bandpass. Nevertheless, there are other reasons to believe that a CSRF may be present at that energy. In Chapter 5 I used the beat frequency mass accretion model (Shibazaki and Lamb 1987, and references therein) to explain the 40 mHz QPO in the BBXRT observation of Cen X-3 and derived a surface magnetic field of $\sim 2.6 \times 10^{12}$ G. I thus predicted that the observer frame energy of the associated CSRF would be ~ 29 keV. For a luminous source such as Cen X-3 it is expected that there will be a stand-off radiative shock above the neutron star's surface (Wang and Frank 1981) so that the magnetic field at the emission region will be smaller. Thus this value is an upper limit to the expected fundamental cyclotron resonance energy. There is thus reason to believe that Cen X-3 has a stronger magnetic field than the average ($\sim 1\text{--}2 \times 10^{12}$ G), placing a CSRF near the upper end of the Ginga LAC's 1–37 keV energy range. This, coupled with a possible broadening of the feature to ~ 20 keV due to a column accretion geometry, may explain why a CSRF has not been detected in Cen X-3 before. Makishima et al. (1992) found a proportionality between the cyclotron feature energy E_{Cy} and the cut off energy E_c derived from a model in which the high energy roll off is due to an exponential cut off. This suggests that the high energy roll off is due mainly to cyclotron opacity.

Using the relation $E_{Cy} \approx 2E_c$ of Makishima et al. we can estimate the magnetic fields of pulsars in which cyclotron lines have not been detected and thus predict where the cyclotron lines might be found. The apparent cut off energy E_c for Cen X-3 was found to vary with luminosity between 8 and 11 keV (White et al. 1983, see Chapter 6), suggesting $E_{Cy} \sim 2E_c \sim 16\text{--}22$ keV. However, the luminosity dependence of E_c suggests that parameters of the neutron

star atmosphere such as temperature and optical depth have some effect on the apparent cut off energy. Thus these values of E_c may not be inconsistent with $E_{Cy} \sim 20\text{--}30$ keV.

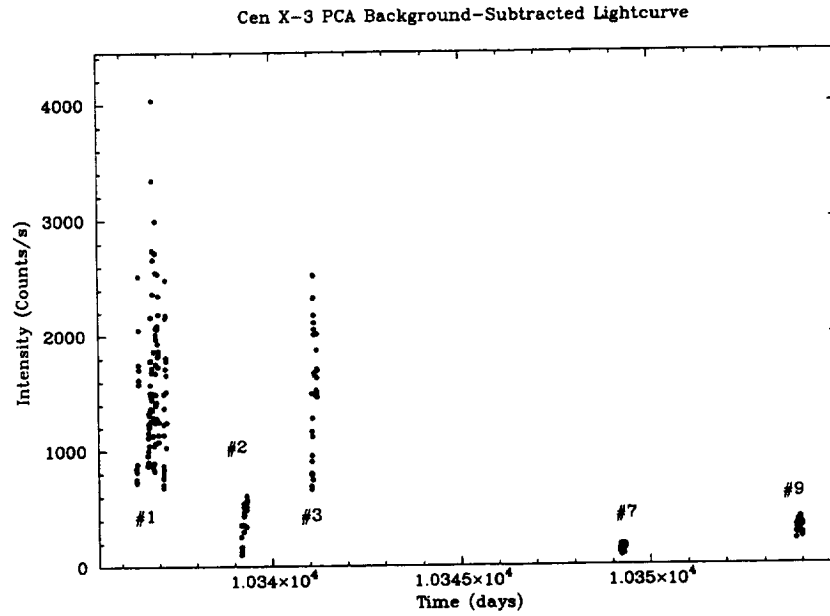
Although Nagase et al. were able successfully to model the cut-off in the Ginga data with cyclotron scattering, the available bandpass did not allow them to detect the upturn in the spectrum that would be present if there is in fact a cyclotron absorption feature at 30 keV. The situation was worse with the EXOSAT GSPC. It seemed that the RXTE PCA and HEXTE in combination would be well suited to examine the 30–60 keV region. Detection of this upturn would confirm that cyclotron opacity is largely responsible for the cut-off.

8.2 The Observation

Because Cen X-3 alternates between its high state and extended lows this observation was triggered from the ASM. The triggering intensity was 120 mCrab.

8.2.1 Background subtraction

To investigate the effect of the galactic ridge on the HEXTE spectrum we assumed a thin thermal bremsstrahlung spectrum with $kT = 7$ keV and a 2–11 keV flux of 8×10^{-8} erg cm $^{-2}$ s $^{-1}$ sr $^{-1}$ (Koyama 1989). We represented the hard tail component by a power law with photon index -2.65 (Gehrels and Tueller 1993) and assumed a flux at 100 keV of 4.5×10^{-7} photons cm $^{-2}$ s $^{-1}$ keV $^{-1}$ in HEXTE's field of view. Due to the brightness of Cen X-3 and the fact that the galactic ridge spectrum falls off much faster with energy, emission from the galactic ridge does not significantly affect the data. The HEXTE background spectra are ac-



The 2.1 day binary orbits are numbered in sequence

Fig. 8.1— Light curve of the observations accumulated in 256 s intervals.

cumulated by dwelling on blank sky fields on either side of the source. These were checked to make sure they agreed. Any difference would have indicated the presence of an X-ray source in one of the background fields. Because of uncertainties in the deadtime corrections and collimator response the normalization of the HEXTE background was varied until the count rate between 200 and 250 keV was zero. This renormalization of the background was not required by the PCA data from orbit #1 due to the high source count rate.

The light curve of the observations is shown in Figure 8.1. Each point is accumulated on a 256 s interval. There is considerable short-term variability. The source appears to have made a transition from its high to its low state.

8.3 Results

8.3.1 The Pulse Profile

The pulse shape is variable. It has the usual asymmetric single peak during orbit #1 when the source is in its high state (see Chapter 5). There is also a less prominent subsidiary peak which is separated from the main peak by about 180° . The subsidiary peak has a softer spectrum than the main peak. The 5–8 keV flux is strongly correlated with the subsidiary peak but not with the main peak. This is true for all of the pointings. If we regard the 6.4 keV fluorescent line as a tracer of X-ray reflection this means that the subsidiary peak contains a component due to reflection of X-rays by matter within a few light-seconds of the pulsar while the main peak is mainly due to emission from one of the pulsar's magnetic poles. As the luminosity decreases we see the profile become more double-peaked, resembling the structure observed by Nagase et al. (1992). The pulse profile also becomes complex, with several subsidiary peaks appearing between orbit #2 and orbit #3. The main and subsidiary peaks also appear to have change places in orbit #9. Typical pulse profiles from different pointings are shown in Figure 8.2.

This behavior is similar to that observed in EXO 2030+375 (Parmar et al. 1989). Parmar et al. attributed this luminosity dependence of the pulse profile to intensity dependent changes in the structure of the accretion column. They suggested that as the intensity decreased the beaming pattern changed from a fan beam with emission normal to the magnetic field to a pencil beam with emission along the magnetic field.

This may be understood in terms of a model in which infalling matter is

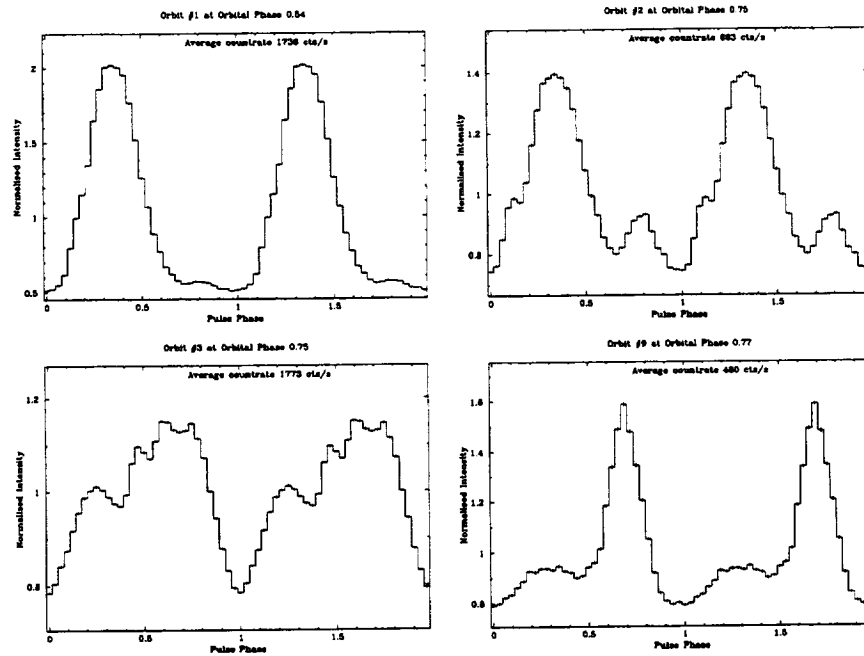


Fig. 8.2— Typical pulse profiles from the different binary orbits.

decelerated in a shock above the neutron star's surface. The height of this shock increases with luminosity resulting in a narrow column atmosphere for high luminosities. This column radiates from its sides in a fan beam pattern (see Figure 1.8). At lower luminosities accreting matter is decelerated close to the neutron star and the atmosphere is a thin slab which radiates predominantly along the magnetic field giving rise to a pencil beam emission pattern (see Figure 1.9).

8.3.2 Spectroscopy

Fits to the PCA data are complicated by severe systematic features in the response. These have been noted by others (e.g. Allen et al. 1997). Figure 8.3

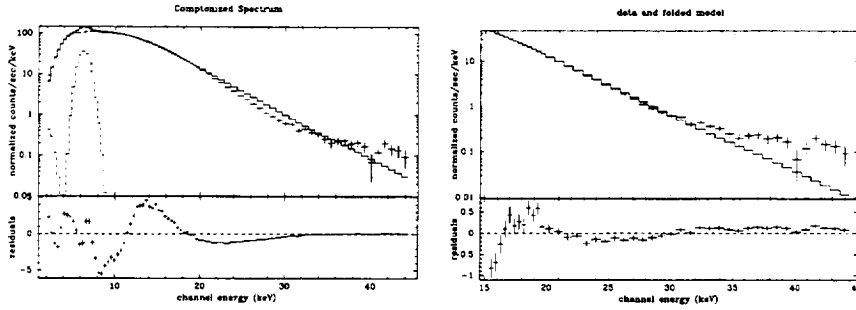


Fig. 8.3— Left: PCA spectrum from orbit #1 fitted to a Comptonization model and showing systematic features below 15 keV. Right: the same spectrum re-fitted above 15 keV.

shows the PCA data from orbit #1 covering orbital phase 0.34–0.38. The data have been fitted to a Sunyaev-Titarchuk Comptonization model with interstellar absorption and an iron line. As I mentioned in Section 6.3.2, although this model may not be appropriate to the physical conditions in Cen X-3, the fact that it fits the data well justifies its use. Also, it has no sharp features that might be misinterpreted as evidence for a CSRF. The fit is dominated by the systematic errors below 15 keV and has $\chi^2_\nu = 87$ with 73 degrees of freedom. Now if the 2–15 keV energy range is ignored and the spectrum is re-fitted, with the iron line parameters and N_H frozen, $\chi^2_\nu = 5.27$ for 37 degrees of freedom. This is the second fit shown in Figure 8.3. The residuals have a concave shape, suggesting a possible broad absorption feature.

In Figure 8.4 the same spectrum has been fitted with an additional component — a CSRF. For the energy range 2–45 keV, $\chi^2_\nu = 43$ for 70 degrees of freedom. When the channels below 15 keV are ignored χ^2_ν drops to 1.270 for 34 degrees of freedom without any further fitting. When the iron line and interstellar absorption are removed from the model and the spectrum is re-fitted,

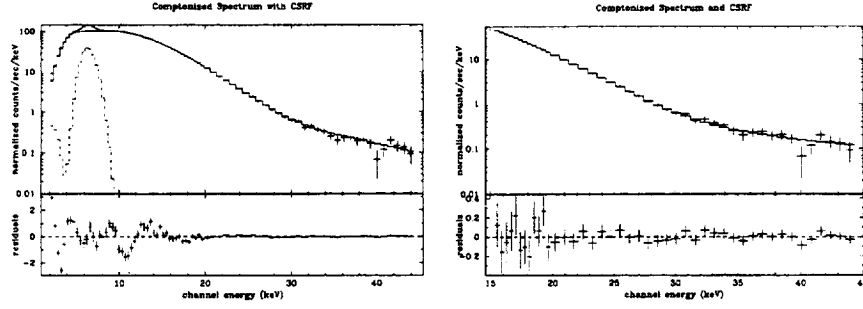


Fig. 8.4— Left: PCA spectrum from orbit #1 showing fitted to a Comptonization model and CSRF and systematic features below 15 keV. Right: the same spectrum re-fitted above 15 keV.

$\chi^2_\nu = 0.7095$ for 38 degrees of freedom.

The improvement in the fit is strong evidence for a cyclotron feature. Similar behavior is found for other continuum models, not just the comptonization model. Models including cyclotron absorption give good fits in the 2–45 keV energy band. The HEXTE data also require the feature. Figure 8.5 shows the results of simultaneous fits to the PCA and HEXTE data from orbit #1 at orbital phase 0.51–0.64. The 90% confidence cyclotron line parameters are $E_{Cy} = 25.1 \pm 0.3$ keV, $\tau = 1.2 \pm 0.2$, and $W = 13.8 \pm 1.6$ keV.

A harmonic of the cyclotron feature with energy constrained to be twice that of the fundamental was added to the model. This caused χ^2_ν to change from 3.084 with 82 degrees of freedom to 3.006 for 80 degrees of freedom which means that the first harmonic is significant at the 86% or 1.5σ level. The possible first harmonic has a depth $\tau = 1.5^{+6.5}_{-0.5}$ and a width $W < 3.2$ keV. Because of the low statistical significance of the feature and the fact that its width is suspiciously small compared to the energy resolution of the detectors, there is no convincing evidence for a first harmonic of the CSRF in the present data.

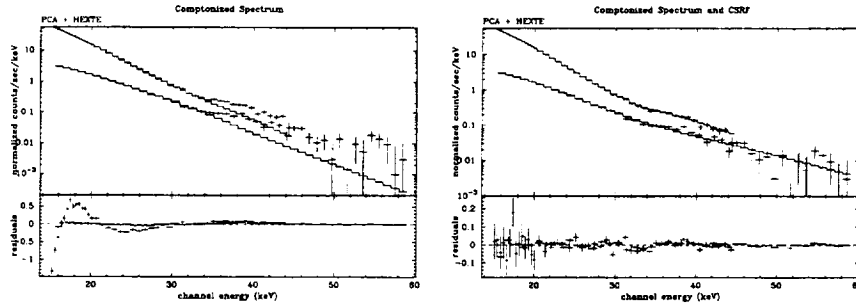


Fig. 8.5— PCA and HEXTE data fitted simultaneously. Left: Comptonized spectrum. Right: Comptonized spectrum and CSRF.

8.4 Discussion and Conclusions

If the apparent absorption feature at 25.1 ± 0.3 keV is in fact due to cyclotron opacity this would imply that the magnetic field is $(2.16 \pm 0.03) \times 10^{12}$ G. The properties of the accreting X-ray pulsars with known cyclotron features are summarized in Table 8.1. In Chapter 5 I used the beat frequency mass accretion model of the 40 mHz quasi-periodic oscillations to predict a surface magnetic field of about 2.6×10^{12} G. Given the uncertainty in the neutron star's mass ($M_x = 1.09^{+0.57}_{-0.52} M_\odot$ at 95% confidence: van Kerkwijk et al. 1995) these values are consistent. If the scattering region extends far above the neutron star surface the field derived from a CSRF would be lower than the surface magnetic field. In Figure 8.6 I have calculated the factor by which the observed CSRF energy differs from the value $E_{Cy} = 11.6 B_{12}$. Close to the surface of the neutron star where $r \gtrsim R_x$, the observed value of E_{Cy} is smaller because of the gravitational redshift. As r becomes larger the magnetic field in the scattering region falls off as $1/r^3$, assuming a dipole field. It should be noted that the large uncertainty in the neutron star's mass allows E_{Cy} and B_{12} to be consistent in any case. The

width of the resonance is about 50% of the cyclotron energy. Comparing this with Figure 8.6 we can see that if the width is mostly due to the scattering region being extended it implies a size of a few kilometers, or a significant fraction of the neutron star's radius. The values of R_{BB} derived in Chapter 6 (~ 2 km) are consistent with this.

Reynolds et al. (1993) investigated the high-energy cut-off in the spectrum of EXO2030+375 with the EXOSAT GSPC. They found that E_c decreased from 20 keV to 10 keV as the luminosity decreased by a factor of 100. They also fitted the high energy cut-off with a CSRF and found that the fitted energies were consistent with the empirical relationship of Makishima et al. (1992) ($E_{\text{Cy}} \sim 2E_c$). The energy of the CSRF decreased from 40 keV to 20 keV as the luminosity decreased. As with the EXOSAT GSPC data on Cen X-3, however, this energy is close to or above the upper limit of the instrument's bandpass. This variation in the apparent cyclotron energy would indicate that the height of the accretion column increased as L_x decreased. This might be expected if a shock which is not radiation-dominated forms above the surface of the neutron star. In the case of a radiative shock we would expect the height of the accretion column to increase with L_x .

Table 8.1. Cyclotron features detected in X-ray pulsar spectra.

Name	P_{orb} (days)	P_{spin} (s)	E_c (keV)	E_{Cy} (keV)	$B(1+z)$ (10^{12} G)	Notes
Her X-1	1.7	1.24	17–21	35	3.0	LMXB
X0115+634	24.3	3.6	7–9	12,23	1.0	Be
BQ Cam	34.25	4.38	14–17	28.5	2.5	Be
X2259+587	?	6.9	≤ 4	$\sim 7?$	0.6	LMXB
Cep X-4	?	66.3	15–17	32	2.8	?
Vela X-1	8.96	283	15–20	27	2.3	HMXB
X1907+097	8.38	438	14–16	21	1.8	Be
QV Nor	3.73	530	14–16	21	1.8	HMXB
GX301–2	41.5	690	19–21	40	3.4	HMXB
A 0535+262	111	104		$\sim 50, 110$	~ 5	Be*
4U1626–67	0.029	7.7	$21.3^{+0.4}_{-0.3}$	37 ± 1	3.3	LMXB [†]
Cen X-3	2.09	4.82	10–15	25.1 ± 0.2	2.16 ± 0.02	HMXB [‡]

*Kendziorra et al. (1994); Grove et al. (1995).

[†]Orlandini et al. (1998).

[‡]Present work.

Note. — From White et al. (1995, and references therein) unless otherwise stated.

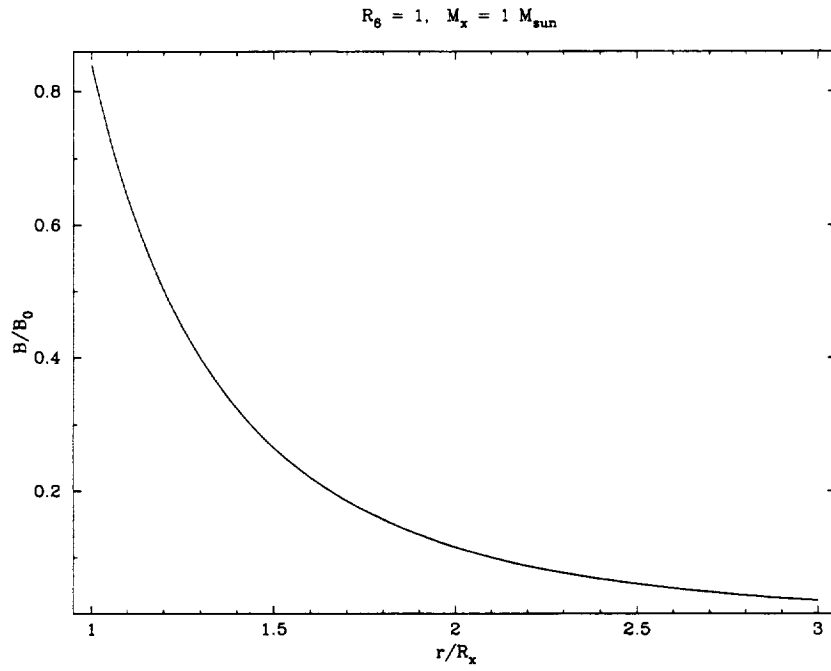


Fig. 8.6— Variation of observed magnetic field with height above the neutron star surface. The effects of the gravitational redshift are included and a dipolar field is assumed.

Chapter 9

Conclusions

9.1 List of Results

Here are the main results of this work:

- The iron line in Cen X-3 is a blend of fluorescent and recombination lines.
- The 6.4 keV fluorescent line pulsates while the 6.7 and 6.9 keV recombination lines do not. This confirms that the 6.4 keV line is produced by fluorescence of dense material close to the neutron star while the 6.7 and 6.9 keV lines are produced by the extended ionized stellar wind of the companion.
- There is some evidence for a reflected continuum in Cen X-3.
- The continuum spectrum is consistent with unsaturated Comptonization of soft photons from the subsonically settling accretion column.
- The pulse profile of Cen X-3 is much more variable than was previously known. This may be due to luminosity-induced changes in the structure of the accretion column.

- The light curve exhibits flares on a timescale of minutes. These may be caused by accretion instabilities. If they are caused by fluctuations in the density of the stellar wind then a portion of this wind must accrete directly onto the neutron star as diffusion in the disk should smear out fluctuations this short.
- A CSRF has been detected in Cen X-3 at an energy of 25.1 ± 0.3 keV which is consistent with the magnetic field predicted from the beat frequency mass accretion model of the QPO.
- The first direct measurement of the magnetic field of Cen X-3 from X-ray spectroscopy has been carried out. The derived value is $(2.16 \pm 0.03) \times 10^{12}$ G.
- The CSRF is broad (13.8 ± 1.6 keV). This is why it has not been convincingly detected before.

9.2 Future Work

There are several X-ray astronomy missions due to begin in the next few years that promise to provide new insights into the nature of HMXBs such as Cen X-3. The information for the following sections was gathered mainly from the mission websites and will probably change. Some of the instruments described below will have large effective areas in Cen X-3's cyclotron region. It would be interesting to measure the short-term variability of the CSRF parameters and see how they relate to the short-term variability of the luminosity. Both of these phenomena originate in the accretion column.

High resolution spectroscopy of the iron line region will be useful in mapping out the stellar wind in Cen X-3. AXAF (see below) is the next mission that will make this possible.

9.2.1 The Advanced X-Ray Astrophysics Facility

The Advanced X-Ray Astrophysics Facility (AXAF), due to be launched in 1998, combines CCD detectors with transmission gratings to provide high spatial and spectral resolution. AXAF will be placed in a high, elliptical earth-orbit to allow uninterrupted observing intervals more than 48 hours long. There are two focal plane instruments.

The High Resolution Camera (HRC) is a microchannel plate. It will be used for high resolution imaging, fast timing measurements, and for observations requiring a combination of both.

The second instrument is the AXAF CCD Imaging Spectrometer (ACIS). A two-dimensional array of these small detectors will do simultaneous imaging and spectroscopy. Images of extended objects can be obtained along with spectral information from each pixel.

There are two transmission grating spectrometers, formed by sets of gold gratings placed just behind the mirrors. One set is optimized for low energies (LETG) and the other for high energies (HETG). Spectral resolving powers in the range 100–2000 can be achieved with good efficiency. These produce spectra dispersed in space at the focal plane. Either the CCD array or the HRC can be used to record data.

9.2.2 X-Ray Multi-Mirror Mission

The X-Ray Multi-Mirror Mission (XMM) will cover the 0.1–10 keV energy range. Its large effective area and highly eccentric orbit will allow long observations of X-ray sources with an unprecedented sensitivity. XMM will carry an optical/UV telescope together with three parallel-mounted X-ray telescopes to allow simultaneous observations in the optical and UV.

9.2.3 Astro-E

Astro-E, the fifth Japanese X-ray satellite which is scheduled for launch in the year 2000, will carry three telescopes.

The X-Ray Spectrometer (XRS) consists of an array of microcalorimeters and foil mirrors developed at GSFC. This will allow 10 eV FWHM spectroscopy of cosmic X-ray sources with high quantum efficiency. The XRS calorimeters are similar to those described in Section 2.3.1. Combined with an effective area of $\sim 400 \text{ cm}^2$ at 6 keV, the high spectral resolution of the XRS should provide new insights into the ionization structure of the stellar winds in HMXB systems.

XIS consists of four CCD X-ray Imaging Spectrometers, also using foil mirrors, which provide images of X-ray sources. The detectors are being built by MIT.

HXD is a Hard X-ray Detector, for observing high-energy (10–700 keV) X-rays.

9.2.4 The Constellation Mission

Constellation will carry the next generation of microcalorimeters. The target energy resolution is 2 eV at 6 keV. Six identical satellites will be launched 3–4 months apart with high earth or libration point orbits for high viewing efficiency. Each spacecraft will carry two coaligned telescope systems covering the 0.25–40 keV band. The high throughput spectroscopy X-ray telescope (SXT) will have an array of high efficiency quantum microcalorimeters plus a reflection grating/CCD system that simultaneously cover the 0.25–10 keV energy band. The gratings deflect part of the beam from the calorimeter to maintain resolving power of 300 at low energies. The Hard X-ray telescope (HXT) system will use grazing incidence focusing optics with a CdZnTe or similar imaging spectrometer with up to four telescopes per spacecraft to provide the required effective area up to 40 keV.

9.2.5 Summary

Figure 9.1 shows the effective areas of these observatories.

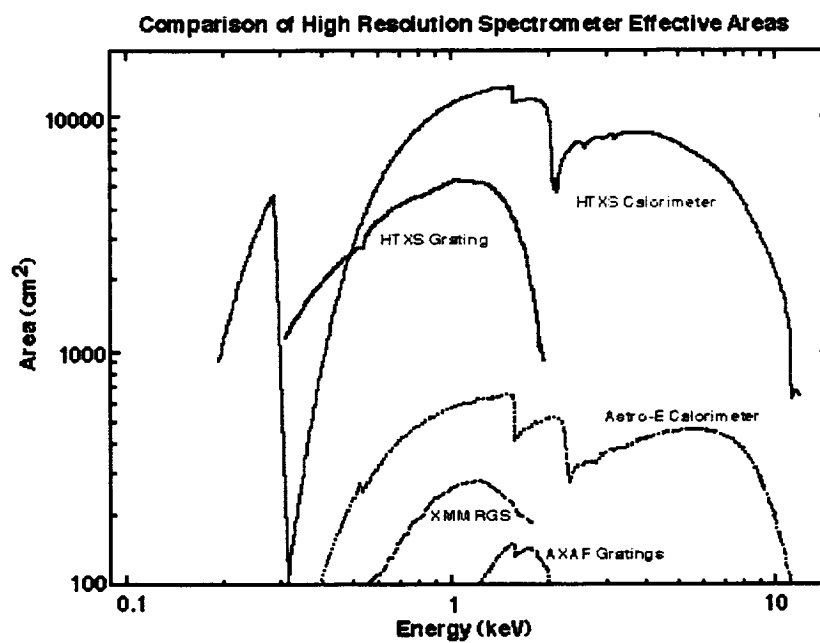


Fig. 9.1— Comparison of effective areas of future X-ray missions.

A.1 Aluminum Proof-of-Concept Kinetic Inductors

A.1.1 Device Fabrication

These devices were fabricated at GSFC by Gayle Rawley. The meander strip and ground plane were patterned using a lift-off process (Hatzakis et al. 1980). A thick layer of photoresist was placed on the wafer and Al was deposited from vapor. The resist was then dissolved and its Al covering lifted off, leaving Al only on those parts of the wafer that had not been covered by resist. With this process there is no need to expose the device to strong etchants which might damage the dielectric layer. The SiO_2 layer was chemically deposited and later etched to expose parts of the ground plane for bonding. The meander strip and ground plane are about 4000 Å thick. These values are much larger than the penetration depth λ and were chosen to ensure reliable patterning and ease of bonding at the expense of sensitivity. The insulating SiO_2 layer is about 1100 Å thick. The meander is 7 cm long and 3.85 μm wide. The layout of the chip is shown in Figure A1.

A.1.2 Testing

The superconducting-normal transition of the meander strip was observed with a current of 10 μA . The critical temperature was found to be 1.224 ± 0.006 K. As expected for a thin film, this is elevated slightly from the value for bulk aluminum which is 1.196 K (Ashcroft and Mermin 1976).

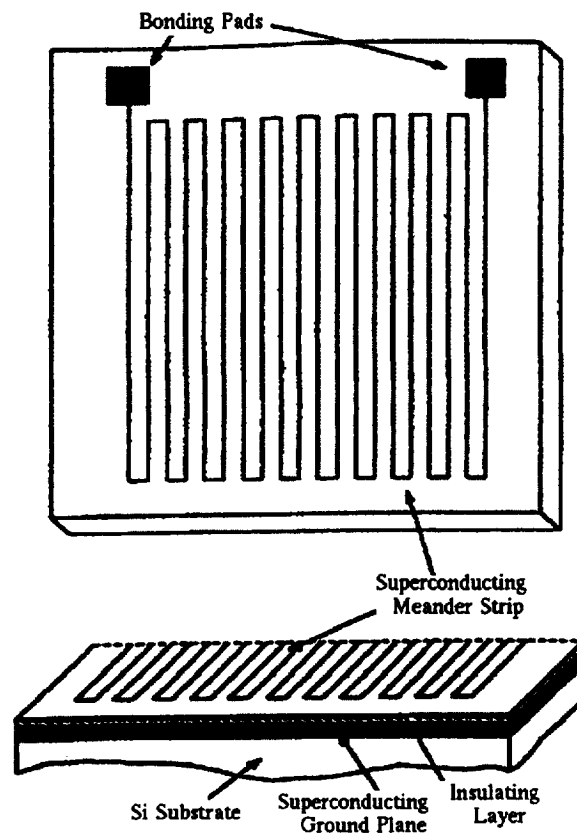


Fig. A1— Layout of the kinetic inductor.

Meservey and Tedrow (1969) have used a tunnel diode oscillator to measure kinetic inductance. This readout method was chosen for the present study because of the oscillator's high stability and its ability to operate at liquid helium temperatures and also because of ease of implementation. It was intended that a phase-locked loop would measure the frequency but it was found that a frequency counter was more convenient due to its greater dynamic range. The kinetic inductor was mounted in a T0-5 can on an aluminum stage along with a germanium resistance thermometer and a heating resistor. The stage was suspended on Kevlar threads from a supporting frame which held the tunnel diode oscillator. A thin copper strip connecting the stage to the frame was used to fine tune the thermal time constant of the stage. The frame was mounted on the cold stage of a ^3He dewar.

For kinetic inductance measurements the device was included in the tank circuit of the tunnel diode oscillator through superconducting niobium wires and the frequency was measured for different temperatures. The niobium wires were strung under tension to reduce microphonics. The setup is shown in Figure A3. It might seem simpler to have the kinetic inductor in series with L rather than C . However the present arrangement was chosen because the tunnel diode requires a dc bias current of about $30\ \mu\text{A}$ which is greater than the critical current of some of the devices we have been testing. Figure A2 shows an I - V curve for the General Electric BD5 tunnel diode that was used in the oscillator. The data were obtained at a temperature of 77 K. For oscillations, the tunnel diode was biased at 120 mV, giving a negative resistance $R_d = -4.2\ \text{k}\Omega$.

Figure A4 shows how the oscillator frequency depends on temperature. As expected, the frequency drops sharply as T approaches T_c . The data were fitted

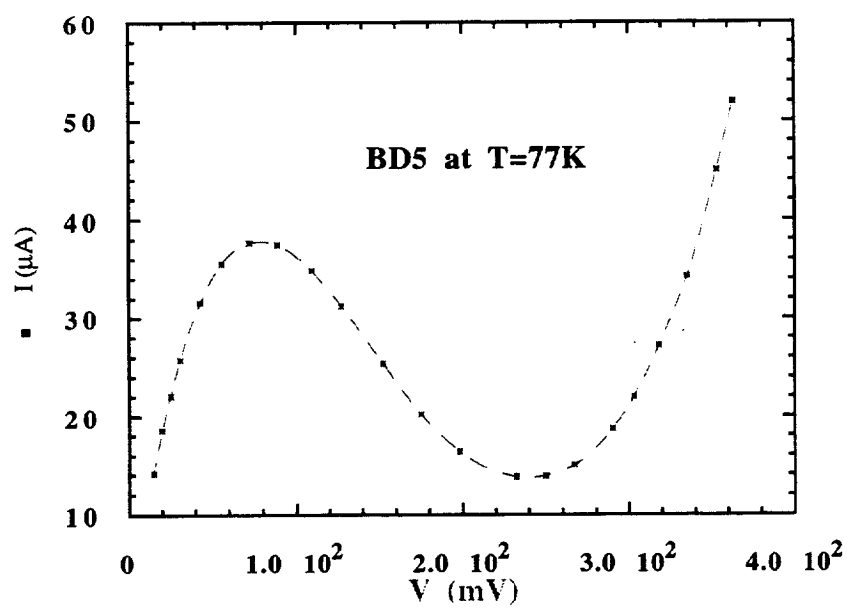


Fig. A2— I - V curve at a temperature of 77 K for the General Electric BD5 tunnel diode used in the readout oscillator.

to a function of the form

$$f = f_0 \left(1 - f_0^2 \frac{\alpha}{\sqrt{1 - (\frac{T}{T_c})^4}} \coth \beta \sqrt{1 - (\frac{T}{T_c})^4} \right) \quad (\text{A1})$$

where

$$\alpha = \frac{4\pi^2 C^2}{(C + C_1)} \frac{\mu_0 l}{w} \lambda(0) \quad (\text{A2})$$

and

$$\beta = \frac{d}{\lambda(0)} \quad (\text{A3})$$

The frequency for $L_k = 0$ is f_0 . Here the ground plane and meander strip are assumed to have equal T_c and $\lambda(0)$. This is reasonable since they were deposited by the same process and their thicknesses are approximately equal. From the device parameters one expects $\alpha = 1.3 \times 10^{-6} \text{ MHz}^{-2}$ and $\beta = 8.3$ for $\lambda(0) = 480 \text{ \AA}$. The best fit values are $\alpha = (8.2 \pm 0.3) \times 10^{-7} \text{ MHz}^{-2}$ and $\beta = 5.1 \pm 0.9$. The apparent disagreement between the expected and measured values may be due to the fact that the large uncertainties in the temperature have not been taken into account.

Because the Al films are so thick, the kinetic inductance is found to be approximately proportional to the penetration depth.

A.2 Limitations of Kinetic Inductors

A.2.1 Critical currents

The next step in the evaluation of kinetic inductance detectors was to try out new materials in the approach to lower temperatures. Test meander strips were provided by David Osterman of HYPRES, Inc..

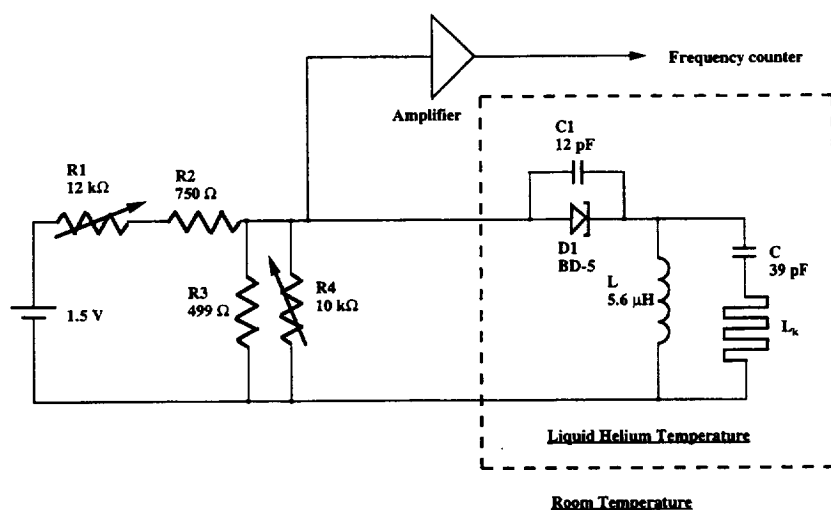


Fig. A3— The tunnel diode oscillator readout.

The first set of strips to be tested were made of molybdenum. These meanders were 1200 \AA thick, $5 \text{ }\mu\text{m}$ wide, and 88 cm long. Critical currents around $10 \text{ }\mu\text{A}$ were measured for these strips in a pumped ^3He dewar. Figure A5 shows the measured resistance of a molybdenum meander strip for different bias currents. The transition temperature T_c depends on the current and the transition is hysteretic.

The next step in the approach to lower operating temperatures was titanium. These strips were 1000 \AA thick, $5 \text{ }\mu\text{m}$ wide, and 88 cm long. The superconducting transitions of these strips were measured in a $^3\text{He}/^4\text{He}$ dilution refrigerator. These transitions are shown in Figures A6 and A7. The critical currents are much lower for the titanium strips than for the molybdenum strips. It was thought that this might have been caused by oxidation of the strips. Thus HYPRES produced a batch of titanium strips with a thin layer of gold for passivation.

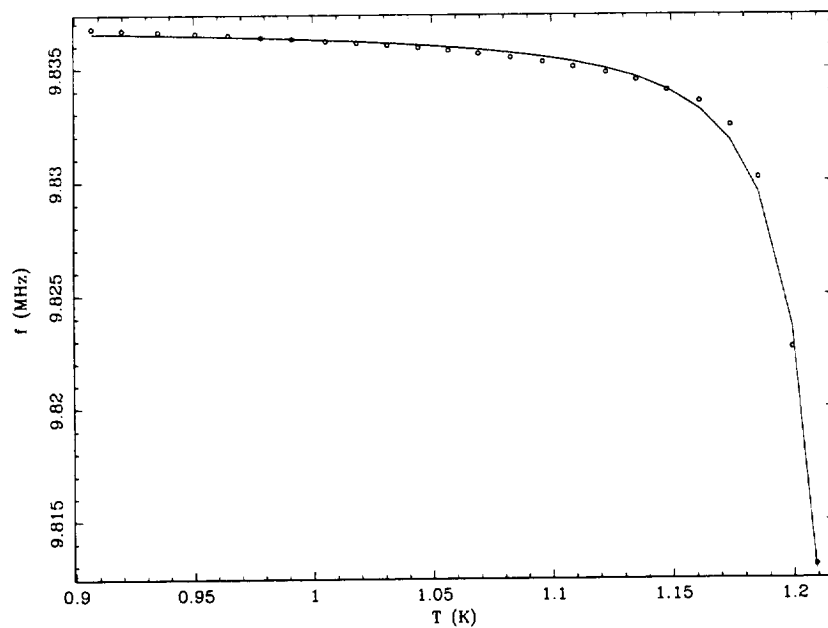


Fig. A4— Variation of TDO frequency with temperature.

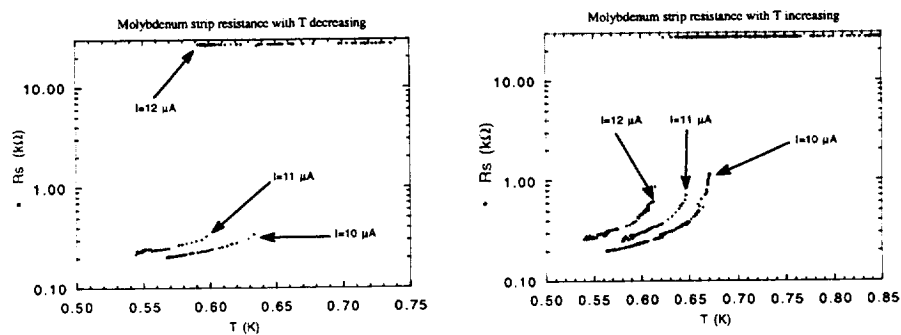


Fig. A5— Superconducting transitions of molybdenum meander strip: a) with temperature decreasing and b) with temperature increasing.

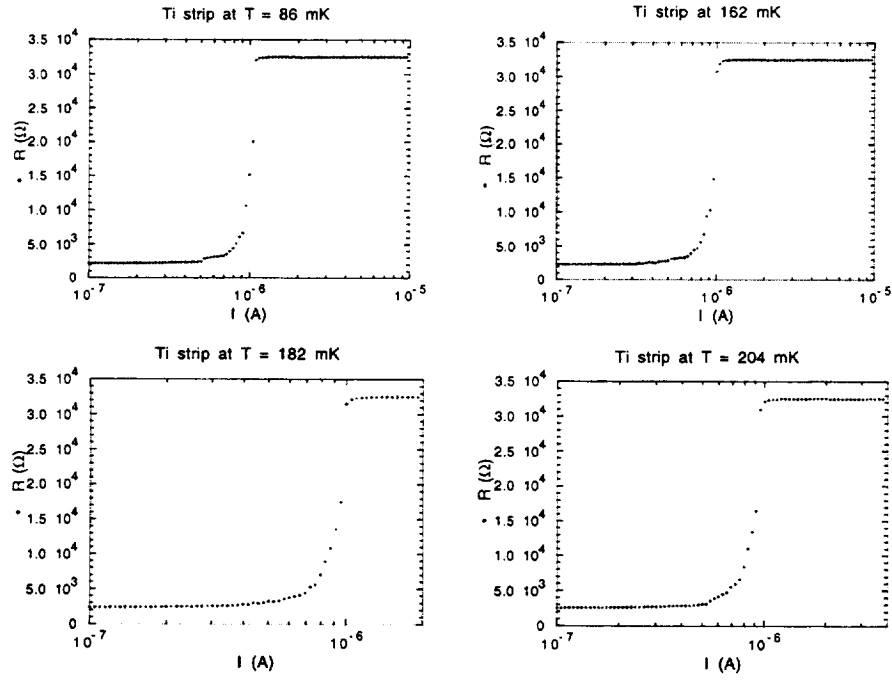


Fig. A6— Superconducting transitions of titanium meander strip at different temperatures.

These strips performed worse than the pure titanium strips. Their transitions were broader and showed steps. The broadening of the transitions may be due to the proximity effect. This results from the overlapping of the Cooper pair wavefunctions into the normal metal (in this case gold). This is possible because of the long coherence length ($\sim 1 \mu\text{m}$) of the superconductor. The result is that the titanium-gold bilayer will be a superconductor, but not as “good” a superconductor as the pure titanium film.

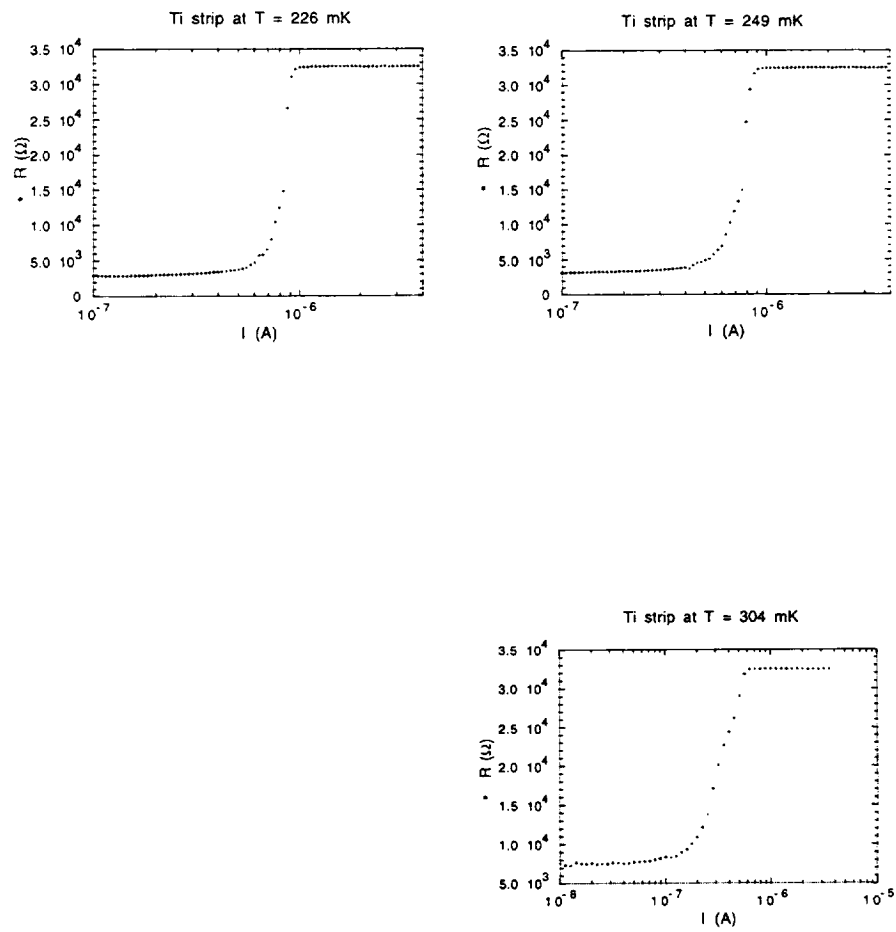


Fig. A7— Superconducting transitions of titanium meander strip at different temperatures.

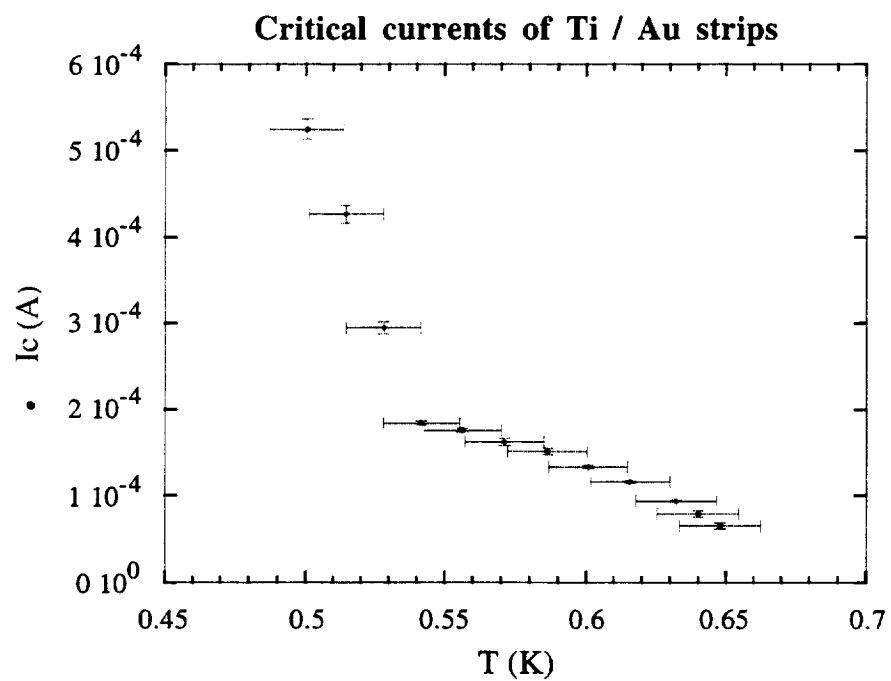


Fig. A8— Critical currents of gold-passivated titanium meander strips.

A.3 Conclusions

Critical currents are important for kinetic inductance detectors because the size of the detection signal is proportional to the current through the meander strip. Currents on the order of 1 mA are required to achieve the target resolution of 2 eV. The currents we have been obtaining are at least two orders of magnitude lower than this. Due to the problems with low critical currents the future of kinetic inductance detectors in X-ray astronomy is doubtful. Transition edge sensors do not have this limitation to the same degree. The parameter that determines their resolution is the transition width. Films with narrow enough transitions have already been produced. Thus transition edge sensors hold more promise as a detector technology.

Glossary

A0	The central pixel of the A-telescope carried by BBXRT.
Accretion column	The magnetically-channeled flow of matter to a neutron star's magnetic pole. The accretion column can be either a thin slab or a tall column depending on whether the infalling matter is decelerated close to the neutron star's surface or in a shock high above the surface, respectively.
ADC	Accretion disk corona.
Alfvén radius	The radius at which the pressure due to the pulsar's magnetic field equals the ram pressure of infalling material.
Alfvén Shell	The Alfvén shell is the hollow shell formed by accreting material as it follows magnetic field lines at the surface of the magnetosphere (see Figure 1.14).
ASCA	The Advanced Satellite for Cosmology and Astrophysics. This is the fourth Japanese X-ray satellite, launched on February 20, 1993.
ASM	All Sky Monitor — a telescope carried by RXTE which provides continuous monitoring of the visible sky in the 2–10 keV band.
Astro-E	The fifth Japanese X-ray satellite. Due to be launched in the year 2000.
AXAF	The Advanced X-Ray Astrophysics Facility due to be launched in 1998.
AXP	Accreting X-ray pulsar.
B0	The central pixel of the B-telescope carried by BBXRT.
Barycentric time	Time referred to the solar system's barycenter or center of mass.

BATSE	The Burst and Transient Explorer. An all-sky monitoring gamma ray telescope carried by CGRO. It can be used to make observations of pulsed sources using earth occultations.
BBXRT	The Broad-band X-Ray Telescope (see Section 3.1).
CCD	Charge-coupled device.
CGRO	The Compton Gamma Ray Observatory, launched in 1991.
CSRF	Cyclotron Scattering Resonance Feature (see Section 1.4.2).
EXOSAT	The European X-Ray Observatory Satellite (see Section 3.2). It operated from May 26, 1983 to April 9, 1986.
Fan beam	A broad radiation emission pattern expected from an accretion column whose height is large compared to its width (see Figure 1.8). In this case the observed intensity will be greatest when the line of sight is perpendicular to the pulsar's magnetic field.
Ginga	The third Japanese X-ray satellite. It was launched on 5 February 1987 and re-entered the earth's atmosphere on 1 November 1991.
GSFC	Goddard Space Flight Center.
GSPC	Gas Scintillation Proportional Counter (see Section 3.2.1).
HEXE	High Energy X-ray Experiment — a phoswich detector in the Kvant 1 module of the Mir space station. It covers the energy band 15–200 keV.
HMXB	High-mass X-ray binary.
HXD	The Hard X-ray Detector to be carried by Astro-E.
JFET	Junction field effect transistor.
LAC	Large Area Collector — a proportional counter X-ray telescope carried by <i>Ginga</i> . The LAC covered the energy range ~ 1 –37 keV.
Light-cylinder radius	The radius at which a test particle would have to move at the speed of light in order to co-rotate with the pulsar.

Line-driven wind	A stellar wind which is driven by the absorption of UV photons with bound-state atomic transitions.
LMXB	Low-mass X-ray binary.
Magnetosphere	The region surrounding the neutron star where the motion of the accreting matter is dominated by the neutron star's magnetic field. The magnetosphere's radius is approximately the Alfvén radius.
ME	The Medium Energy telescope carried by EXOSAT.
MOS capacitor	Metal-oxide-semiconductor capacitor — a capacitor where one electrode (the gate) is metal, the other (the substrate) is a semiconductor, and the dielectric is formed from an oxide layer and a depletion region. The depth of the depletion layer, and hence the capacitance, depend on the gate voltage.
OSO 8	The Orbiting Solar Observatory-I. It was launched on 21 June 1975 and operated until late September 1978. It carried GSFC's Cosmic X-ray Spectrometer which was used to observe X-ray sources in the 2–60 keV band.
OSSE	The Oriented Scintillation Spectrometer Experiment — a gamma ray scintillation telescope carried by CGRO. It covers the energy range 50 keV–10 MeV.
PCA	Proportional Counter Array — an X-ray telescope carried by RXTE.
Pencil beam	A narrow radiation emission pattern expected from an accretion column whose height is small compared to its area. In this case the observed intensity will be greatest when the line of sight is along the pulsar's magnetic field.
phoswich	Short for phosphor sandwich — a scintillation detector with a guard scintillator for rejecting charged-particle events.
Population I	Population I stars have high abundances ($> 1\%$) of elements heavier than helium. They are believed to have formed after the interstellar medium was enriched by heavy elements from supernovae. They are thus younger than population II stars and can have large masses.

Population II	Population II stars are stars with low abundances of elements heavier than helium. They are believed to have formed before the interstellar medium was enriched by heavy elements from supernovae. They are thus the oldest stars in the Galaxy. Because heavier stars have shorter lives, population II stars have low masses.
Propeller effect	The propeller effect refers to the centrifugal barrier encountered by accreting matter which is orbiting more slowly than the magnetosphere. This centrifugal barrier can cause the accreting matter to be ejected.
QPO	Quasi-periodic oscillation.
ROSAT	<i>Röntgen Satellite</i> — a German-U.S.-U.K. X-ray satellite launched on June 1 1990.
RXTE	The Rossi X-Ray Timing Explorer.
SAA	The South Atlantic Anomaly — a region of low geomagnetic rigidity off the east coast of Brazil which has a high charged-particle flux.
Si(Li) detector	An X-ray detector consisting of a reverse-biased silicon diode in which a depletion layer has been created by drifting in lithium.
SQUID	Superconducting quantum interference device — a sensitive magnetometer.
TTM/COMIS	COded Mask Imaging Spectrometer — a wide-angle coded-aperture camera in the Kvant 1 module of the Mir space station. It covers the 20–30 keV energy band with a spatial resolution of 2'.
UV	Ultraviolet.
Wolter geometry	A scheme for focussing X-rays with grazing-incidence mirrors. Paraxial X-rays are reflected first by a paraboloidal surface and then by a hyperboloid to form an image.
XIS	X-ray Imaging Spectrometers. These are telescopes with conical foil mirrors and CCD detectors that will be carried by Astro-E.
XMM	The X-Ray Multi-Mirror Mission.

XQC	The X-Ray Quantum Calorimeter — a sounding rocket payload comprising an array of X-ray microcalorimeters. It was successfully flown in June 1996.
XRS	The X-Ray Spectrometer. An array of microcalorimeters to be carried by Astro-E.

References

- Alexander, S. G. and Mészáros, P. 1991, *Astrophys. J.*, **372**, 565
- Allen, G. E., Keohane, J. W., Gotthelf, E. V., Petre, R., Jahoda, K., Rothschild, R. E., Lingenfelter, R. E., Heindl, W. A., Marsden, D., Gruber, D. E., Pelling, M. R., and Blanco, P. R. 1997, *Astrophys. J.*, **487**, L97
- Alpar, M. A. and Shaham, J. 1985, *Nature*, **316**, 239
- Anzer, U. and Börner, G. 1995, *Astron. Astrophys.*, **299**, 62
- Arnaud, M. and Raymond, J. 1992, *Astrophys. J.*, **398**, 394
- Ashcroft, N. W. and Mermin, N. D. 1976, *Solid State Physics*, Philadelphia: Saunders College
- Audley, M. D. et al. 1996, *Astrophys. J.*, **457**, 397
- Audley, M. D., Kelley, R. L., and Rawley, G. L. 1993, *J. Low. Temp. Phys.*, **93**, 245
- Avni, Y. and Bahcall, J. N. 1975, *Astrophys. J.*, **197**, 675
- Bevington, P. R. 1969, *Data Reduction and Error Analysis for the Physical Sciences*, New York: McGraw-Hill
- Bhattacharya, D. and Srinivasan, G. 1995, in W. H. G. Lewin, J. van Paradijs, and E. P. J. van den Heuvel (eds.), *X-ray binaries*, pp 495–522, Cambridge: Cambridge University Press
- Bildsten, L. 1995, *Astrophys. J.*, **438**, 852
- Bildsten, L. 1997, in A. Alpar, L. Bucccheri, and J. van Paradijs (eds.), *The Many Faces of Neutron Stars*, Dordrecht: Kluwer
- Bildsten, L. and Brown, E. F. 1997, *Astrophys. J.*, **477**, 897

- Bildsten, L., Chakrabarty, D., Chiu, J., Finger, M. H., Koh, D. T., Nelson, R. W., Prince, T. A., Rubin, B. C., Scott, D. M., Stollberg, M., Vaughan, B. A., Wilson, C. A., and Wilson, R. B. 1997, *Astrophys. J. Suppl. Ser.*, **113**, 367
- Blondin, J. M. 1994a, *Astrophys. J.*, **435**, 756
- Blondin, J. M. 1994b, in S. S. Holt and C. S. Day (eds.), *The Evolution of X-Ray Binaries*, p. 578, New York: AIP Press
- Blondin, J. M., Stevens, I. R., and Kallman, T. 1991, *Astrophys. J.*, **371**, 684
- Boldt, E. 1974, in F. B. McDonald and C. E. Fichtel (eds.), *High Energy Particles and Quanta in Astrophysics*, pp 368–382, Cambridge: MIT Press
- Bonnet-Bidaud, J. M. and van der Klis, M. 1979, *Astron. Astrophys.*, **73**, 90
- Bradt, H. V. D. and McClintock, J. E. 1983, *Annu. Rev. Astron. Astrophys.*, **21**, 13
- Bulik, T., Mészáros, P., Woo, J. W., Nagase, F., and Makishima, K. 1992, *Astrophys. J.*, **395**, 564
- Charles, P. A. and Seward, F. D. 1995, *Exploring the X-Ray Universe*, Cambridge: Cambridge University Press
- Chodil, G., Mark, H., Rodrigues, R., Seward, F., Swift, C. D., Hiltner, W. A., Wallerstein, G., and Mannery, E. 1967, *Phys. Rev. Lett.*, **19**, 681
- Clark, G. W., Minato, J. R., and Mi, G. 1988, *Astrophys. J.*, **324**, 974
- Conti, P. S. 1978, *Astron. Astrophys.*, **63**, 225
- Cowan, R. D. 1981, *The Theory of Atomic Structure and Spectra*, Berkeley: University of California Press
- Cui, W., Almy, R., Deiker, S., McCammon, D., Morgenthaler, J., Sanders, W. T., Kelley, R. L., Marshall, F. J., Moseley, S. H., Stahle, C. K., and Szymkowiak, A. E. 1994, *Proc. SPIE*, **2280**, 362
- Davidson, K. and Ostriker, J. P. 1973, *Astrophys. J.*, **179**, 585
- Day, C. S. R., Nagase, F., Asai, K., and Takeshima, T. 1993, *Astrophys. J.*, **408**, 656
- Day, C. S. R. and Stevens, I. R. 1993, *Astrophys. J.*, **403**, 322

- Day, C. S. R. and Tennant, A. F. 1991, *Mon. Not. R. Astron. Soc.*, **251**, 76
- Deeter, J. E., Boynton, P. E., and Pravdo, S. H. 1981, *Astrophys. J.*, **247**, 1003
- Ebisawa, K., Day, C. S. R., Kallman, T. R., Nagase, F., Kotani, T., Kawashima, K., Kitamoto, S., and Woo, J. 1996, *Publ. Astron. Soc. Japan*, **48**, 425
- Eggelton, P. P. 1983, *Astrophys. J.*, **268**, 368
- Elsner, R. F. and Lamb, F. K. 1977, *Astrophys. J.*, **215**, 897
- Finger, M. H., Wilson, R. B., and Fishman, G. J. 1994, in C. E. Fichtel, N. Gehrels, and J. P. Norris (eds.), *The Second Compton Symposium*, p. 304, New York: AIP Press
- Frank, J., King, A. R., and Raine, D. J. 1985, *Accretion Power in Astrophysics*, Cambridge: Cambridge University Press
- Gehrels, N. and Tueller, J. 1993, *Astrophys. J.*, **407**, 597
- Gendreau, K. 1995, *Ph.D. dissertation*, Massachusetts Institute of Technology
- George, I. M. and Fabian, A. C. 1991, *Mon. Not. R. Astron. Soc.*, **249**, 352
- Ghosh, P. and Lamb, F. K. 1979a, *Astrophys. J.*, **232**, 259
- Ghosh, P. and Lamb, F. K. 1979b, *Astrophys. J.*, **234**, 296
- Ghosh, P., Lamb, F. K., and Pethick, C. J. 1977, *Astrophys. J.*, **217**, 578
- Giacconi, R. 1974, in R. Giacconi and H. Gursky (eds.), *X-Ray Astronomy*, pp 1–23, Dordrecht: D. Reidel
- Giacconi, R., Gursky, H., Kellogg, E., Schreier, E., and Tananbaum, H. 1971, *Astrophys. J.*, **167**, L67
- Giacconi, R., Gursky, H., Paolini, F. R., and Rossi, B. B. 1962, *Phys. Rev. Lett.*, **9**, 439
- Grove, J. E., Strickman, M. S., Johnson, W. N., Kurfess, J. D., Kinzer, R. L., Starr, C. H., Jung, G. V., Kendziorra, E., Kretschmar, P., Maisack, M., and Staubert, R. 1995, *Astrophys. J.*, **438**, L25
- Hatchett, S. and McCray, R. 1977, *Astrophys. J.*, **211**, 552
- Hatzakis, M., Canavello, B. J., and Shaw, J. M. 1980, *IBM. J. Res. Develop.*, **24**, 452

- Hayakawa, S. 1985, *Phys. Rep.*, **121**, 319
- Hjellming, R. M. 1978, in *Physics and Astrophysics of Neutron Stars and Black Holes*, pp 185–201, Amsterdam: North Holland Publishing Co.
- Hjellming, R. M. and Han, X. 1995, in W. H. G. Lewin, J. van Paradijs, and E. P. J. van den Heuvel (eds.), *X-Ray Binaries*, pp 308–330, Cambridge: Cambridge University Press
- Illarionov, A. F. and Sunyaev, R. A. 1975, *Astron. Astrophys.*, **39**, 185
- Inoue, H. 1985, *Space Sci. Rev.*, **40**, 317
- Irwin, K. D. 1995, *Appl. Phys. Lett.*, **66**, 1998
- Irwin, K. D., Hilton, G. C., Wollman, D. A., and Martinis, J. M. 1996, *Appl. Phys. Lett.*, **69**, 1945
- Joss, P. C. 1978, *Astrophys. J.*, **225**, L123
- Joss, P. C. and Li, F. K. 1980, *Astrophys. J.*, **238**, 287
- Joss, P. C. and Rappaport, S. A. 1984, *Annu. Rev. Astron. Astrophys.*, **22**, 537
- Kallman, T. 1993, in W. Ronan (ed.), *APS Topical Conference on Atomic Processes in Plasmas*, San Antonio, TX
- Kallman, T. R. 1991, in A. Treves, G. C. Perola, and L. Stella (eds.), *Iron Line Diagnostics in X-Ray Sources*, pp 87–97, Berlin: Springer-Verlag
- Kallman, T. R. and McCray, R. 1982, *Astrophys. J. Suppl. Ser.*, **50**, 263
- Kelley, R. L., Rappaport, S., Clark, G. W., and Petro, L. D. 1983, *Astrophys. J.*, **268**, 790
- Kellogg, E. M. 1975, *Astrophys. J.*, **197**, 609
- Kendziorra, E., Kretschmar, P., Pan, H. C., Kunz, M., Maisack, M., Staubert, R., Pietsch, W., Trümper, J., Efremov, V., and Sunyaev, R. 1994, *Astron. Astrophys.*, **291**, L31
- Khruzina, T. S. and Cherepaschchuk, A. M. 1986, *Soviet Ast.*, **30**, 295
- Klein, R. I., Arons, J., Jernigan, G., and Hsu, J. J.-L. 1996, *Astrophys. J.*, **457**, L85
- Kompaneets, A. S. 1957, *Soviet Phys. JETP*, **4**, 730

- Kortright, J. B. 1986, in D. Vaughan (ed.), *X-ray Data Booklet*, Berkeley: Lawrence Berkeley Laboratory
- Koyama, K., Makishima, K., and Tanaka, Y. 1986, *Publ. Astron. Soc. Japan*, **38**, 121
- Krolik, J. H. and Kallman, T. R. 1987, *Astrophys. J.*, **320**, L5
- Krzemiński, W. 1974, *Astrophys. J.*, **192**, L135
- Lamb, F. K., Pethick, C. J., and Pines, D. 1973, *Astrophys. J.*, **184**, 271
- Lang, K. R. 1991, *Astrophysical Data: Planets and Stars*, Berlin: Springer-Verlag
- Léna, P. 1988, *Observational Astrophysics*, Berlin: Springer-Verlag
- Lewin, W. H. G., van Paradijs, J., and Taam, R. E. 1995, in W. H. G. Lewin, J. van Paradijs, and E. P. J. van den Heuvel (eds.), *X-Ray Binaries*, pp 175-232, Cambridge: Cambridge University Press
- Little, W. A. 1959, *Can. J. Phys.*, **37**, 334
- Long, K., Agrawal, P. C., and Gramire, G. 1975, *Astrophys. J.*, **197**, L57
- Lotz, W. 1968, *J. Opt. Spect.*, **58**, 915
- Makino, F. and the ASTRO-C Team 1987, *Astrophys. Lett.*, **25**, 223
- Makishima, K. 1986, in K. O. Mason, M. G. Watson, , and N. E. White (eds.), *The Physics of Accretion onto Compact Objects*, p. 249, Berlin: Springer-Verlag
- Makishima, K., Mihara, T., and Murakami, T. 1992, in Y. Tanaka and K. Koyama (eds.), *Frontiers of X-Ray Astronomy*, pp 23-32, Tokyo: Universal Academy Press
- Marshall, F. E., Mushotsky, R. F., Petre, R., and Serlemitsos, P. J. 1993, *Astrophys. J.*, **419**, 301
- Mather, J. C. 1982, *Appl. Opt.*, **21**, 1125
- McCammon, D., Cui, W., Juda, J., Morgenthaler, J., Zhang, J., Kelley, R. L., Holt, S. S., Madjeski, G. M., Moseley, S. H., and Szymkowiak, A. E. 1993, *Nuc. Inst. Meth.*, **A326**, 157
- Meservey, R. and Tedrow, P. M. 1969, *J. Appl. Phys.*, **40**, 2028

- Mészáros, P. 1992, *High-Energy Radiation from Magnetized Neutron Stars*, Chicago: University of Chicago Press
- Mészáros, P. and Nagel, W. 1985a, *Astrophys. J.*, **298**, 147
- Mészáros, P. and Nagel, W. 1985b, *Astrophys. J.*, **299**, 138
- Mészáros, P. and Riffert, H. 1988, *Astrophys. J.*, **327**, 712
- Meyers, N. H. 1961, *Proc. IRE*, **59**, 1640
- Mihara, T. 1995, *Ph.D. dissertation*, University of Tokyo
- Moseley, S. H., Juda, M., Kelley, R. L., McCammon, D., Stahle, C. K., Szymkowiak, A. E., and Zhang, J. 1992, in *Proceedings of an ESA Symposium on Photon Detectors for Space Instrumentation*, pp 13–19
- Moseley, S. H., Mather, J. C., and Mc Cammon, D. 1984, *J. Appl. Phys.*, **56**, 1257
- Nagase, F., Corbet, R. H. D., Day, C. S. R., Inoue, H., Takeshima, T., Yoshida, K., and Mihara, T. 1992, *Astrophys. J.*, **396**, 147
- Ohashi, T., Makishima, K., Ishida, M., Tsuru, T., Tashiro, M., Mihara, T., Kohmura, Y., and Inoue, H. 1991, *Proc. SPIE*, **1549**, 9
- Orlandini, M., Fiume, D. D., Frontera, F., Sordo, S. D., Piraino, S., Santangelo, A., Segreto, A., oosterbroek, T., and Parmar, A. N. 1998, in *to appear in Proceedings of "The Active X-ray Sky: Results from BeppoSAX and Rossi-XTE"*, (astro-ph preprint 9712023)
- Orlando, T. P. and Delin, K. A. 1991, *Foundations of Applied Superconductivity*, Reading: Addison-Wesley
- Owens, A., Denby, M., Wells, A., Keay, A., Graessle, D. E., and Blake, R. L. 1997, *Astrophys. J.*, **476**, 924
- Parmar, A. N., White, N. E., and Stella, L. 1989, *Astrophys. J.*, **338**, 373
- Peacock, A., Andresen, R. D., Manzo, G., Taylor, B. G., Villa, G., Re, S., Ives, J. C., and Kellock, S. 1981, *Space Sci. Rev.*, **30**, 525
- Peterson, K. E. 1982, *Proc. IEEE*, **70**, 420
- Petterson, J. A. 1978, *Astrophys. J.*, **224**, 625
- Pounds, K. A., Cooke, B. A., Ricketts, M. J., Turner, M. J., and Elvis, M. 1975, *Mon. Not. R. Astron. Soc.*, **172**, 473

- Priedhorsky, W. C. and Terrel, J. 1983, *Astrophys. J.*, **273**, 709
- Pringle, J. E. and Rees, M. J. 1972, *Astron. Astrophys.*, **21**, 1
- Reilman, R. F. and Manson, S. T. 1978, *Phys. Rev. A*, **18**, 2124
- Reynolds, A. P., Parmar, A. N., and White, N. E. 1993, *Astrophys. J.*, **414**, 302
- Rothschild, R. E., Blanco, P. R., Gruber, D. E., Heindl, W. A., MacDonald, D. R., Marsden, D. C., Pelling, M. R., Wayne, L. R., and Hink, P. L. 1998, *Astrophys. J.*, **496**, in press
- Rybicki, G. B. and Lightman, A. P. 1979, *Radiative Processes in Astrophysics*, New York: Wiley-Interscience
- Schreier, E., Levinson, R., Gursky, H., Kellogg, E., Tananbaum, H., and Giacconi, R. 1972, *Astrophys. J.*, **172**, L79
- Schreier, E. J., K. Swartz, R., Giacconi, G., Fabbiano, J., and Morin 1976, *Astrophys. J.*, **204**, 539
- Serlemitsos, P., Petre, R., Glasser, C., and Birsá, F. 1984, *IEEE. Trans. Nucl. Sci.*, **NS-31**, 786
- Serlemitsos, P. J., Marshall, F. E., Petre, R., Jahoda, K., Boldt, E. A., Holt, S. S., Mushotsky, R., Swank, J., Szymkowiak, A., Kelley, R., and Loewenstein, M. 1990, in Y. Tanaka and K. Koyama (eds.), *Frontiers of X-Ray Astronomy*, p. 221, Tokyo: Universal Academy Press
- Shakura, N. I. and Sunyaev, R. A. 1973, *Astron. Astrophys.*, **24**, 337
- Shapiro, S. L. and Teukolsky, S. A. 1983, *Black Holes, White Dwarfs, and Neutron Stars*, Wiley-Interscience
- Shibazaki, N. and Lamb, F. K. 1987, *Astrophys. J.*, **318**, 767
- Smale, A. P., Done, C., Mushotzky, R. F., Weaver, K. A., Serlemitsos, P. J., Marshall, F. E., Petre, R., Jahoda, K., Boldt, E. A., Swank, J. H., Szymkowiak, A. E., Kelley, R., and Arnaud, K. 1993, *Astrophys. J.*, **410**, 796
- Smith, R. K. and Dweck, E. 1998, *Astrophys. J.*, *submitted*
- Stahle, C. K., Kelley, R. L., Moseley, S. H., Szymkowiak, A. E., Juda, M., McCammon, D., and Zhang, J. 1993, *J. Low. Temp. Phys.*, **93**, 257
- Sterne, T. E. 1941, *Proc. Nat. Acad. Sci. (U.S.A.)*, **27**, 175

- Sunyaev, R. A. and Titarchuk, L. G. 1980, *Astron. Astrophys.*, **86**, 121
- Takalo, L. O., Tennant, A. F., and Fabian, A. C. 1990, *Adv. Space Res.*, **10**, 105
- Takeshima, T., Dotani, T., Mitsuda, K., and Nagase, F. 1991, *Publ. Astron. Soc. Japan*, **43**, L43
- Tennant, A. F. 1988, in *Talk presented at "Quasi-periodic oscillation in Luminous Galactic X-ray Sources"*, 5th Los Alamos Space Physics / Astrophysics workshop, La Cienega, New Mexico
- Thorne, A. P. 1988, *Spectrophysics*, London: Chapman and Hall
- Tjemkes, S. A., Zuiderwijk, E. J., and van Paradijs, J. 1986, *Astron. Astrophys.*, **154**, 77
- Tuohy, I. R. 1976, *Mon. Not. R. Astron. Soc.*, **174**, 45P
- van den Heuvel, E. P. J. and Heise, J. 1972, *Nature Phys. Sci.*, **239**, 67
- van der Klis, M. 1997, in D. Maoz, A. Sternberg, and E. M. Leibowitz (eds.), *Astronomical Time Series*, p. 121, Dordrecht: Kluwer
- van der Klis, M., Bonnet-Bidaud, J. M., and Robba, N. R. 1980, *Astron. Astrophys.*, **88**, 8
- van Kerkwijk, M. H., van Paradijs, J., and Zuiderwijk, E. J. 1995, *Astron. Astrophys.*, **303**, 497
- van Paradijs, J. and McClintock, J. E. 1995, in W. H. G. Lewin, J. V. Paradijs, and E. P. J. van den Heuvel (eds.), *X-Ray Binaries*, pp 58–125, Cambridge: Cambridge University Press
- VanSpeybroeck, L. P. and Chase, R. C. 1972, *Appl. Opt.*, **11**, 440
- Ventura, J., Nagel, W., and Mészáros, P. 1979, *Astrophys. J.*, **233**, L125
- Voges, W., Pietsch, W., Reppin, C., Trümper, J., Kendiziorra, E., and Staubert, R. 1982, *Astrophys. J.*, **263**, 803
- Wang, T. M. 1987, *Astron. Astrophys.*, **183**, 257
- Wang, Y.-M. and Frank, J. 1981, *Astron. Astrophys.*, **93**, 255
- Weaver, K. et al. 1995, *Astrophys. J. Suppl. Ser.*, **96**, 303
- Weaver, K. A. 1993, *Ph.D. dissertation*, University of Maryland

- Welty, R. P. and Martinis, J. M. 1993, *IEEE. Trans. Appl. Superconductivity*, **3**, 2605
- White, N. E., Nagase, F., and Parmar, A. N. 1995/, in W. H. G. Lewin, J. van Paradijs, and E. J. P. van den Heuvel (eds.), *X-ray Binaries*, p. 1, Cambridge: Cambridge University Press
- White, N. E., Swank, J. H., and Holt, S. S. 1983, *Astrophys. J.*, **270**, 711
- Wood, K. S., Meekins, J. F., Yentis, D. J., Smathers, H. W., McNutt, D. P., Bleach, R. D., Friedman, H., Byram, E. T., Chubb, T. A., and Meidav, M. 1984, *Astrophys. J. Suppl. Ser.*, **56**, 507
- Yaqoob, T. 1997, *Astrophys. J.*, **479**, 184
- Zombeck, Martin, V. 1990, *Handbook of Space Astronomy and Astrophysics*, 2nd ed., Cambridge: Cambridge University Press

CURRICULUM VITAE

Name Michael Damian Audley

Permanent address 10534 Lime Tree Way, Beltsville, MD 20705-2024

Degree and date to be conferred Doctor of Philosophy, 1997

Date of birth June 30, 1966

Place of birth Thurles, Co. Tipperary, Ireland

Secondary education Meánscoil Iosaf, Thurles, Co. Tipperary, Ireland

Education

1997 Ph.D. (Physics), University of Maryland, College Park, MD 20742

1994 M.S. (Physics), University of Maryland, College Park, MD 20742

1989 M.Sc. (Experimental Physics), National University of Ireland (University College, Cork)

Thesis Title: The Photoabsorption Spectra of Strontium and Yttrium in the Extreme Ultraviolet

Supervisor: Prof. M. W. D. Mansfield

1987 B.Sc. (Experimental Physics), National University of Ireland (University College, Cork)

Professional positions held

1991–present Graduate Research Assistant, Department of Astronomy, University of Maryland, College Park, MD 20742

1990 (Summer) Graduate Research Assistant, Department of Astronomy, University of Maryland, College Park, MD 20742

1989–1991 Graduate Teaching Assistant, Department of Physics, University of Maryland, College Park, MD 20742

1984–1989 Teaching Assistant, Department of Experimental Physics, University College, Cork, Ireland

Awards

1990 Ralph D. Meyers Award for Graduate Studies, Department of Physics, University of Maryland

1987–1989 Senior Studentship, University College, Cork

1984–1985 College Scholarship, University College, Cork

1983–1984 Entrance Scholarship, University College, Cork

Honors

1987–1988 Title of College Scholar, University College, Cork

Professional Society Memberships

- American Physical Society
- American Astronomical Society

Publications in Refereed Journals

1. A High Resolution X-Ray Spectrum of Cen X-3, M. D. Audley, R. L. Kelley, E. A. Boldt, K. M. Jahoda, F. E. Marshall, R. Petre, P. J. Serlemitsos, A. P. Smale, J. H. Swank, and K. A. Weaver, 1996, *Astrophys. J.*, **457**, 397
2. 3d Absorption Spectra of Sr I through Sr IV, C. McGuinness, G. O'Sullivan, P. K. Carroll, D. Audley, and M. W. D. Mansfield, 1995, *Phys. Rev. A*, **51**, 2053
3. An X-ray Microcalorimeter with Kinetic Inductance Thermometer and dc SQUID Read-out, D. P. Osterman, R. Patt, R. Kelley, and D. Audley, 1993, *J. Low. Temp. Phys.*, **93**, 251
4. A Prototype Kinetic Inductance Thermometer for X-Ray Calorimetry, M. D. Audley, R. L. Kelley, and G. L. Rawley, 1993, *J. Low. Temp. Phys.*, **93**, 245

Other significant publications

1. The BBXRT Observation of Centaurus X-3, M. D. Audley and R. L. Kelley, 1993, *Bull. Amer. Astron. Soc.*, **25**, 918
2. The BBXRT Observation of Cen X-3, R. L. Kelley and M. D. Audley, 1994, in *New Horizon of X-Ray Astronomy — First Results from ASCA*, ed. F. Makino and T. Ohashi, (Tokyo: Universal Academy), 417
3. Pulse Phase Resolved Spectroscopy of Cen X-3, M. D. Audley, K. Ebisawa, and R. L. Kelley, 1996, *Bull. Amer. Astron. Soc.*, **28**, 1327
4. Broad-Band X-ray Spectroscopy of Cen X-3, M. D. Audley, K. Ebisawa, and R. L. Kelley, 1997, *Bull. Amer. Astron. Soc.*, **29**, 841